Fall 12-14-2018

Detection and Melting of Surface-Bound DNA using a Purely Electrochemical Approach

Denny Ho
denny.ho1992@gmail.com

Detection and Melting of Surface-Bound DNA using a Purely Electrochemical Approach

A thesis presented to the faculty

of the Department of Chemistry

at the University of San Francisco

in partial fulfillment of the requirements for the degree of

Master of Science in Chemistry

Written by

Denny Ho

Bachelor of Science in Chemistry

University of California – Riverside, Riverside, CA

December 5, 2018

Detection and Melting of Surface-Bound DNA using a Purely Electrochemical Approach

Thesis written by Denny Ho

This thesis is written under the guidance of the Faculty Advisory Committee, and approved by all its members, has been accepted in partial fulfillment of the requirements for the degree of

Master of Science
in Chemistry at
the
University of San Francisco

Thesis Committee

Ryan M. West, Ph.D. Date
Research Advisor

Janet Yang, Ph.D. Date
Assistant Professor

Lawrence D. Margerum, Ph.D. Date
Professor

Marcelo Camperi, Ph.D. Date
Dean, College of Arts and Sciences

Acknowledgement

First, I want to thank my research advisor Dr. West for all his advice, trust, expertise, and guidance during my time at the University of San Francisco. I am truly honored to be part of the development of the "Plaid Lab." I am glad that you were the first friendly face I saw in San Francisco. I also want to thank Dr. Yang and Dr. Margerum for being a part of my thesis committee. Special thanks to Andy Huang, Jeff Oda, John Hendricks, Deidre Shymanski, and Angela Qin for helping me with the instruments, logistics, and chemicals that I needed to do my research at USF. Further thanks to all the other professors and graduate students at USF for the advice, emotional support, food/bar outings, and making me laugh. Finally, thanks to everyone I have met at USF, especially the Plaid Lab members: Ryan, Camille, Ngoc, Olaide, Wes, Anthony, Ramsess, Lucas and Arya. Thank you all for the laughs, coffee, and love you have all given me to achieve my goals at USF and beyond.

TABLE OF CONTENTS

Table of Figures

List of Equations

List of Tables

List of Reactions

Abstract

In this thesis, we demonstrate an electrochemical approach for monitoring the electric-field induced melting of surface-bound double-stranded DNA. The electrochemical routine involves repeated chronoamperometry pulses to melt the duplex and square wave voltammetry to monitor the extent of melting. We utilize a scanning potential and constant potential technique to generate melting curves and access the stability and kinetics of the DNA duplexes. Our method uses a mixed monolayer of thiol-modified DNA oligomers and mercaptohexanol on gold electrodes, are subsequently incubated with target DNA covalently modified with electroactive methylene blue. Under room temperature, 10 mM Tris, and optimized electrochemical parameters, DNA duplexes are discriminated based on factors such as base pairs, hairpins, and mismatches. As a proof of concept, this method was extended towards a label-free DNA melting method.

Chapter 1: General Electrochemical Concepts

Electrochemistry is the study of chemical changes caused by the passage of an electric current and the production of electrical energy by chemical reaction.[1] This passage of current, or electron transfer, is typically depicted as the following;

$$O_{(aq)} + ne^- \underset{k_a}{\overset{k_c}{\rightleftharpoons}} R_{(aq)} \quad \text{(Rxn.1)}$$

where O represents the oxidized species, n is the number of electrons transferred and R represents the reduced species. The rates of the cathodic (forward) and anodic (reverse) reactions are k_c and k_a, respectively. Electron transfer reactions are critical in the natural and technological world. For example, biochemical cycles, such as the Krebs cycle, involves electron transfer to produce 34 ATP from carbon dioxide and water.[2] Furthermore, electron transfer allows the chemicals in batteries (or any voltaic cell) to produce electrical energy.[3] In this thesis, we utilize the oxidation and reduction of an electroactive species, methylene blue, to monitor the denaturation of electrode-bound DNA duplexes.

1.1. Electrode Kinetics

The rate of an electrochemical reaction not only depends on the concentrations of O and R, but also the electrode potential. In Rxn.1 above the rate constants k_c and k_a are proportional to the concentrations of their respective species and change exponentially with applied potential:

$$k_c = k_c^o\left(e^{-\alpha f(E-E_{eq})}\right) \quad \text{(Eq.1)}$$

$$k_a = k_a^o\left(e^{(1-\alpha) f(E-E_{eq})}\right) \quad \text{(Eq.2)}$$

where C_o and C_r are the concentrations of the oxidized and reduced species, respectively, and k_c^o and k_a^o are the standard cathodic and anodic rate constants, i.e. the rate constants in the absence of an electrode potential.[4] The last term introduces the electrical portion of electrochemistry, where α is a symmetry coefficient (typically close to 0.5), f is a constant equal to nF/RT (where n is electrons transferred, F is Faraday's constant, R is the gas constant, and T is temperature), E_{eq} is the equilibrium electrode potential, and E is the applied potential. The difference, $E - E_{eq}$, is known as the overpotential, η. By applying an overpotential, the current can flow across the interface. Equation 3 represents the current density (current divided by electrode area);

$$j = nF\left[C_O k_c^o\left(e^{-\alpha f\eta}\right) - C_R k_a^o\left(e^{(1-\alpha) f\eta}\right)\right] \quad \text{(Eq.3)}$$

where $\boldsymbol{j}$ is the net current density (A/cm^2). Note that in this thesis we will use the convention that anodic current has a positive sign, while cathodic current has a negative sign. This is a form of the Butler-Volmer equation of electrode kinetics. The current-potential curve in Figure 1visually represents Equation 3. The net current density is shown as a solid line, while the anodic and cathodic contributions are shown as dashed lines. For large negative overpotentials, the anodic current is negligible; therefore, the total current is the dominated by cathodic current. At large positive overpotentials, the inverse occurs. Furthermore, when deviating from the equilibrium potential ($\boldsymbol{E_{eq}}$), the magnitude increases exponentially. At very large deviations from the equilibrium potential, the current density saturates as diffusion limits the flow of reactants to the electrode surface.[1] This behavior is not predicted by the Butler-Volmer equation, which is only strictly valid for kinetically-controlled electrode reactions.

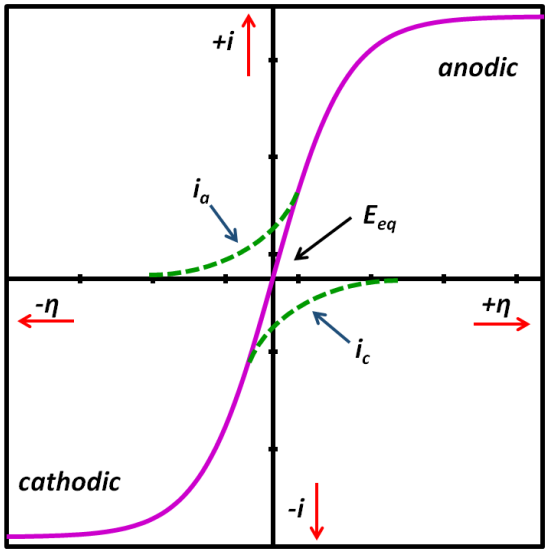

Figure 1. *Current-potential curve where the overpotential, η, is simply the difference between the applied potential and the equilibrium potential.*

At equilibrium, the Butler-Volmer equation simplifies to the well-known Nernst equation for the equilibrium potential across an electrode-electrolyte interface:

$$\boldsymbol{E_{eq} = E^o - \frac{RT}{nF} ln \frac{C_R}{C_O}} \qquad \text{(Eq.4)}$$

where $\boldsymbol{E^0}$, $\boldsymbol{R}$, $\boldsymbol{T}$, $\boldsymbol{n}$, $\boldsymbol{F}$, $\boldsymbol{C_R}$, and $\boldsymbol{C_O}$ are the standard cell potential (V), universal gas constant (8.314 J/K*mol), temperature (K), number of electrons exchanged, Faraday's constant (96,485.3 C/mol), bulk concentration of the cathodic species, and bulk concentration of the anodic species at equilibrium, respectively. Because equilibrium implies the net current is zero, the electrode potential is dependent on the bulk concentrations of the redox species.

1.2. Electrode Reactions

An electrochemical cell is a device where electrochemical measurements can be measured. Electroanalytical techniques typically use a three-electrode system that consists of a working, counter, and reference electrode as seen in Figure 2.

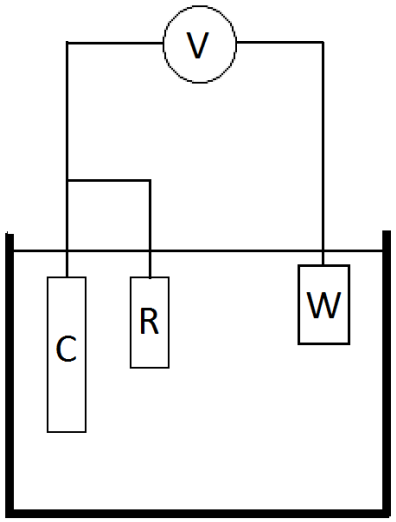

Figure 2. *Schematic of a three-electrode cell. V, C, R, and W represent the potentiometer, counter electrode, reference electrode, and working electrode, respectively.*

The working electrode is where the reaction of interest occurs - electrons are transferred between the analyte and electrode.[1] The size and material of the working electrode is dependent on the type of application. For example, platinum electrodes can be used for electrodeposition of polyaniline[5] and gold electrodes for biomolecular detection.[6,7] These are examples of inert electrodes in which the electrode material itself does not take part in the electrochemical reactions. The counter electrode closes the circuit, allowing current to pass between itself and the working electrode. A counter electrode must have a higher surface area than the working electrode and be inert. This ensures that the reaction on the counter electrode will not dominate the electrochemical behavior.[1] The potential at the working electrode is monitored or applied in relation to the reference electrode, which has a fixed electrode potential. To keep the potential fixed, the reference electrode must include a fast, stable redox reaction, at equilibrium. This electrode, including the solution containing the reference redox species, is isolated from the rest of the cell by a liquid junction.**[1]** A liquid junction is a nonselective interface which allows species from the reference electrode compartment and the rest of the cell to freely mix, albeit at a very small rate to avoid contamination. Silver–silver chloride and the saturated calomel reference electrodes are commonly adopted in the three-electrode system. In this work, the Ag/AgCl reference is used. The redox reaction occurring at the Ag/AgCl electrode is:

$$AgCl_s + e^- \rightleftharpoons Ag_s + Cl^-_{aq} \quad \text{(Rxn.2)}$$

By placing this electrode in a KCl solution of constant Cl^- concentration, the potential is kept constant. Utilizing the three-electrode setup allows the experimenter to effectively monitor any electrochemical responses during measurements.

When performing an electrochemical experiment, the types of electrodes and choice of electrochemical technique must be suitable to the analyte of interest because of the two types of electrochemical responses that occur at the electrode: faradaic and non-faradaic processes. Faradaic current is the current transferred across the electrified interface because of the oxidation and reduction of a species in an electrochemical reaction, as described by the Butler-Volmer equation. Faradaic current obeys Faraday's Law:

$$Q = nFz \quad \text{(Eq.5)}$$

where n is the amount in moles, Q is the total charge, and z is the number of electrons transferred per reaction. Non-Faradaic current is caused by the transient motion of ions in solution as an interface is charged, much like transient current observed across a capacitor.[3] In electrochemical measurements, both types of current exist; however, non-faradaic current should be minimized as it does not report on the nature of the analyte.

As the electrode becomes charged, the ions in the electrolyte are redistributed to balance out the charge on the electrode, forming the electrical double-layer. Both sides of the interface must have equal and opposite charges. While the charges on the electrodes are typically found on the surface, the charges in the solution are distributed away from the interface due to thermal motion of the ions. As shown in Figure 3, the double layer is comprised of several layers. The first is the inner Helmholtz plane where solvent, ions, and molecules are not fully solvated but specifically adsorbed to the electrode surface. The second is the outer Helmholtz plane where ions are nonspecifically bound to the electrode. Further away from the electrodes, the ions are distributed about into the diffuse layer, with decreasing concentration, until the homogenous bulk solution where there is no net charge or chemical/electrical gradients. The structure of the double layer can affect the rate of electrode processes and the non-faradaic current. For example, in reactions with very low concentrations of electroactive species, the non-faradaic current can be much larger than the faradaic current, causing large background currents in voltammetric experiments.[1]

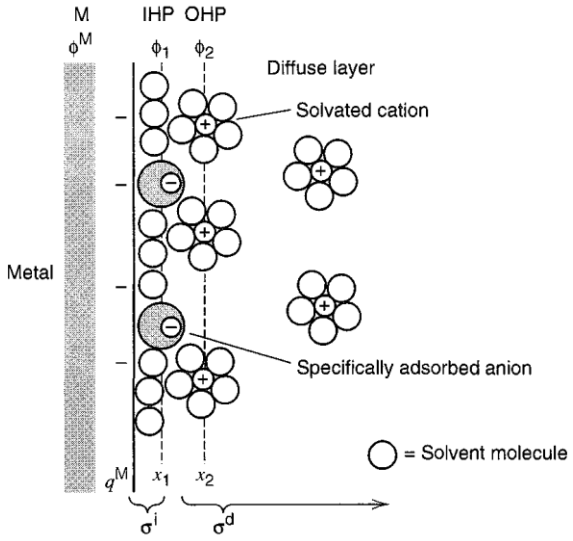

Figure 3. *Pictorial representation of the electrical double layer.* ***M***, ***IHP***, *and* ***OHP*** *represent metal, inner Helmholtz plane, and outer Helmholtz plane, respectively*.[1]

The overall electrochemical behavior is a complex mix of the electrical double-layer effects, electrode kinetics, and mass transport, as shown in Figure 4. The rate of the electrode reaction is dependent on the rate of these processes. It starts with the mass transfer of the oxidative or reductive species from the bulk of the solution to the double layer. Once within the double layer, primarily electron transfer occurs at the electrode surface to reduce or oxidize the species. Other surface chemistries and reactions can occur such as protonation, dimerization, adsorption, crystallization, etc. The various electroanalytical techniques that will be described take advantage of the ease with which electrical parameters (such as potential and current) can be controlled and measured to investigate electroactive molecules by perturbing one or more of the behaviors displayed in Figure 4.

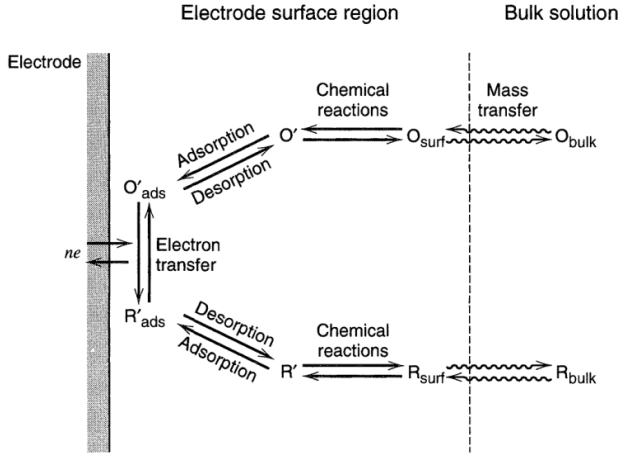

Figure 4. *Pictorial representation of general pathway of an electrode reaction.*

Chapter 2: Electroanalytical Techniques

2.1. Chronoamperometry

Chronoamperometry is an electrochemical technique where the potential of the working electrode is stepped from one potential to another and the current is measured as a function of time. The waveform, shown in Figure 5A, shows the initial potential (E_i), which is held for a chosen amount of time then instantaneously stepped to the final potential (E_f). The response curve displays current as a function of time, shown in Figure 5B.

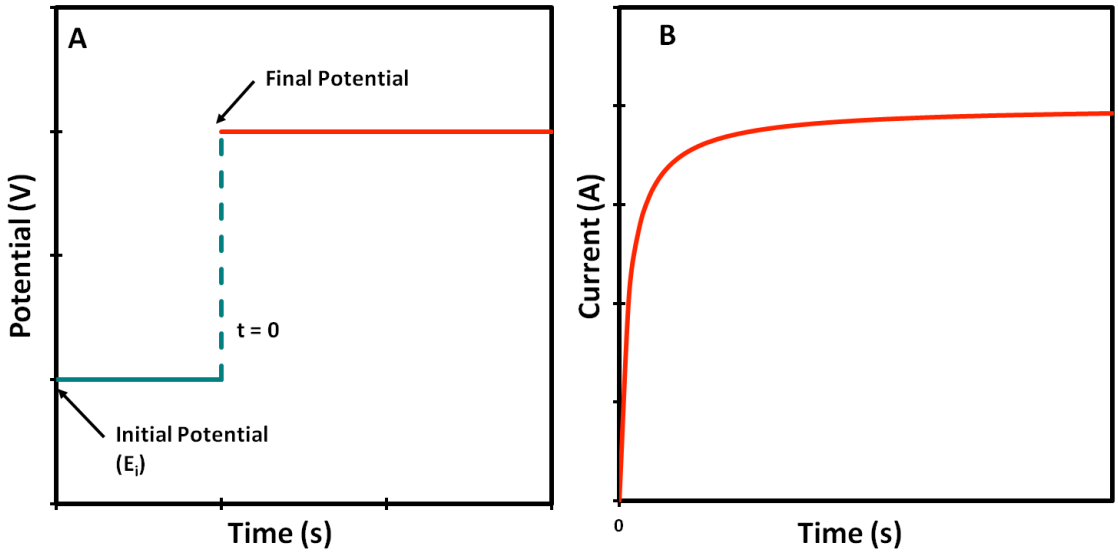

***Figure 5**. Chronoamperometry input waveform (**A**) and measured response curve (**B**)*

Typically, no faradaic processes occur at the initial potential. Then the potential is stepped to a final value where the redox reaction occurs and is diffusion limited. The switch to the final potential is where time is defined at zero, and where current measurement begins. The transient current can be defined as;

$$i_{net} = i_d + i_{cap} \qquad \text{(Eq.6)}$$

where the net current (i_{net}) is the sum of the diffusion limiting current (i_d) and the capacitive current (i_{cap}).[8] The Cottrell equation describes the diffusion limited current as a function of time after the step for semi-infinite planar diffusion, as is expected at a macroscopic electrode like those used in this work;

$$i_d = \frac{nFAD^{1/2}C}{(\pi t)^{1/2}} \qquad \text{(Eq.7)}$$

where n is the number of electrons transferred, F is Faraday's constant, A is the electrode area (cm^2), D is the diffusion coefficient (cm^2/s), C is the concentration (mol/cm^3) and t is time (s).[1] The diffusion limiting current is a faradaic current resulting from the maximum transfer rate of the species.

The capacitive current is given by;

$$i_{cap} = \frac{E}{R_u} e^{-t/R_u C_d} \quad \text{(Eq.8)}$$

where E is the potential, R_u is the uncompensated resistance, C_d is the double layer capacitance, and t is time. At short times, (t < 0.1 s), the capacitive current is a considerable contribution to the net current while at times greater than ~0.1 s, the effect is almost negligible. This equation suggests that the involvement of the capacitive current exponentially decays over time. Moreover, at greater time intervals, the measurement of the diffusion limiting current will be more reliable.

2.2. Chronocoulometry

In chronocoulometry, a potential step is applied to the electrode, like in chronoamperometry, however the charge is measured rather than current. Chronocoulometry offers some advantages over chronoamperometry, such as a signal that increases with time, better signal-to-noise ratio, and ease of differentiating contributions from Faradaic and non-Faradaic reactions.[1]

Generally, a chronocoulometric experiment is plotted as the total charge (Q) versus the square-root of time ($t^{1/2}$) as shown in Figure 6.

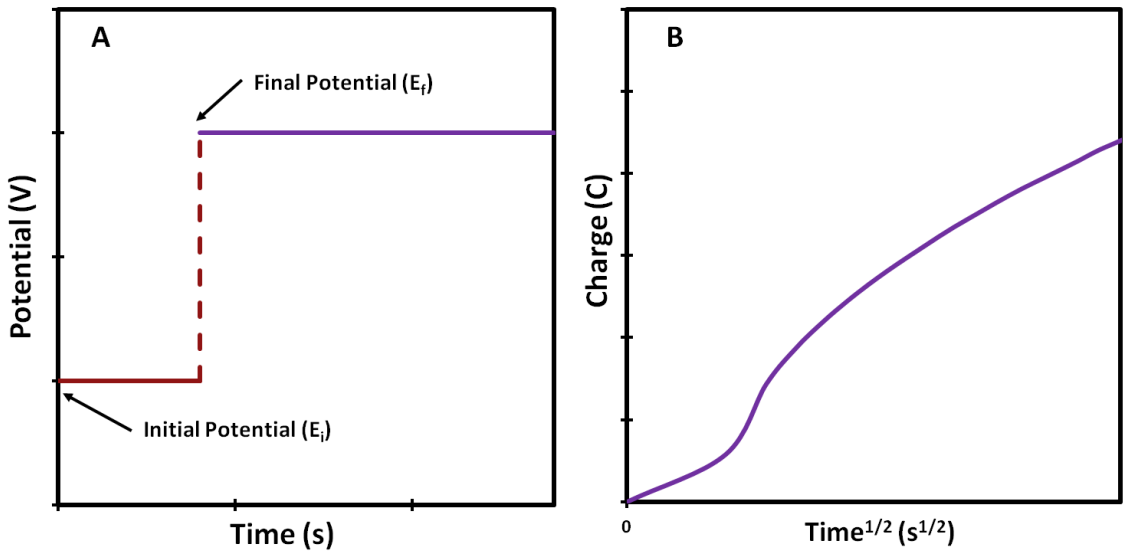

***Figure 6**. Chronocoulometry input waveform (**A**) and measured response curve (**B**)*

The charge, Q, of a chronocoulometry experiment is given by the integrated Cottrell expression along with terms representing the non-Faradaic current and surface-bound species;

$$Q = \frac{2nFAD_0^{1/2}C_0}{\pi^{1/2}} t^{1/2} + Q_{dl} + nFA\Gamma_0 \quad \text{(Eq.9)}$$

where $\boldsymbol{n}$ is the number of electrons per molecule for reduction, $\boldsymbol{F}$ the Faraday constant (C/mol), $\boldsymbol{A}$ the electrode area (cm^2), $\boldsymbol{D_0}$ the diffusion coefficient (cm^2/s), $\boldsymbol{C_0}$ the bulk concentration (mol/cm^3), $\boldsymbol{Q_{dl}}$ the double-layer charge (C), and $\boldsymbol{nFA\Gamma_0}$ is the charge from the reduction of the surface excess ($\boldsymbol{\Gamma_0}$ is the surface coverage in mol/cm^2) of the redox species. The surface excess refers to redox-active species at the electrode surface at the initial instant of the potential step, thus they undergo a Faradaic reaction immediately. A common application of chronocoulometry is to evaluate surface excesses of electroactive species. An example of this application is the quantification of DNA immobilized on a gold surface.[9]

2.2.1. Quantification of Surface-Bound DNA using Ruthenium Hexamine

Steel et al. developed an electrochemical technique now commonly employed to quantify the amount of DNA immobilized on a gold surface using chronocoulometry.[9] This technique utilizes the electrostatic attraction between the negatively charged backbone of DNA and the trivalently charged ruthenium (III) hexamine, $[Ru(NH_3)_6]^{3+}$ (RuHex). The RuHex binds to every three nucleotide base pairs of the DNA strand. The amount of RuHex bound is determined using chronocoulometry, where the Faradaic charge due to the bound RuHex is used to approximate the amount of surface-bound DNA. A scheme of this process is in Figure 7.

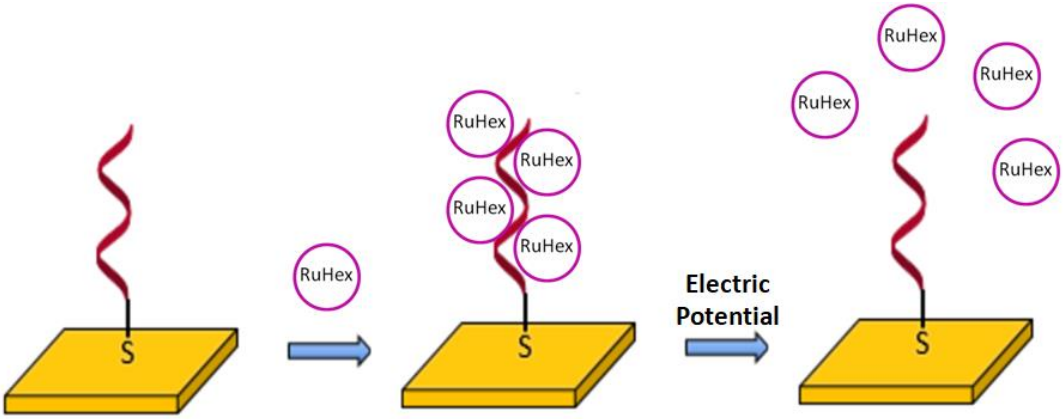

Figure 7*. General Scheme of utilizing RuHex to measure surface coverage. (1) The DNA-modified electrode is incubated in a solution of RuHex and (2) then an electric potential from a chronocoulometry experiment measures the amount the bound RuHex and the RuHex diffuses from the surface.*

To begin our quantification surface-bound DNA, solutions of 10 mM Tris and 50 µM RuHex in 10 mM Tris are degassed and blanketed using nitrogen. The DNA modified electrode is first immersed in the Tris solution. The potential is stepped from +100 mV to -400 mV versus Ag/AgCl and the resulting charge is measured versus the square root of time, Figure 6B. This method is then repeated in the solution of RuHex. To calculate the DNA density on the surface, we must refer to Eq. 14. At time equal zero seconds, the first term is also zero (no species have had an opportunity to diffuse to the surface) and the

chronocoulometric intercept at t=0 s is the sum of the double layer and surface excess charge. The charge from the surface excess (Γ_0) is determined by the difference in the chronocoulometric intercept from the Tris and RuHex measurements. The DNA probe surface density is then determined by a modified form of Faraday's Law;

$$\Gamma_{DNA} = \Gamma_0(Z/m)(N_A) \qquad \text{(Eq.10)}$$

where Γ_{DNA} is the probe surface density (molecules/cm^2), Z is the charge of the redox molecule (+3), m is the number of base pairs in the DNA strand, and N_A is Avogadro's number.

As a control experiment, this method is repeated using an electrode modified with only 6-mercaptohexanol (MCH), Figure 8A. Since there is no electrostatic attraction between RuHex and MCH the difference of the chronocoulometric intercept is zero.

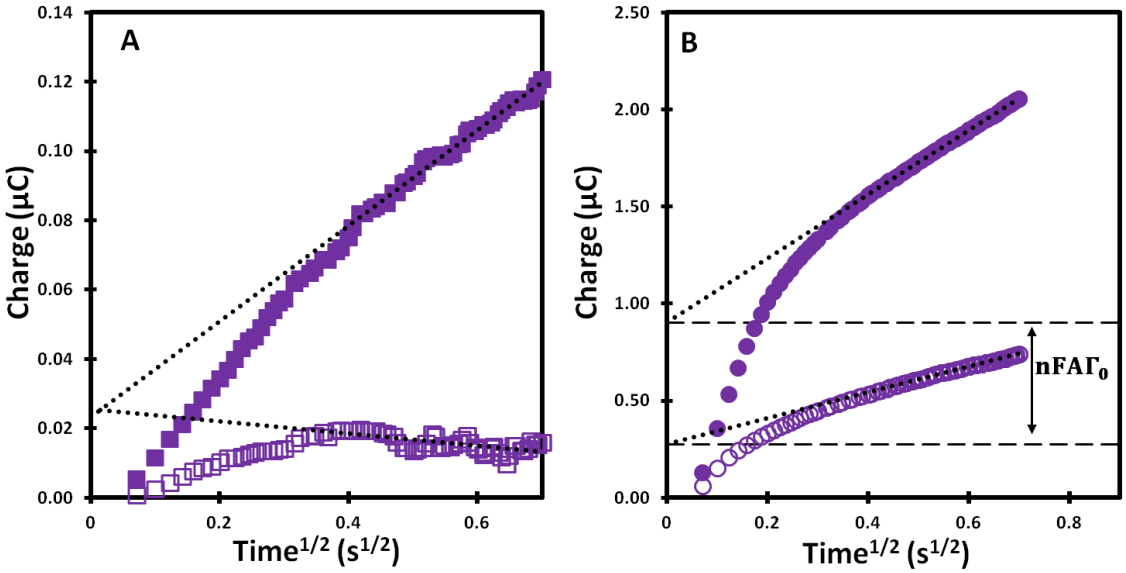

Figure 8. *Chronocoulometric response curves for (**A**) MCH (square) and (**B**) probe/MCH (circle). Open shapes represent measurements done in 10 mM Tris while closed shapes represent the presence of 50 µM RuHex. The difference in intercepts represents the charge of surface excess of RuHex.*

2.3. Cyclic Voltammetry

Cyclic voltammetry is a well-established voltammetric technique and is often the first experiment performed in an electrochemical study of a compound, a biological material, or an electrode surface due to its capability for rapidly observing the redox behavior over a wide potential range.[10] It is a technique in which the applied potential is linearly scanned to a switching potential, then reversed and linearly scanned back to a second switching potential where the cycle is repeated, as shown in Figure 9.

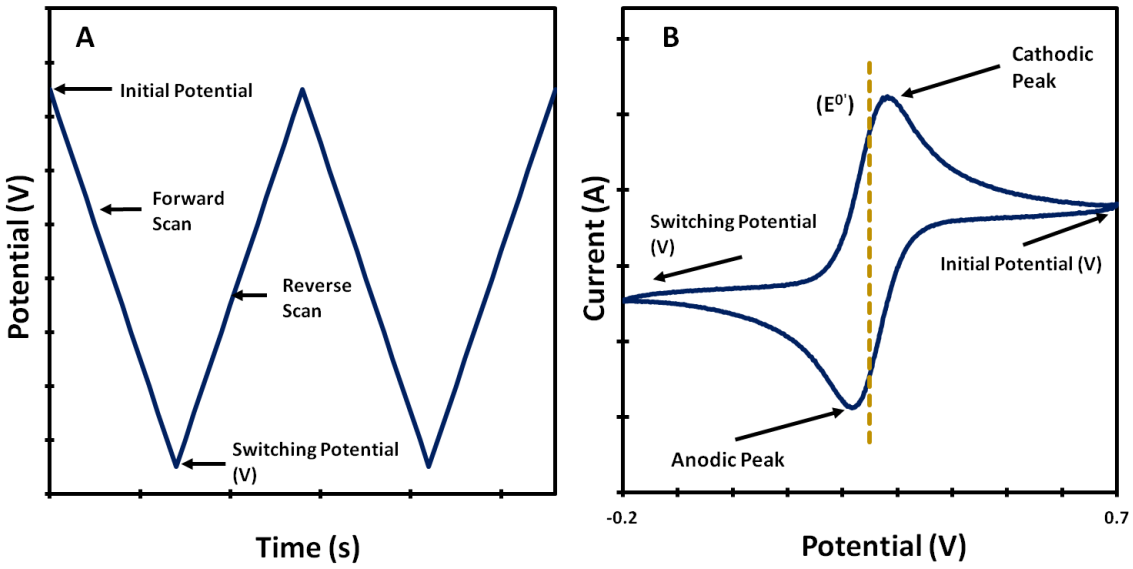

Figure 9*. Cyclic voltammetry input waveform (**A**) and measured response curve (**B**)*

The current is measured and plotted versus the applied potential to give a voltammogram. The switching potentials are chosen based on the electrochemical window of electrolyte and electrode and the potential at which the analyte is oxidized and reduced. Other than the switching potential, another controllable parameter is the scan rate, which allows elucidation of kinetic information.

Consider the reaction of potassium ferrocyanide in Figure 9B. As the scan begins, at -0.2 V (vs. Ag/AgCl), the potential is well negative of the formal potential ($E^{0'}$), thus only the non-faradaic current (ferricyanide is the fully reduced form of the analyte). As the scan approaches the formal potential, the oxidation of the ferrocyanide to ferricyanide begins and anodic current starts to flow. As the potential gets more positive, the current continues to increase as the ferrocyanide at the surface is oxidized at a higher rate (see the discussion of Butler-Volmer kinetics above). Then, the current will reach a maximum and begin to decrease to a steady diffusion-limited current due to the ferrocyanide being depleted at the surface. At this point, the rate of ferrocyanide oxidation, and therefore the current, is determined by the rate at which it can diffuse to the surface from the bulk of solution.

A cyclic voltammogram provides the experimenter with the peak potentials and peak currents of both the forward and backward scans to characterize the redox couple using peak separation and peak ratio. A redox couple is considered reversible when the reaction is fast enough to maintain the concentrations of the oxidized and reduced forms in equilibrium with each other at the electrode surface.[11] One method to determine if a redox couple is reversible is to compare the peak separation of the cyclic voltammogram with the following equation:[10]

$$\Delta E_P = E_{P,A} - E_{P,C} \cong \frac{0.059}{n}\ V \quad \text{(Eq.11)}$$

A redox couple where both species rapidly exchange electrons exhibits a ΔE_P of about 0.059/n V. A slow electron transfer at the electrode surface causes the peak separation to increase. This increase can be caused by an irreversible (or quasi-reversible) redox couple. Moreover, an increase in peak separation also occurs if the quality of the electrode surface is poor or if there is a passivation layer blocking efficient electron transfer. It's important to note that the apparent reversibility of the redox couple also depends on the scan rate chosen. The peak separation increases if the scan rate is too fast. The cathodic and anodic peak current of a simple, reversible, and fast redox couple should also be identical:

$$\frac{i_{pa}}{i_{pc}} = 1 \quad \text{(Eq.12)}$$

Factors that affect peak separation also affect the peak ratio.

The peak current of a cyclic voltammogram can be determined by fitting the baselines of the cathodic and anodic peak and calculating the distance from the peak to the baselines to acquire the peak currents. The peak current for a reversible reaction dependent on scan rate and concentration by the Randles-Sevcik equation;

$$i_p = 268,600 n^{3/2} A D^{1/2} C v^{1/2} \quad \text{(Eq.13)}$$

where i_p is peak current (A), n is the number of electrons transferred, A is electrode area (cm^2), D is diffusion coefficient (cm^2/s), C is concentration (mol/cm^3) and v is scan rate (V/s) at 25 ˚C. The peak current is related to the concentration and scan rate as illustrated in Figure 10. The concentration and square root of scan rate can be plotted versus the peak current, as shown in Figure 10BD. A linear relationship between the variables shows that the redox reaction between ferrocyanide and the electrode is diffusion-limited, as it correlates to the Randles-Sevcik equation.

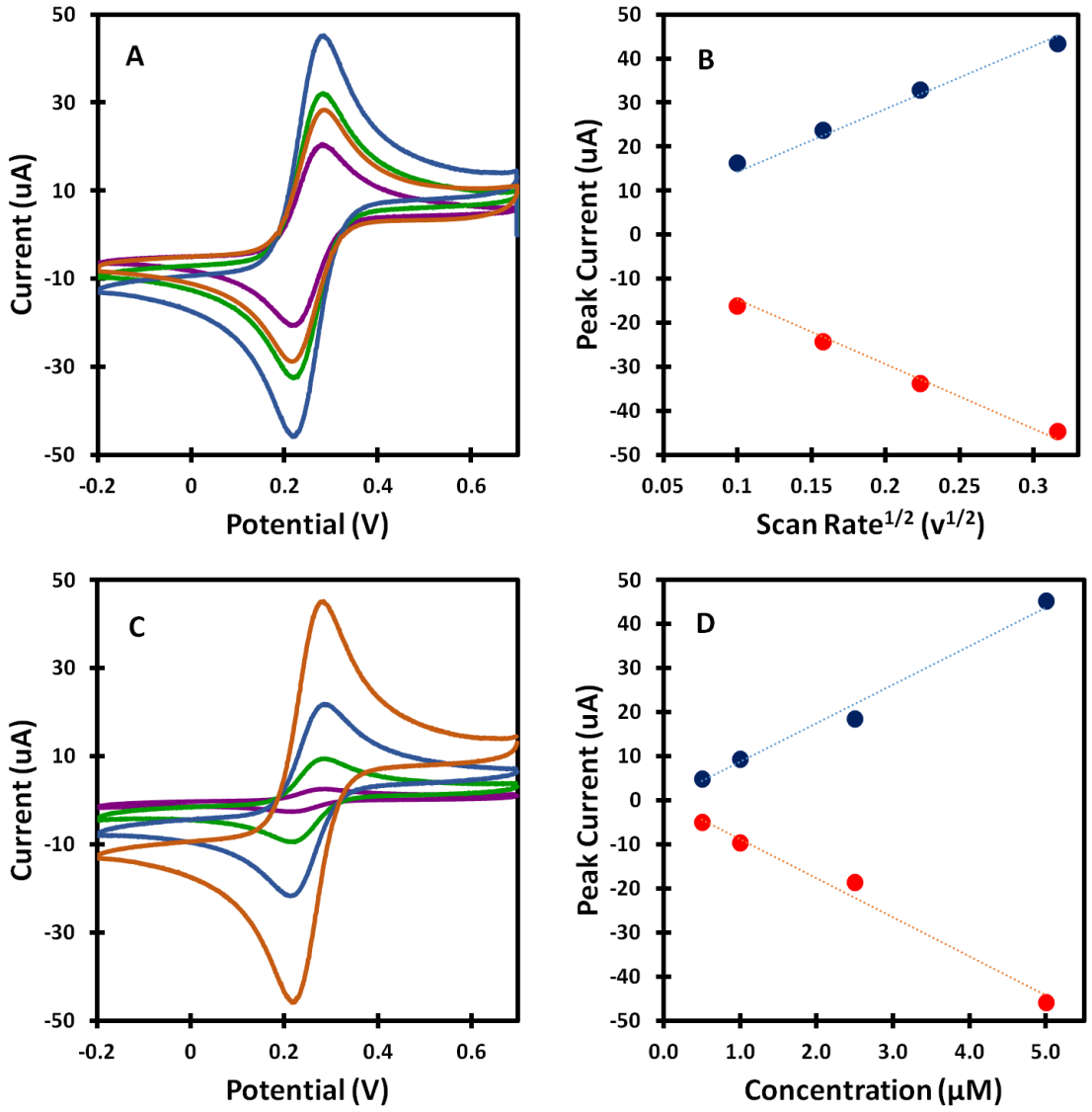

Figure 10. *Effect of **A**) varying scan rate (**purple** – 10 mV/s, **orange** – 25 mV/s, **green** – 50 mV/s, **blue** – 100 mV/s) and **C**) varying concentration (**purple** – 0.5 nM, **green** – 1.0 nM, **blue** – 2.5 nM, **orange** – 5.0 nM). The change in **B**) scan rate and **D**) concentration are plotted versus CV peak current (**red** – anodic peak current and **blue** – cathodic peak current)*

2.3.1. Characterization of Gold Surfaces using Cyclic Voltammetry

Cyclic voltammetry can be used as a tool to assess the condition of the electrode surface. For the experiments in this thesis, it is important for the polycrystalline gold surface to be polished and free of contamination for the formation of a uniform DNA monolayer. The routine consists of a mechanical polishing using alumina slurry, chemical treatment using piranha solution, and electrochemical polishing with sulfuric acid as summarized later in this thesis. Figures 11 and 12 shows typical cyclic

voltammograms of clean gold surfaces in 0.5 M sulfuric acid (Figure 11) and 2.5 mM potassium ferricyanide/ferrocyanide (Figure 12).

As the potential is swept is the positive direction in sulfuric acid, gold oxide is formed on the surface. It is then reduced as the potential is swept back.[12] The reduction of gold oxide results in a single, clear peak. Repeated scans in sulfuric acid result in a rearrangement of surface Au atoms. A clean, uniform surface will display characteristic, sharp peaks in the voltammogram, as shown in Figure 11. Any secondary peaks, broadening, or shouldering of the peaks may be a result of contamination on the surface or in the solution.

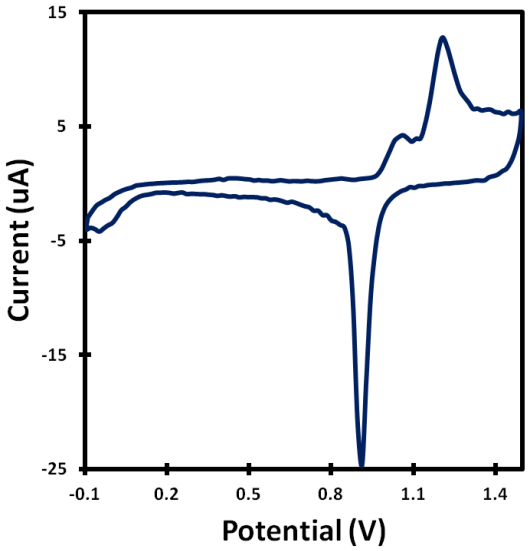

Figure 11. *Cyclic voltammogram of 0.5 M H_2SO_4 using a gold working electrode*

The peak separation and peak ratio of cyclic voltammograms in ferrocyanide/ferricyanide are also used to determine the cleanliness of the electrode surface calculate. Figure 12 illustrates how the electrode surface can affect a cyclic voltammogram. Visually, the peak currents of the polished surface (blue) are higher and the peak separation is smaller than the contaminated surface (red). Table 1 compares peak separation, peak ratio, and surface area of the two different surfaces. The peak ratio between the two is similar. However, the peak separation of the dirty electrode is outside the acceptable range. The geometrical surface area of the polycrystalline gold electrode is 0.0314 cm^2 calculated using the known radius of the gold disc electrode. The peak current of the CV determines the surface area. The surface area of a clean and smooth electrode should be close to the geometrical area.

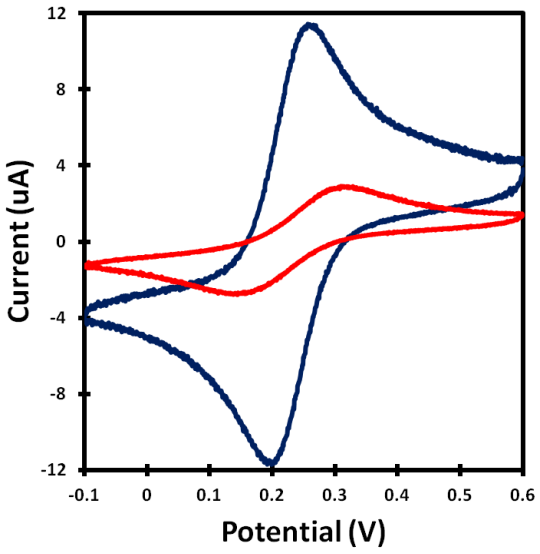

***Figure 12**. Cyclic voltammogram of 2.5 mM Ferricyanide using a gold electrode before (**red**) and after (**blue**) surface polishing*

***Table 1**. Characterization of Gold Surface Before and After Electrochemical Polishing*

	Before	**After**
Peak Separation (V)	$0.3095 - 0.1442 = 0.1653\ V \neq 0.059V$	$0.2564 - 0.1984 = 0.0579V \cong 0.059V$
Peak Ratio	$\frac{2.71E-6}{2.98E-6} = 0.91 \cong 1$	$\frac{11.42E-6}{11.72E-6} = 0.97 \cong 1$
Surface Area (cm^2)	$\frac{2.98E-6}{2.69E5(1)^{1.5}(6.7E-6)^{0.5}(1.0E-6)(0.05)^{0.5}}$ $= 0.0076\ cm^2 \neq 0.0314\ cm^2$	$\frac{11.72E-6}{2.69E5(1)^{1.5}(6.7E-6)^{0.5}(1.0E-6)(0.05)^{0.5}}$ $= 0.0300\ cm^2 \cong 0.0314\ cm^2$

2.4. Square Wave Voltammetry

Square wave voltammetry (SWV) is a more recent electrochemical technique developed by Ramaley and Krause in 1969.[13] The SWV waveform is a bipolar square wave that is superimposed on a staircase wave. Various parameters, shown in Figure 13A, characterizes the waveform. The amplitude (ΔE_p, mV) is the height of the pulse. The period (τ, s), or frequency ($f = 1/\tau$, Hz), is the length of time required to complete an up and down pulse. The increment (ΔE_s, mV) is the rise or fall in the potential after each period. Current samples are taken twice per cycle, at the end of each pulse. The forward current, i_f, arises from the first pulse per cycle, which is in the direction of the staircase scan. The reverse current, i_r, is taken at the end of the second pulse, which is in the opposite direction. A difference current,

Δi, is calculated as $i_f - i_r$. The result of a single SWV run are three voltammograms showing forward, reverse, and difference currents vs. the potential as shown in Figure 13B. The following equation depicts the difference in peak current;

$$\Delta i_p = \frac{nFAD^{1/2}C}{(\pi t_p)^{1/2}}\Delta\psi_p \quad \text{(Eq.14)}$$

where t_p is the pulse width (s) and $\Delta\psi_p$ is the dimensionless peak current. The $\Delta\psi_p$ gauges the peak height in SWV relative to the limiting response in normal pulse voltammetry.[1] Like CV, the concentration is proportional to the difference current of a SWV voltammogram. This difference of current is one of the advantages of SWV because the effects of non-faradaic current and the large unstable background are subtracted out.[14] This also gives SWV higher sensitivity, being able to detect down to 10 nM. The general rule when determining the parameters are as follows:

$$\Delta E_p(mV) = \frac{50}{n} \quad \text{(Eq.15)}$$

$$\Delta E_s(mV) = \frac{10}{n} \quad \text{(Eq.16)}$$

where n is the number of electrons transferred. For the redox reaction of methylene blue, the net electrons transferred is 2; therefore, our SWV parameters are ΔE_p = 25 mV and ΔE_s = 5 mV.

Another advantage to using SWV is its high effective scan rate. Typically, with voltammetric techniques, like CV, a high scan rate could distort the current-voltage curve by introducing uncompensated resistance.[1] Unlike cyclic voltammetry, SWV can reach a reach scan rate to about 1 Vs^{-1} giving the user a shorter analysis time. The high speeds also lower the consumption of electroactive compounds and fouling of the electrode surface.

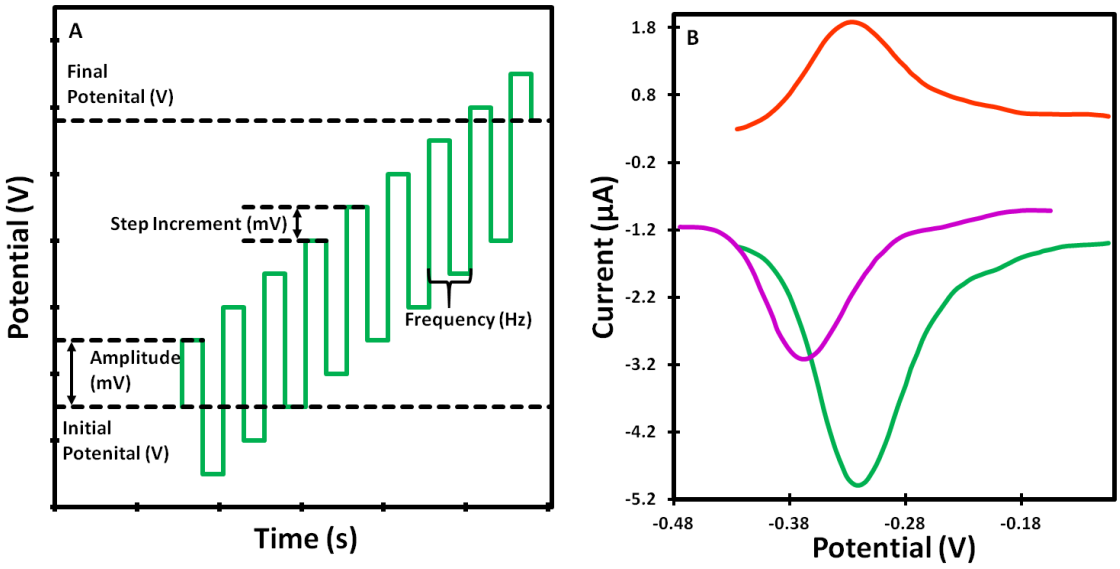

***Figure 13**. Square Wave Voltammetry input waveform (**A**) and measured response curve (**B**) (**purple** – forward current, **orange** – reverse current, and **green** – difference)*

2.4.1. Square Wave Voltammetry of Methylene Blue

Intercalators, inserters, and covalently-tethered electrochemically active molecules are species reported for the electrochemical detection of DNA. [19-21]Among these redox species, methylene blue (MB) has been intensively studied. Methylene blue is an aromatic heterocycle that forms leucomethylene blue when reduced with the addition of two electrons and one proton, as shown in Figure 14.[15]

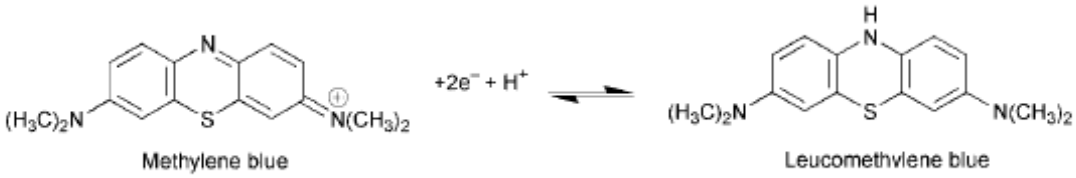

***Figure 14**. Redox Reaction of Methylene Blue*

As an intercalator, MB can insert itself into the stacked, planar bases of DNA. The electronic coupling between the MB intercalator and the π stack of DNA is important for DNA-mediated charge transport.[20] CV and SWV voltammograms were taken of MB-tethered DNA duplexes (Figure 15). Poor peak definition and large peak separation in the CV voltammogram indicates slow-electron-transfer kinetics and prevents confident analysis of MB-DNA complexes. However, using SWV offers clear resolution of peaks due to its ability to lower non-faradaic current. The data shows that MB reduction is reversible and detectable at low concentrations. Not only is MB a reversible redox couple, it is also a strong intercalator with a binding constant of ~ 10^6 M^{-1}.[20-21] In Chapter 3, we explore the use of the

covalently tethered MB to provide insight into the electrochemical melting of DNA for kinetic studies and biosensing applications.

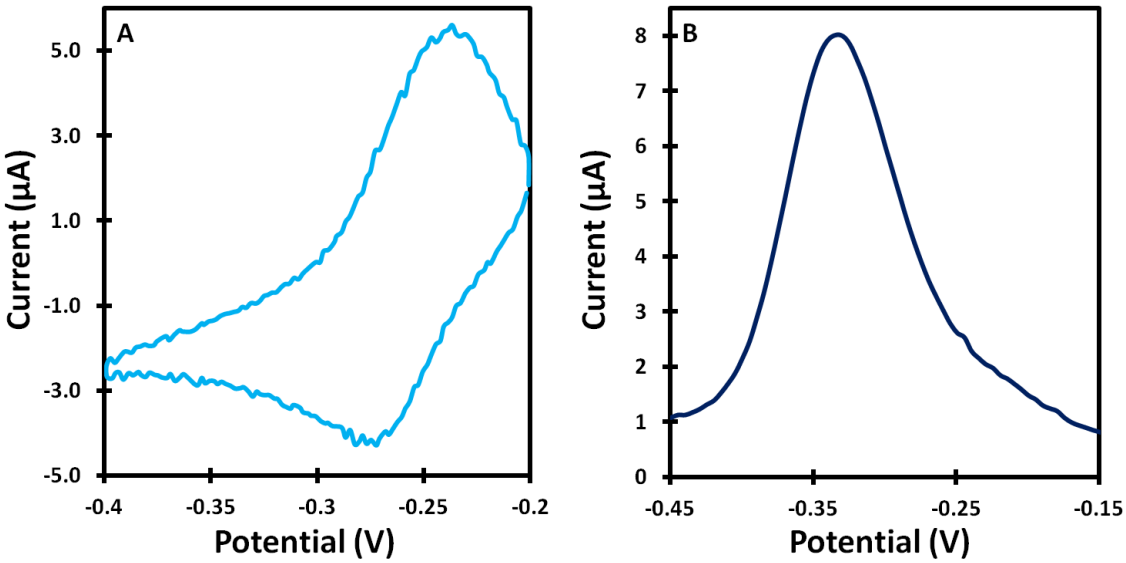

Figure 15. *Cyclic voltammogram (A) and Square Wave Voltammogram (B) of MB-tethered DNA*

Chapter 3: Review of DNA Biosensors

3.1. General DNA Concepts

DNA is an organic molecule, consisting of a chain of nucleotides, which create the genetic makeup and functionality of life. Each nucleotide contains three covalently bonded components: a phosphate group, deoxyribose sugar, and a nitrogenous base, as shown in Figure 16A. These bases are adenine (A), guanine (G), cytosine (C), and thymine (T). Adenine and guanine have a purine ring while thymine and cytosine have pyrimidine rings. Through phosphodiester bonding, these nucleotides form a long chain, commonly known as single-stranded DNA (ssDNA). Hydrogen bonding between complementary bases (adenine with thymine, guanine with cytosine), antiparallel to one another, forms double-stranded DNA (dsDNA), through a process called hybridization. When the duplex is formed, major and minor grooves form, alternating throughout the length of the dsDNA. The grooves play a rolein the binding of proteins and small molecules. The backbone bases of a major groove are typically deeper and farther apart compared to the minor groove. The major groove usually binds to specific sequences, via the insertion of the alpha helix of a protein, while protein can bind nonspecifically to the minor groove through interactions with the beta strand.[17] The deoxyribose sugar ring also plays an important role in the DNA duplex. Figure 17 shows a furanose ring and torsion of the bonds. The flexible ring can adopt different puckering conformations based on the twisting of the bonds, altering the orientation of the phosphate backbone and nitrogenous bases.[18] The C2' and C3' carbons are displaced above (endo-) the plane of the C1', C4' and O' atoms. The typical DNA duplex has a sugar pucker conformation of C2'endo. This section will provide an in-depth discussion on the different forms of DNA.

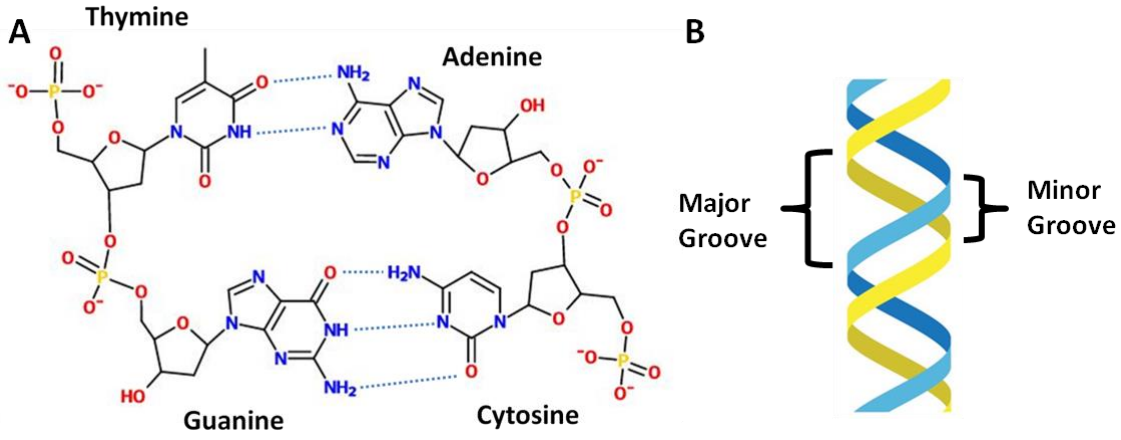

Figure 16. A) *Schematic diagram of the structure of the four nucleotide bases hydrogen bonded to their respective pairs (blue dotted line).* ***B)*** *Typical hybridized DNA duplex with the major and minor grooves labeled.*[29]

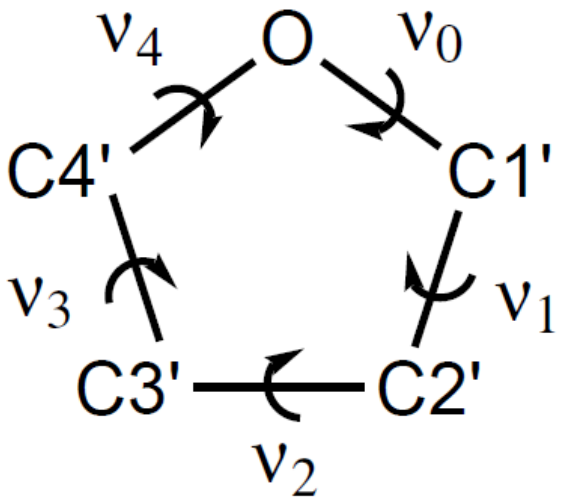

***Figure 17**. Furanose ring system of the deoxyribose sugar group. ν_n represents the possible areas of bond torsion that cause the sugar puckering around the ring.*[19]

There are four levels of DNA structure: primary, secondary, tertiary, and quaternary. The primary structure of DNA refers to the base pair sequence of a linear chain of nitrogenous bases, sugars, and phosphate groups (i.e. single stranded DNA). The secondary structure refers to the bases interacting with one another along the same chain or different chains. Besides formation of the double helix, base-pairing within the same chain can lead to structures such as stem-loops (or hairpins) and pseudoknots, as shown in Figure 18. Hairpins are formed when ssDNA self-hybridizes due to the sequence itself, temperature, or mismatches. These hairpins adds instability in a DNA helix but can be essential for biological functions, such as RNA hairpins regulating gene expression in *cis* or *trans*, serving as binding cites for various proteins, or act as substrates for enzymatic reactions.[20] Pseudoknots are formed when the bases in a loop of a hairpin form intramolecular pairs with the bases outside of the stem, causing a second loop. These pseudoknots have a diverse set of biological roles such as forming the catalytic core of various ribosomes, self-splicing introns and telomerase, and altering gene expression by inducing ribosomal frameshifting in many viruses.[21]

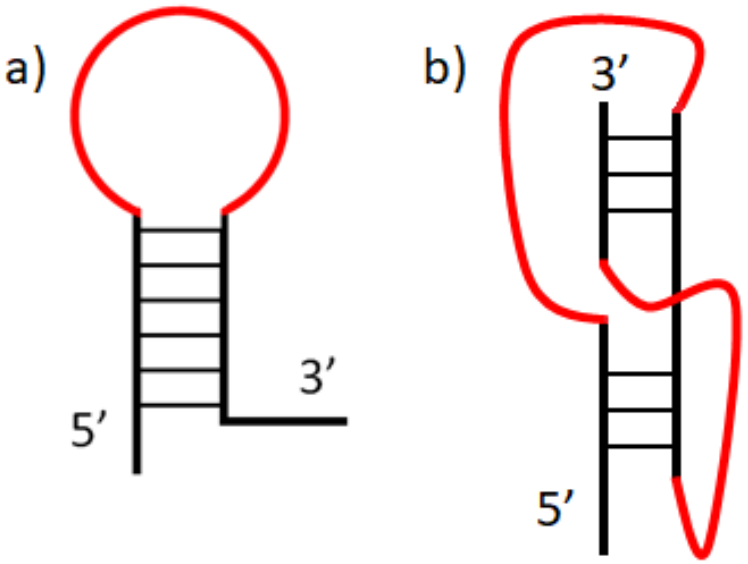

***Figure 18**. Pictorial representation of a) self-dimer stem loop/hairpin, b) psuedoknot secondary DNA structures. The red represents non-hybridized ssDNA involved in the loop.*

Tertiary structures are the three-dimensional conformation of DNA, which includes the hairpons and psuedoknots discussed above, as well as the various forms of the double-stranded DNA helix. DNA helices exist in different configurations such as, B-DNA, A-DNA, and Z-DNA, as shown in Figure 19. B-DNA is the most common form of the dsDNA found by Watson and Crick, which is formed under typical physiological conditions. This duplex is a right-handed helix that contains 10.5 base pairs per turn, 3.4 Å between each base pair, and a diameter of 20 Å.[22] A-DNA is a high-energy conformation that occurs under dehydrated conditions i.e. reduced water or high solvent/salt concentrations.[23] Similar to B-DNA, A-DNA is right-handed but has 11 base pairs per turn, 2.55 Å between each base pair, a diameter of 23 Å and the sugar puck has a C3' endo conformation.[22] A-DNA is common in DNA-RNA duplexes as it is more stable in transcription than B-DNA. Furthermore, the changes to the major and minor grooves allow certain proteins, such as TATA-box binding protein (TBP) and Escherichia coli cyclic AMP receptor protein (CAP), to bind better.[17,22] Z-DNA is a left-handed conformation that has a zigzag backbone pattern which is caused by alternating purine–pyrimidine bases, $(GC)_n$, and the sugar ring conformation is C2' endo – C3' endo.[24] The duplex of Z-DNA has 12 base pairs per turn, 3.8 Å between each base pair, and a diameter of 18 Å.[25] The differences in structure allows for certain proteins to be enhanced more when bound to Z-DNA than B-DNA, for example proteins in mRNA editing.[17]

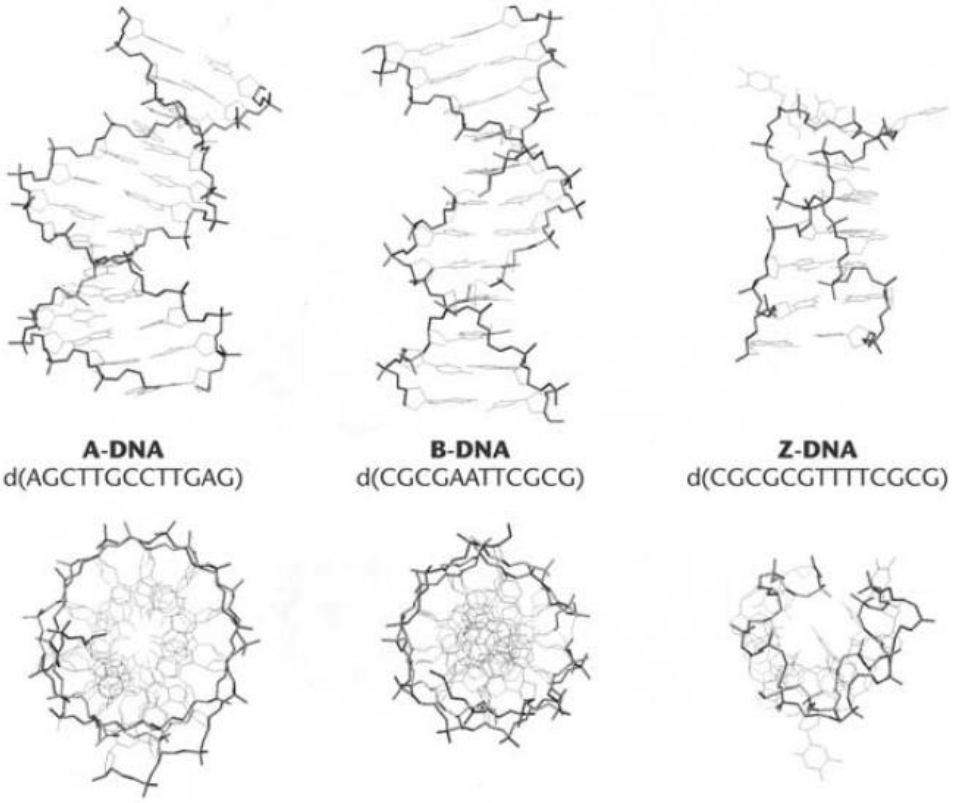

***Figure 19**. A side view (upper portion) and top view (low portion) of A-, B-, and Z-DNA helix.*[17]

***Table 2**. Summary of the DNA confirmations and their differences*

	B – DNA	***A – DNA***	***Z – DNA***
Helix Rotation	Right Handed	Right Handed	Left Handed
Base Pairs per Turn	10.5	11	12
Helix Diameter (Å)	20	23	18
Distance between Bases (Å)	3.4	2.55	3.7
Glycosidic Bond	anti	anti	anti and syn
Major Groove	Wide/Deep	Narrow/Very Deep	Flat
Minor Groove	Narrow/Deep	Shallow/Very Broad	Very Narrow/Deep
Sugar Pucker	C2′ endo	C3′ endo	C2′ endo and C3′ endo

Other tertiary structures of DNA include the cruciform, Holliday junction, triplex, and G-quadruplex. Cruciforms (Figure 20a) are likely to form when DNA sequences contain palindromes, or an inverted repeat, and after DNA recombination creates a four-way junction which two hairpins. Cruciform structures are targets for architectural and regulatory proteins such as junction-resolving enzymes, DNA repair proteins, transcription factors, proteins involved in replication, and chromatin-associated proteins.[26] The Holliday junction is type of cruciform; however, its four-way junction is caused by four individual strands (Figure 20b). They also target architectural and regulatory proteins and they exist in two

conformations; folded and unfolded. In the unfolded conformation (Figure 20c), the junctions are perpendicular to one another (occurring at low ionic strength). When folded, the junctions take on a more X-shape and can be modeled with two duplexes exchanging strands at the junction point in high ion concentrations.[27] The triplex (H-DNA, triple helix) occurs when ssDNA binds to the major groove of a purine-rich B-DNA helix through Hoogsteen hydrogen bonding. Hoogsteen hydrogen bonding refers to the base pairing between the Watson-Crick base pairs (A-T, G-C) and a base (thymine or a protonated cytosine) under acidic pH values in the absence of Mg^{2+} or in a high degree of negative supercoiling.[28] Figures 21a and 21b depict the Hoogsteen hydrogen bonding of DNA bases and the triplex that it forms. Introducing a third strand into the duplex allows for multiple applications such as targeting gene for therapeutics,[29] modulating gene expression by promotion of transcription inhibition,[30,31] and stimulating DNA repair in breast cancer.[32] G-quadruplexes form from sequences that are guanine-rich. The guanines form a planar tetrad though a cyclic Hoogsteen hydrogen bonding in which each guanine makes two hydrogen bonds with its neighbor (Figure 22). These planar tetrads stack on top of each other, forming a quadruplex, helical structure that is dependent on monovalent cations, such as K^+ or Na^+. Moreover, it can form intramolecularly or intermolecularly, as shown in Figure 22.[33] The G-quadruplex structure has been shown to be an inhibitor of telomerase activity. Telomerase is upregulated in most cancer cells and can promote the lifespan of malignant cells. [33,34]

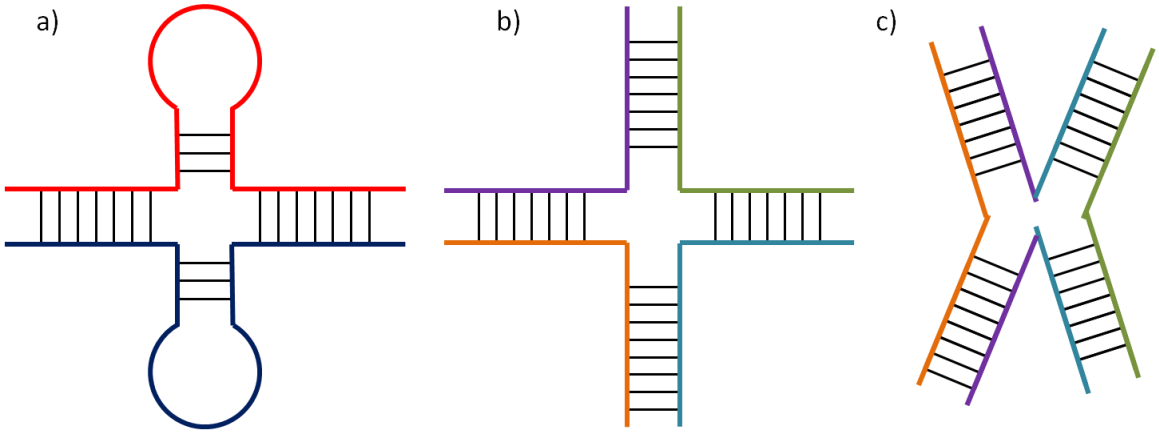

***Figure 20**. Pictorial representation of **a)** typical cruciform **b)** unfolded Holliday junction and **c)** folded Holliday junction tertiary DNA structures. The various colors represent different strands of DNA.*

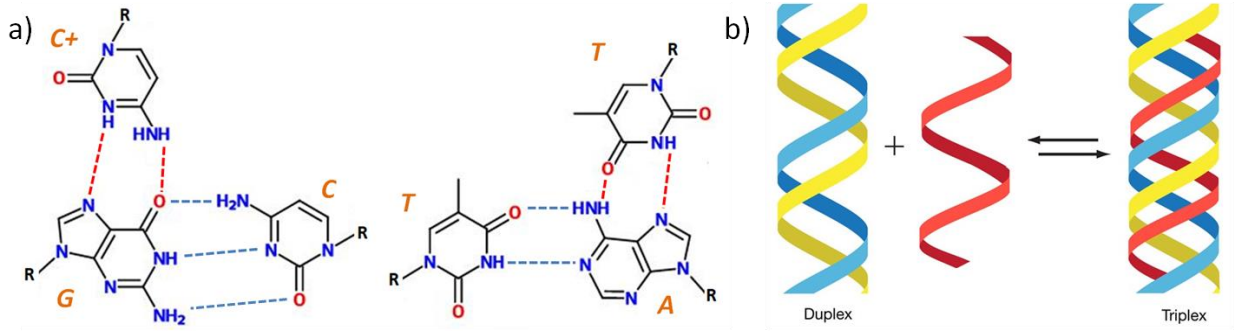

Figure 21. ***a)*** *Schematic illustration of A-T/G-C Watson-Crick base pairing (**blue dashes**) and Hoogsteen base pairing (**red dashes**). **R** groups represent the phosphate and deoxyribose sugar groups. Bases are denoted in **orange**, note that the cytosine involved in the Hoogsteen base pairing is protonated.* ***b)*** *Schematic illustration of the formation of a triplex.*[29]

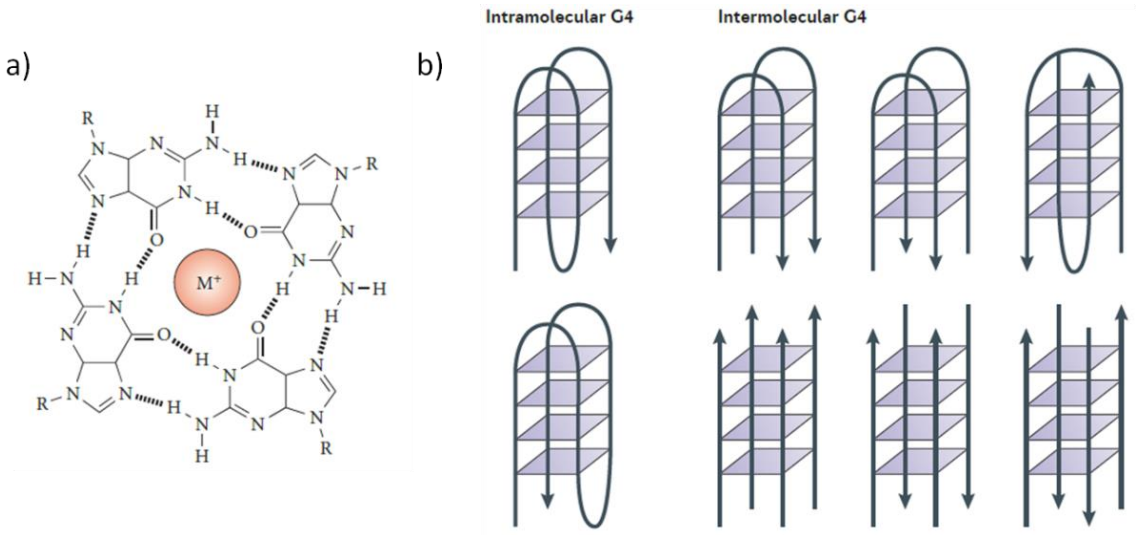

Figure 22. *Schematic illustration of G-quadruplex.* ***a)*** *Four guanine forms the tetrad through Hoogsteen hydrogen bonding* ***b)*** *the stacking of the tetrads form the G-quadruplex.*[34]

Quaternary structures refer to complexes formed between DNA molecules and proteins or other molecules. A well-known quaternary structure is the interaction between DNA and histone. Histone is shown to interact with DNA through non-specific electrostatic binding sites and to have little binding energy associated with it. Together, they form chromatin which serves as the primary substrate for all DNA-related processes.[35,36]

3.2. DNA Melting

The hydrogen bonding along with the π-stacking effect of the base pairs stabilizes the DNA duplex. [110] A measurement of dsDNA stability is defined by melting temperature of the duplex. The temperature at which the concentration of ssDNA and dsDNA are equal. The determination of melting

temperature is typically carried out using UV absorbance. The temperature of a cell containing a solution of dsDNA is increased incrementally. Meanwhile, a detector measures the UV absorbance of the solution at 260 nm (ssDNA absorbs more strongly at 260 nm than while dsDNA does).[37] The resulting curve is sigmoidal as shown in Figure 23. The midpoint of the sigmoid, or the peak of its first derivative, indicates the melting temperature of the DNA duplex.

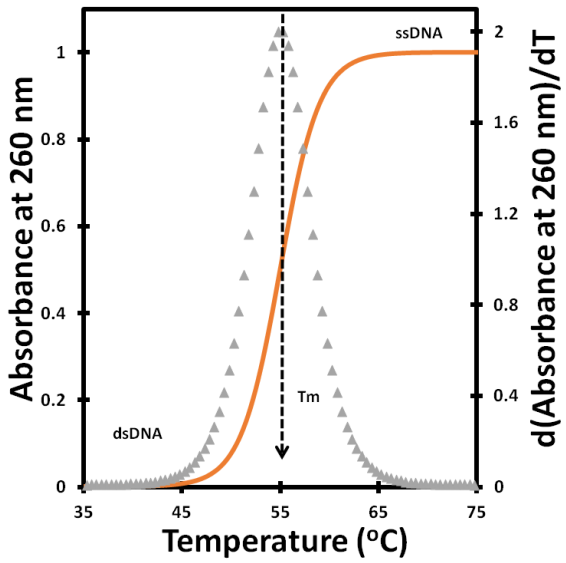

Figure 23. ***Orange*** *– Melting curve displaying the change in Absorbance at 260 nm as a function of temperature and the transition from dsDNA to ssDNA. The plot is overlaid with the first derivative of the melting curve (**Gray**) where the peak represents the melting temperature (T_m).*

The stability and melting temperature of DNA can be affected by GC content, sequence length, ionic strength, and the presence of mismatches or other base pair mutations. Increased GC content in the sequence increases the melting temperature of the duplex. This is because the GC base pair shares 3 hydrogen bonds while the AT base pair shares two. The melting temperature also increases as the length increases due to more hydrogen bonds. The melting temperature of DNA increases by 2 °C for every A:T pair and 4 °C for every G:C pair.[38] As ionic strength decreases, the melting temperature decreases due to the increased electrostatic repulsion between the negative phosphate backbones of the two DNA strands.[39] Conversely, an increase in ions will screen the negative charge of the backbone, reducing the electrostatic repulsion and increasing the stability of the duplex. Finally, DNA mutations, such as sequence mismatch, deletion, or insertion, disrupts the hydrogen bonding and π-stacking, which lowers the stability and affects the shape and melting temperature of the curves. These mutations can cause diseases and cancers by inhibiting or disrupting normal functions of a cell. In this work, a method of discriminating between complementary and mismatched DNA will be described that relies on the melting of duplex DNA at room temperature via electrostatic repulsion at a charged interface.

3.3. Standard Methods for Detecting DNA

Before an in-depth conversation about surface-based DNA sensors, we shall discuss two well-known standard solution-based techniques of DNA detection; polymerase chain reaction (PCR) and high-resolution melting (HRM). PCR is a biological technique capable of amplifying DNA and RNA sequences. The mechanism of PCR consists of three steps; (1) denaturation of dsDNA to ssDNA, (2) annealing of a primer, short DNA molecules, to the single stranded target DNA, and (3) the extension of the primer by using DNA polymerase to attach nucleotides. This step is then repeated 25-35 times to produce exact copies of the target DNA (Figure 24).[40]

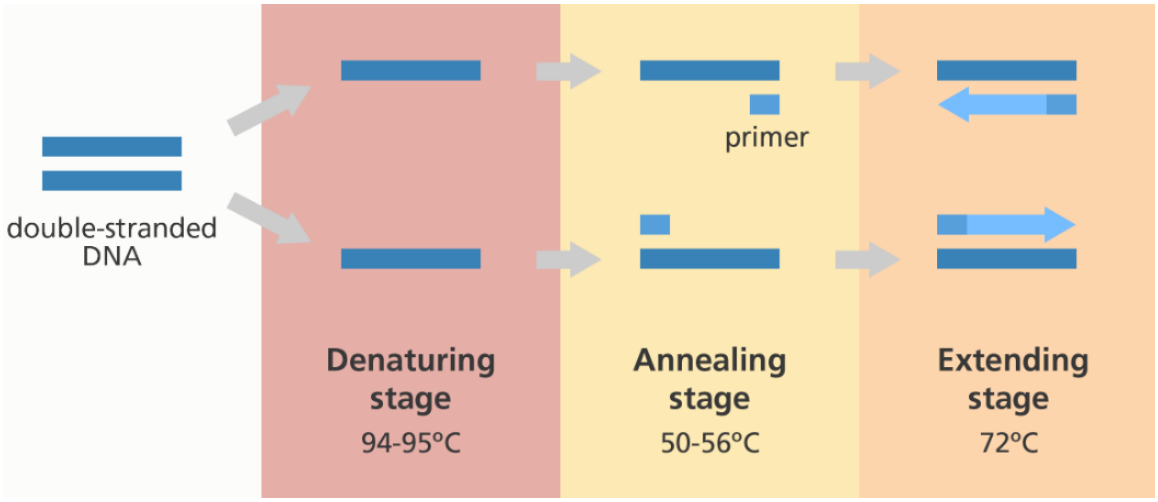

Figure 24. *Three steps of PCR: denaturation, annealing, and extension.*[41]

PCR can also be used to detect, characterize, and quantify nucleic acids in a technique called quantitative PCR (qPCR). This technique utilizes dye-based and/or probe-based labeling to quantify DNA hybridization for mismatch detection and forensics. In dye-based PCR, a dye is used to measure the fluorescence after each PCR cycle. As the amount of DNA increases, the fluorescence increases as well.[42] This method can be applied to forensics by detecting trace amounts of male DNA in a vast excess of female DNA[43] and quantifying human blood samples.[44] However, insufficient concentrations of the PCR product may yield false sex reports. DNA fluorescent qPCR kits such as Quantifiler® and Quadruplex® are sensitive enough to detect 32 – 44 picograms of DNA. However, the dye may bind to any dsDNA present.[45] The results may include false positives and will not report on the degradation of the PCR products. In probe-based PCR, a type of probe is the hydrolysis probe[46], which incorporates a fluorophore and quencher. During annealing, the hydrolysis probe binds to the target sequence. The fluorescence of the probe is quenched. During extension, the probe is hydrolyzed the signal from fluorescence increases as the proximately of the fluorophore and quencher increases (Figure 25).[46] The probe-based PCR is much more specific than the dye-based method. According to Ziola's group, the use of a hydrolysis probe

allows for a detection limit of 2.5 – 10 CFU (or Colony Forming Unit) of *Firmicutes*, beer spoiling bacteria, per packaged 341 ml bottle or can of beer. However, they reported that the hydrolysis probe was not sensitive enough to differentiate between the wild type and 2-bp mismatch strands.

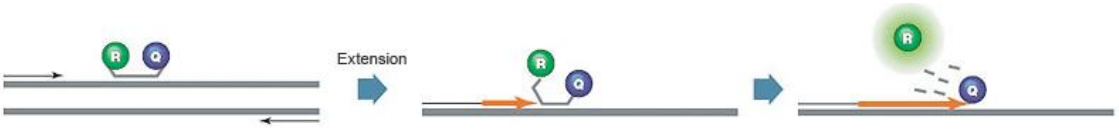

Figure 25. *Hydrolysis probe during the annealing and extension process of PCR.*[46]

High resolution melting (HRM) utilizes improved instrumentation and software to analyze PCR products for variant scanning and genotyping. HRM analysis is a faster, simpler, and less expensive method compared to the classical melt curve analysis.[47] HRM analysis eliminates the need for oligonucleotide probe modifications on the PCR products. In lieu of probes, dsDNA binding dyes are used which exhibit high fluorescence signal when bound to dsDNA and low fluorescence when unbound (ssDNA present). Furthermore, HRM curves provide the user with two observations. As stated in the previous section, changes in the melting temperature or curve shape is due to variation in the sequence and base pairing mismatches of the PCR products.[48] A study was done using HRM to differentiate between eight poxviruses. Although the classical melting curve analysis was sufficient enough to detect and differentiate the eight poxviruses, HRM analysis resulted in a clearer view of separation; showing the advantage HRM has over the classical method.[49] The disadvantages of PCR and qPCR are the nonspecificity of the dye/probe. The use of HRM allows for mutation detection, such as cancer causing the KRAS gene, with a detection limit of 3% for KRAS for a 114 bp sequence.[50,51] However, the cost is relatively high, due to the need for highly effective instrumentation and dyes.[47] Therefore, it does not offer the potential for portable application that surface-based DNA sensors could provide.

3.4. Surface-Based DNA Sensors

DNA sequences are manufactured using techniques and instruments such as the 454Genome Sequencer FLX. This allows experimenters to fabricate sequences specific to an organism, function, or disease. Detailed descriptions of these instruments and techniques can be found in literature.[52,53] Once sequenced and purified, DNA can then be quantified and detected. This section will discuss the methodology and fabrication of surface-bound DNA biosensors as a potentially complementary suite of techniques to the laboratory-based techniques described in the last section.

DNA biosensors report on the hybridization and/or denaturation of dsDNA. These sensors offer sensitive and selective sensing for DNA, proteins, and small molecules. The development of DNA biosensors has various applications such as medical diagnostics/screenings and forensics. Surface-bound

detection offers the ability to produce simple, portable biosensors.[54-56] A general schematic of a DNA biosensor is show in Figure 26. The biosensor consists of an analyte (target DNA) being detected by the molecular recognition element (probe DNA). The hybridization of the analyte causes a physical/chemical change which is then converted into a measurable output signal using a mode of signal transduction.

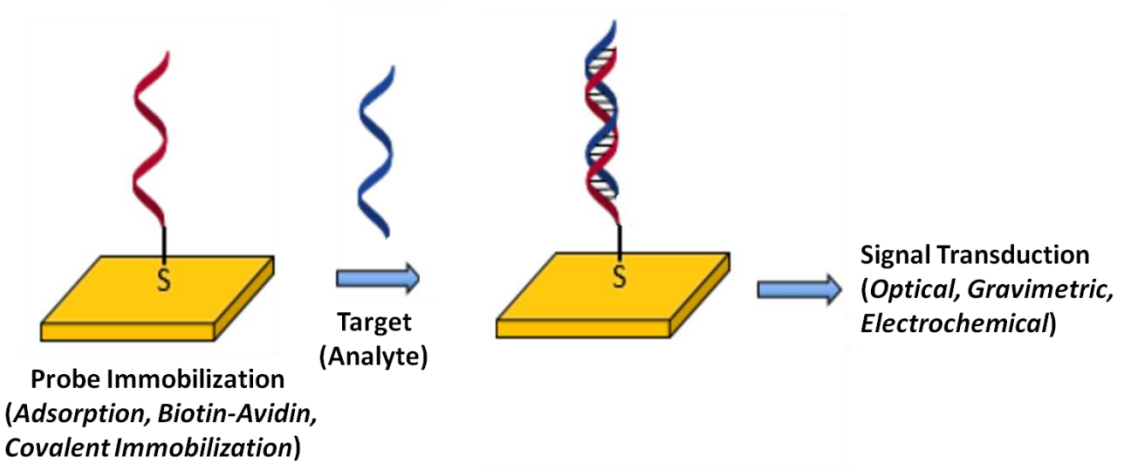

***Figure 26**. Schematic of basic DNA biosensor*

3.4.1. Probe Immobilization

The immobilization of the probe (molecular recognition) layer is essential to the development of a DNA biosensor. For a successful sensor, the probe monolayer must be stable in its immobilization and minimize the amount of non-specifically bound molecules.

3.4.1.1. Physisorption

The physisorption, or non-specific adsorption, of DNA probe onto a surface is considered the simplest method because no modification to the probe is needed - physisorption relies on van der Waals and/or electrostatic interactions between the electrode and the DNA. The earliest instance of DNA immobilization by physisorption was in 1969 by Paleček in which polynucleotides were adsorbed onto the surface of a hanging mercury drop electrode via hydrophobic base interactions.[57,58] The detection of DNA oligos using a hanging mercury drop electrode has been studied by Paleček's group. The concentration of pseudouridine has been detected to be as low as 10^{-8} M using cathodic stripping voltammetry on these electrodes.[59]

Physisorption has also been carried on both glassy carbon[60] and pyrolytic graphite[15] electrodes Similar to the mercury electrodes; the hydrophobicity of the bases plays a key role in the adsorption on carbon electrodes. Absorption on carbon electrodes can be enhanced using positive potential pulses.[61] The hydrophobicity of the electrode, surface roughness, and applied potential during adsorption increase the stability of the probe-surface interaction through the electrostatic attraction between the negatively

charged probe and the positively charged carbon. This technique has been used to immobilize both single-stranded probe DNA as well has double-stranded DNA.[62] Palecek also found that loosely bound native DNA molecules from the electrode during washing affected the peak heights of the experiments, suggesting a relatively weak adsorption.[63]

Charged polymers and polyelectrolytes have also been used to control the surface charge of the electrode and enhanced DNA adsorption (Figure 27). For instance, nonporous glass beads,[64] graphene,[65] and gold[6] electrodes can be modified with a thin film of chitosan, a natural polysaccharide. The Chitosan forms an anime ($-NH_2$) layer that is positively charged at neutral pH. The negatively charged DNA backbone is then electrostatically adsorbed onto the chitosan-modified graphene or gold surface. Other positively charged films, such as poly(allylamine)-hydrochloride (PAAH)[66] and octadecylamine,[67] have also been reported to adsorb probe through electrostatic interactions.

Although physisorption provides a simple means of immobilizing DNA on surfaces, the non-specific nature of the DNA-surface interactions cause issues with non-specific absorption and electrode fouling. Furthermore, the adsorbed DNA can interact with the electrode along its entire length resulting in poor hybridization efficiency because most of the probe is not accessible for the target to hybridize with.[68,69]

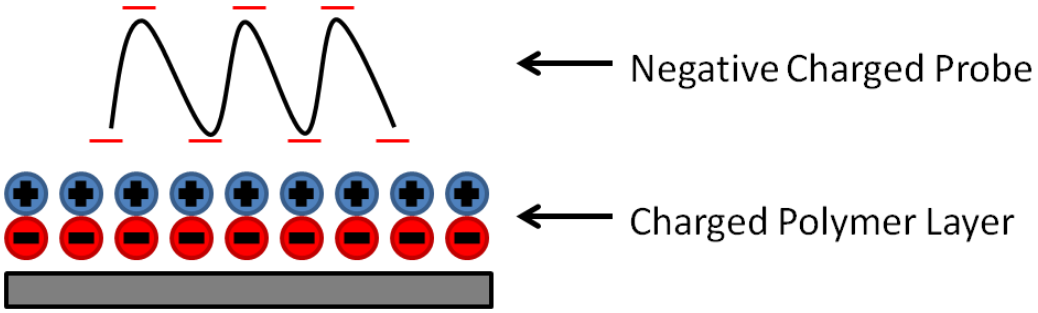

***Figure 27**. Schematic of probe immobilization via adsorption of charged polymers*

3.4.1.2. Biotin-Avidin Interaction

Biotin-avidin complexes provide a non-covalent method of probe immobilization on surfaces. Avidin is a tetrameric protein that is composed of four identical binding sites for biotin. Biotin is small molecule that has a strong binding affinity for avidin. Figure 28a depicts the general setup. For this immobilization method, first the avidin must be immobilized either covalently via thiol bonds or electrostatically adsorbed on polyelectrolytes (PAAH/PSS).[66] The probe strand can then be biotinylated to bind with the avidin. This method has been reported to be effective on gold[7] or glass[70] substrates. Streptavidin is one of the analogues of avidin, with a similar structure and function. The major structural difference is between the L3, L4 loops which is shown in Figure 28b. For avidin, it is more disordered

than the closed, ordered conformation of the streptavidin loop. This difference in the loop allows biotin-modified molecules to bind stronger to streptavidin than avidin.[71]

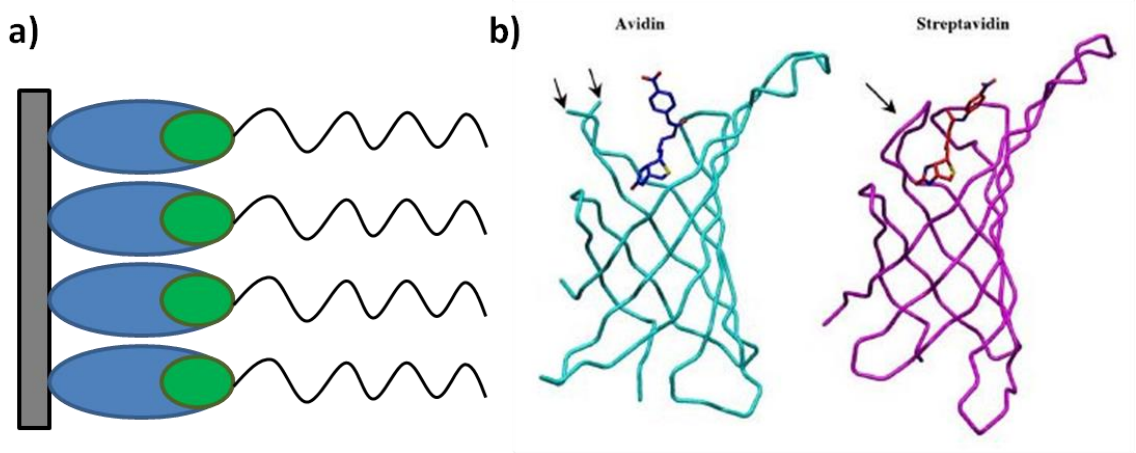

***Figure 28**. **a**) Schematic of avidin (**blue**) and biotinylated (**green**) probe immobilization on glass and **b**) crystallography to show structural differences of avidin and streptavidin*[71]

3.4.1.3. Covalent Modifications

The surface of the electrode can be functionalized to allow for covalent bonding. For example, 1-ethyl-3(3-dimethylaminopropyl)carboiimide (EDC) is an activation coupling reagent that turns a carboxylic acid (-COOH) into an intermediate that readily reacts with the amide group of DNA strands, as in Figure 29. The OH group of the carboxylic acid becomes a leaving group as EDC forms an unstable O-acylisourea intermediate. There is then a nucleophilic substitution with an amino-modified probe strand, resulting in a covalent bond between the probe and the surface (Figure 29).[72] This modification has been applied to carbon paste, [73] and carbon nanotube[74] electrodes. Polymers not only provide a charged surface for adsorption, but also a platform where covalent bonds can occur. An example is conductive polyaniline nanowires on graphene. The graphene electrode was oxidized then coated with polyaniline (PANi) nanowires through an electrochemical deposition procedure.[75] The immobilization is possible through the formation of phosphoramidate bonds between the amino group of the polyaniline and the phosphate group of the probe using EDC-coupling (Figure 30).[76] PANi nanotubes have been reported to measure the hybridization efficiencies of complementary and single mismatch DNA duplexes using differential pulse voltammetry. The duplexes with a mismatch showed a lower signal and hybridization efficiency compared to duplexes of complementary DNA. Furthermore, they reported a detection limit of 1 fM of target DNA.[77]

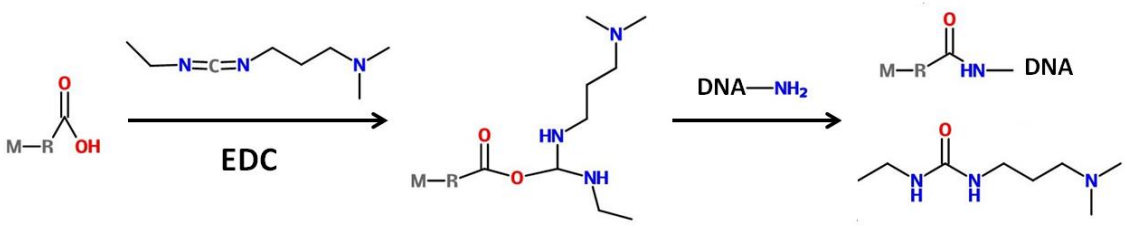

Figure 29. *EDC – coupling mechanism for probe immobilization*

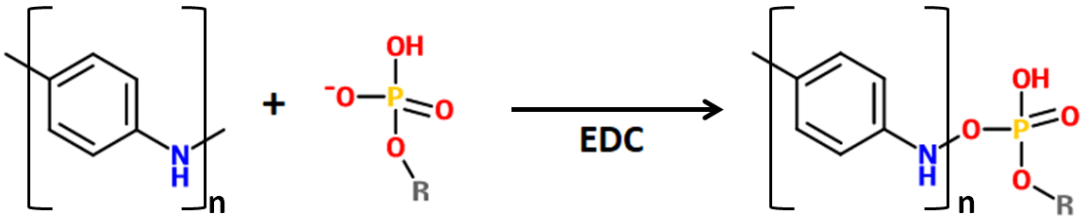

Figure 30. *Polyaniline-DNA reaction mechanism using EDC – coupling*

3.4.1.4. Covalent Immobilization via Thiol-Au Bonds

In this work, we use the method of probe immobilization via thiol-Au bonds. The probe (or molecular recognition layer) is modified with a thiol or disulfide moiety which covalently binds to the gold, forming a self-assembled monolayer on the surface. Thiol-Au monolayers have been studied for the last two decades, with the first reported

study in 1983 by the Nuzzo group.[78] Early studies have shown that thiol groups can be modified and attached to macromolecules, such as streptavidin[79] and DNA oligonucleotides.[80] Thiol modifications on the probe allow the experimenter to control the orientation of the probe on gold surfaces, a factor that physisorption does not offer.[68] This monolayer is typically followed up with a layer of an alkanethiol to pacify the gold surface and limit nonspecifically bound probe.[81] Moreover, there are multiple forms of surface-active thiols, such as those in Figure 31. Alkanethiols can assemble uniform monolayers on the surfaces of metals. However, surface impurities or defects, like those in Figure 32, affects the uniformity and bonding of the monolayer.[82] Using a thermal desorption study, Nuzzo's group also found the strength of the thiol-Au bond to be approximately 45 kcal/mol.[83] The general reaction scheme of this bond can be seen in Rxn. 3.[84]

$$R - S - H + Au_n^0 \rightarrow R - S^- Au^+ \cdot Au_n^0 + {}^1/_2\, H_2 \qquad \text{(Rxn.3)}$$

An applied potential has been shown to disrupt the monolayers due to the reduction and oxidation of the thiol bonds. Porter et al. conducted a study on reductive and oxidative desorption. The reaction schemes of the reductive (Rxn. 4) and oxidative (Rxn. 5 and 6) desorption of thiol are shown in the following;

$$RS - Au_n^0 + e^- \rightarrow RS^- + Au_n^0 \quad \text{(Rxn.4)}$$

$$RS - Au_n^0 + 2H_2O \rightarrow Au_n^0 + RSO_2H + 3e^- + 3H^+ \quad \text{(Rxn.5)}$$

$$RS - Au_n^0 + 2H_2O \rightarrow Au_n^0 + RSO_2^- + 3e^- + 4H^+ \quad \text{(Rxn.6)}$$

The reductive and oxidation desorption of n-alkanethiol on Au increases negatively as the number of carbon increases and the pH decreases. In a solution of 0.5 M KCl at pH 7, the reductive and oxidative desorption potentials were -0.95 and -1.2 V vs. Ag/AgCl for a 6-carbon thiol; similar to the thiol in this work.[85] A disadvantage to thiol-gold immobilization is that thermal stability above 75 ^{0}C is limited.[38]

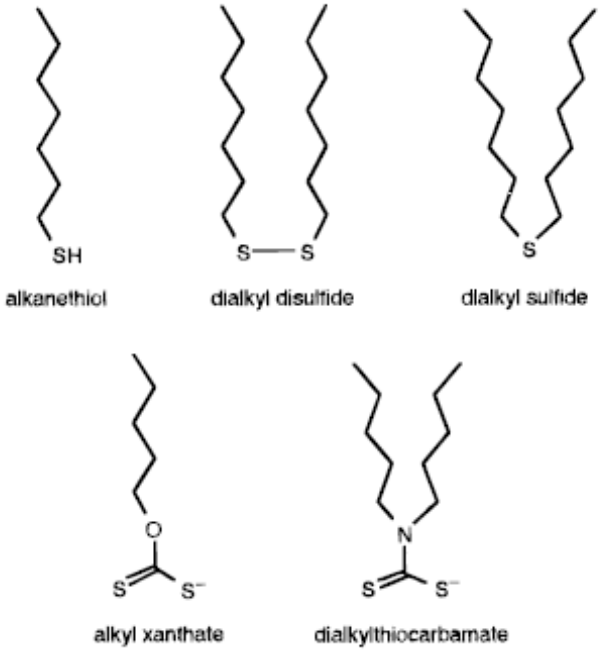

Figure 31. *Surface-active organosulfur compounds from Ulman et al.* [84]

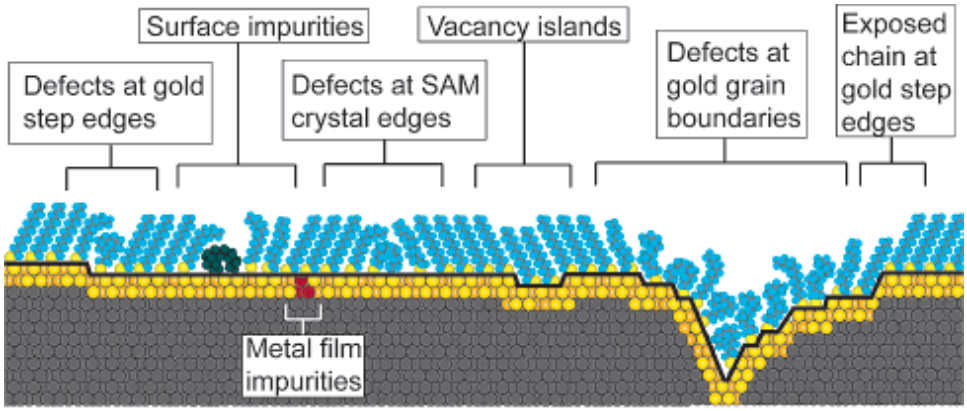

Figure 32. *Schematic illustration of some intrinsic and extrinsic defects in monolayers of thiols on gold.*[82]

3.5. Transduction Methods for Hybridization Detection

Ultimately, the method of probe immobilization depends on the electrode material being used, which in turn depends on the detection modality employed. As is often the case, there is a trade-off between stability, ease-of-modification, and reproducibility. In the end, the best immobilization strategy will be the one that gives consistent results for the chosen transduction mechanism. Here, various transduction techniques are outlined. These methods include optical, gravimetric, and electrochemical techniques. These techniques can be used to obtain a measurable signal which can determine immobilization of probe, hybridization of target, or binding of proteins/small molecules.

3.5.1. Optical – Fluorescence

For fluorescence-based detection, typically the target strand is labeled with a fluorophore. Upon hybridization to the surface-bound probe, the fluorescence is detected. For example, Mehnaaz et al used fluorophores to detect DNA hybridization and mismatch discrimination on a microbead array. Biotinylated probe DNA was immobilized on a microbead array using avidin. Target strands were tagged with fluorescein isothiocyanate, Texas Red, or Pacific Blue. Once hybridized, the signal from fully the complementary strands gave a higher fluorescent signal than non-complementary.[86]

Molecular beacons have been reported to detect DNA hybridization. Molecular beacons are sequences that contain a hairpin (Figure 33) with a fluorophore and fluorescence quencher on opposite ends of the sequence. In the hairpin conformation, the fluorescence of the fluorophore is quenched. However, once the strand hybridizes with target DNA, the hairpin breaks apart and a rigid duplex forms. This increases the distance between the fluorophore and quencher, which increases the fluorescence of the sensor.[87,88] This setup allows for label-free sensing of DNA hybridization and mismatch discrimination.[89] Reports have shown that gold surfaces have the ability to quench the fluorescence of fluorophores such as rhodamine red or Cy-5. In both case, the molecular beacon is either covalently bound to a gold surface via a thiol bond[90] or in solution with negatively charged gold nanoparticles.[91] The fluorescence signal is quenched as the fluorophore is in close proximity of the gold. However once hybridized, the signal increases due to the distance of the fluorophore and surface increases or the gold nanoparticles no longer being attracted to the dsDNA. These studies were able to report on DNA hybridization down to a concentration of 1 10 nM.

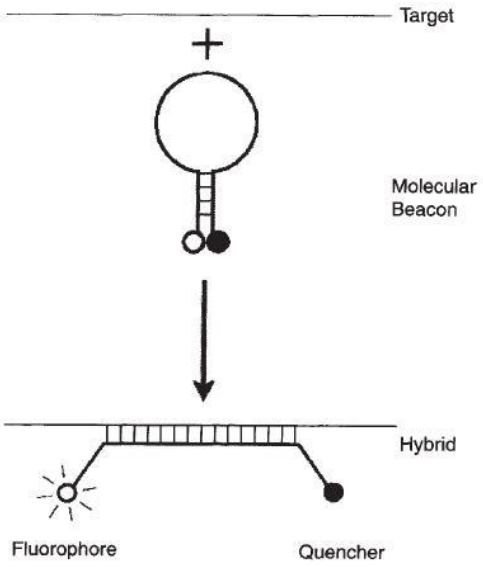

***Figure 33**. Generic setup of a molecular beacon.* [40]

3.5.2. Optical – Surface-Enhanced Raman Spectroscopy Detection

Surface-enhanced Raman spectroscopy is a sensitive surface technique. When incident light interacts with the analyte, an electric field induces a polarization of the electron cloud. This electric field is amplified by the resonant field given off when the light also hits the surface. The metal acts similarly to an antenna amplifying the electromagnetic field form the incident light source. Like fluorescence, surface-enhanced Raman spectroscopy (SERS) detection utilizes labeled target strands to detect DNA hybridization or mismatches. Raman dyes can be fluorescent or non-fluorescent. Furthermore, minor modification to a Raman-active dye molecule can lead to different Raman spectra even if they exhibit indistinguishable fluorescence spectra.[92,93] Studies by Bartlett's group utilize SERS to detect DNA hybridization, mismatch discrimination, and melting. In these studies, a mixed monolayer of probe and alkanethiols are immobilized on functionalized gold nanostructures. These gold nanostructures are optimized to enhance SERS signal. Target tagged with a SERS-active label, such as Texas Red, hybridizes with the probe; this produces a SERS signal.[94] As temperature or potential is ramped, the signal decreases due to the target melting and diffusing to the bulk of the solution.

Instead of a functionalized, structured surface, other works use a smooth surface in conjunction with nanoparticles for the SERS detection of DNA. A monolayer of probe, alkanethiols, and 5-((2-(and-3)-S-(acetylmercapto)succinoyl)amino) (SAMSA) fluorescein is immobilized on a smooth gold surface, while the target is tagged with a silver nanoparticle. When hit with incident light, the gold surface and silver nanoparticle creates an intense electromagnetic hotspot which strongly enhances the SERS signal.[95] This technique is also reported to work with DNA "sandwich" structure (Figure 34) on gold nanowires.[96]

SERS allow for detection limits of 1 μM to 10 pM.[94] A drawback of SERS detection is that is relies on the fabrication of specialized nanostructured surfaces to obtain its low detection limits.

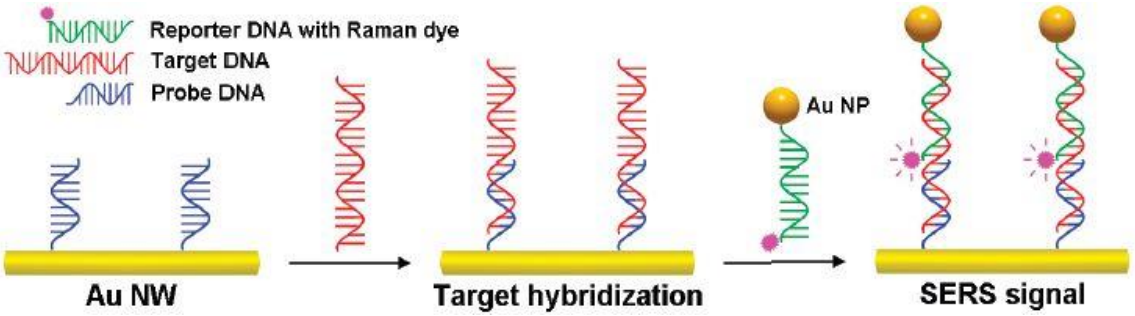

***Figure 34**. Example of a DNA sandwich assay on gold nanowires tagged with a Raman dye and a gold nanoparticle*[96]

3.5.3. Optical – Surface Plasmon Resonance

Surface Plasmon Resonance (SPR), like SERS, is an optical technique relying on the interactions between light and the electrons on metal surfaces. As shown in Figure 35, a laser shines on a metal surface through a prism. The laser is refracted off the surface and the refractive index is calculated with the detector. Any changes to the refractive index are due to changes on the surface of the substrate. SPR allows for real-time monitoring of DNA hybridization/melting as the refractive index changes. SPR has been reported to detect DNA hybridization.[98] The biotinylated probe is immobilized on a surface of avidin on gold. As the target molecule hybridizes, the refractive index increases until it reaches a point of saturation. It is at this point where the probe is fully hybridized with the target. This technique works well with label-free hybridization monitoring – no fluorescence or SERS label is necessary. However, if low-molecular weight molecules, such as short-chain DNA, are involved in the binding or if the packing density of the film is very low, the resonance angle shifts are very slight and SPR is no longer sensitive enough to monitor these binding events or interactions. Non-specific absorption, i.e. not via hybridization, also results in false positives. SPR detection discriminates between mismatches. On a gold substrate with a mixed monolayer of probe and alkanethiols, Heaton et al. studied the effects of low negative and positive potentials on the hybridization and melting of DNA duplexes. Based on the SPR data, hybridization rates were calculated and plotted as a function of time. They found that an applied positive potential facilitates hybridization for mismatch DNA and a negative potential lowers both complementary and mismatch duplex; however, the rate of the mismatch duplex is lower.[99,100] The limit of detection for SPR biosensing of DNA hybridization is 2 nM for 37-bp DNA.[101] However, SPR is not sensitive enough for short-chain DNA molecules or low molecular weight molecules because the resonance angle shift is very slight.[102]

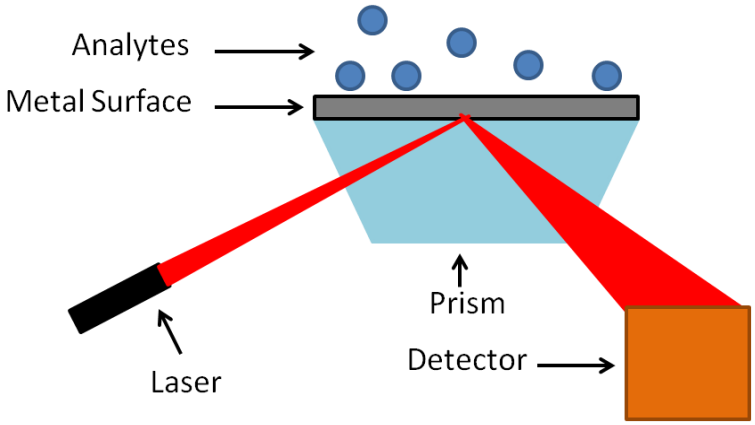

***Figure 35**. The basic set up of a surface plasmon resonance (SPR) experiment.*

3.5.4. Gravimetric – Quartz Crystal Microbalance

A quartz crystal microbalance is a mass-sensitive sensor that can detect changes in mass on the nanogram scale. It consists of a quartz disc between two electrodes. The crystal vibrates at a specific resonance frequency that is dependent on the mass deposited on the electrode. When the mass of the crystal changes, the resonance frequency changes according to the Sauerbrey equation:

$$\Delta f = \frac{-2.3 * 10^{-6} f^2 \Delta m}{A} \quad \text{(Eq.17)}$$

where Δf is the change in frequency, f is the fundamental frequency of the quartz, A is the surface area, Δm is the deposited mass.[103] QCM provides the opportunity to characterize the immobilization of probe on the surface and the hybridization of target by observing the change in frequency of the QCM and calculating the mass change. QCM-based methods have also been reported to detect mismatches. For instance, peptide nucleic acids (PNA) probes were immobilized on QCM electrodes, then subjected to a solution of complementary target and mismatch DNA. The frequency of the crystal changed when hybridized with a complimentary strand, while the mismatch had no effect.[104] QCM offers an effective, label-free method to monitor DNA hybridization and mismatches. This sensitive technique allows for a detection limit of 5 x 10^{-12} M.[85] However, in aqueous solutions, the use of QCM is can be challenging and unreliable.[105,106]

3.5.5. Gravimetric – Microcantilever

The working principle of microcantilevers relies on surface stress induced by mass loading. Figure 36 show a cantilever as a DNA biosensor. The cantilever deflection signal (Δz), is given by

$$\Delta z \cong \frac{3(1-v)L^2}{Et^2}(\Delta\sigma_1 - \Delta\sigma_2) \quad \text{(Eq.18)}$$

where $\boldsymbol{E}$ is the Young's modulus, $\boldsymbol{v}$ is Poisson ratio, $\boldsymbol{t}$ and $\boldsymbol{L}$ are thickness and length of the beam and $\boldsymbol{\Delta\sigma_1 - \Delta\sigma_2}$ accounts for the differential surface stress.[107] For a given experiment, a baseline of the deflection signal is taken. Once established, changes to the deflective signal are monitored over time, which represents changes in the mass on the cantilever. The use of gold-plated cantilevers was first introduced by Fritz et al. The cantilevers are coated with a thin layer of gold and then immobilized with probe DNA. A baseline of the deflection signal is measured over time. When introduced to complementary target, the stress from the mass loading causes a shift in the deflection signal. The shift in signal represents successful hybridization of DNA. The detection limit of the microcantilever was 10 nM of 12 base pairs oligos.[108] Further studies show that the use of cantilever detection is sensitive enough to differentiate between mismatches and target length. Microcantilevers, like QCM, offer a label-free detection method for DNA hybridization and mismatch detection.[109] The main disadvantage of microcantilever devices are the high costs and technical skills needed to fabricate them.[105]

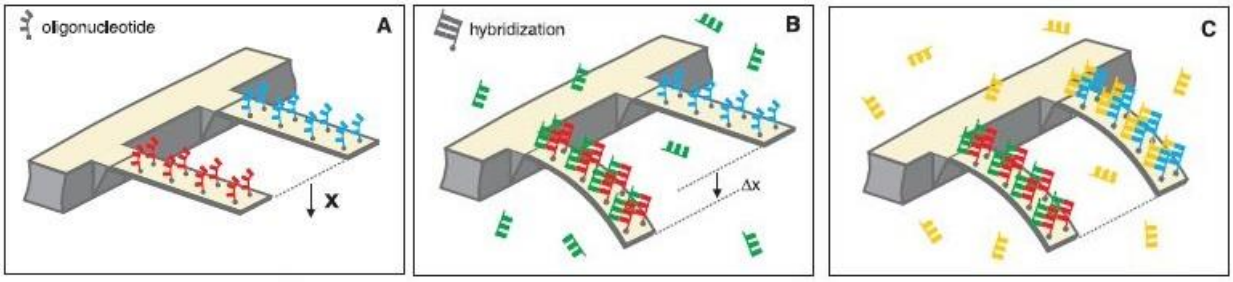

***Figure 36**. Scheme of oligo-functionalized cantilevers for hybridization detection.*[108]

3.5.6. Electrochemical – Charge Transport

The π-stacking of the nitrogenous bases suggests that DNA has special electrical properties and can act as a charge mediator analogous to a molecular wire due to its high conductivity and electronic coupling of donor and acceptors.[110] Two theories that arose to the mechanism behind charge transport are super exchange and charge hopping. In the super exchange mechanism, the charge tunnels though high energy bases without formally occupying them; however, the rate decreases exponentially with distance between the charge donor and acceptor.[111] This model does not satisfy DNA-mediated charge transfer over long distances. In the hopping mechanism, charge occupies the low energy sites of the base pairs, hopping one to the next.[111-113] This model does not take into account the dynamic structure of DNA since DNA strands are not rigid "bridges." The Barton group has proposed a domain-hopping mechanism where charge passes through the DNA using delocalized domains.[111,114] A domain is a sequence-dependent feature of DNA that exists in the absence of a charge. This transient nature of DNA, coupled with the π-stacking of DNA allows charge to hop into these empty, delocalized domains along the DNA

bridge. The electrical properties and charge transport of DNA allow for the electrochemical transduction of some DNA Biosensors.

3.5.7. Electrochemical – Electroactivity of Nitrogenous Bases

The purine bases, guanine and adenine are electrochemically reduced at extremely low potentials and readily adsorb onto mercury, gold, copper, and carbon.[115] Paleček first demonstrated the electrochemical oxidation of DNA adsorbed on mercury electrodes using oscillographic.[57,63,116] Polynucleotides were absorbed onto the surface at a potential of -0.1 V. By running adsorption stripping voltammetry, they found that DNA denatured at -1.5 V, allowing them to differentiate between ssDNA and dsDNA. The electrode current was measured as a function of time and a function of potential as the analyte is stripped. Further studies by Wang et al. have improved this methodology, resulting in a detection limit of 40 femtomoles.[117] Utilization of electrochemical techniques, such as differential pulse voltammetry, can distinguish between single stranded and double stranded. Kerman et. al reported that the oxidation signal of guanine on carbon electrodes decreases as the duplex form, because the guanine bases are no longer accessible. They also saw that this signal decreases as the concentration of the target strand increases.[118]

Another electrochemical method utilizes mediators to indirectly oxidize target DNA through an electrocatalytic reaction. A well-known system is adopted from Thorp where a redox molecule, like $Ru(bpy)_3^{2+}$ (ruthenium 2,2'-bipyridine), oxidizes guanine in an electrocatalytic cycle. The electrode first oxidizes $Ru(bpy)_3^{2+}$ to $Ru(bpy)_3^{3+}$, which then removes an electron from guanine to form a radical cation which in turn, deprotonates and undergoes the cycle again (Rxn. 7 and 8).[119] The signal from this technique can differentiate between ssDNA and dsDNA where ssDNA has a higher signal because ssDNA has more accessible guanine bases than dsDNA.

$$\boldsymbol{Ru(bpy)_3^{2+} \rightarrow Ru(bpy)_3^{3+} + e^-} \qquad \text{(Rxn.7)}$$

$$\boldsymbol{Ru(bpy)_3^{3+} + guanine \rightarrow Ru(bpy)_3^{2+} + guanine^+} \qquad \text{(Rxn.8)}$$

3.5.8. Electrochemical – Enzyme-Labeled

This scheme consists of a surface-bound probe strand hybridizing with an enzyme-tagged target strand. The redox-active enzyme typically undergoes an electrocatalytic reaction with the DNA and surface which amplifies the measured signal. Horseradish peroxidase (HRP) is used to study the signal amplification from enzymes. A redox polymer, poly(4-vinylpyridine)-coacrylamide-$Os(bpy)_2Cl_2$, is drop-casted or electrodeposited on an electrode. A capture probe is covalently bound to the surface. The hybridization of target is followed up with the enzyme-tagged detection probe to form a DNA duplex (from three strands) with the distal end tagged with HRP. The electrocatalytic reaction is as follows: the

electrode oxidizes $Os(bpy)_2^{3+}$ to $Os(bpy)_2^{2+}$ which reduces HRP. The result is a reduction of hydrogen peroxide to water. The resulting amperometric current increases with the concentration of hydrogen peroxide. Further studies found that mismatches in the sequence disrupt the electrocatalytic reaction of the enzyme.[120-122]

Glucose oxidase amplifies the amperometric signal. In a similar sandwich-type assay, a capture probe is immobilized gold then hybridized with target and the glucose oxidase-tagged detection probe. The electrode is then incubated in a redox solution of poly(4-vinylpyridine)-coacrylamide-$Os(bpy)_2Cl_2$ (PVA-Os). The result is an increase in oxidation current due to the electrocatalytic reaction with glucose when glucose oxidase is activated by the $Os(bpy)_2^{2+}$ coating. This increase in current is proportional to the concentration of glucose in the solution and decreases if mismatches are present.[123]

3.5.9. Electrochemical – Redox Indicators

Using a redox molecule yields an electrochemical signal which decreases or increases based on DNA hybridization. This method is similar to fluorescent dyes for optical signals; however, redox molecules offer more versatility for measurements. The performance of surface-bound DNA sensors is affected by the following properties of redox molecules: formal potential, affinity for DNA, selectively of dsDNA versus ssDNA, and nonspecific binding to the electrode surface. The formal potential of redox molecule should be within a range that does not affect the DNA duplex, i.e. cause dehybridization or desorption from the electrode. The redox molecule should bind to DNA, specifically to dsDNA, to detect hybridization. Figure 37 depicts the three types of redox-active molecules for electrochemical measurements. The redox molecule should also demonstrate low nonspecific binding to the surface to reduce background current/noise.[38]

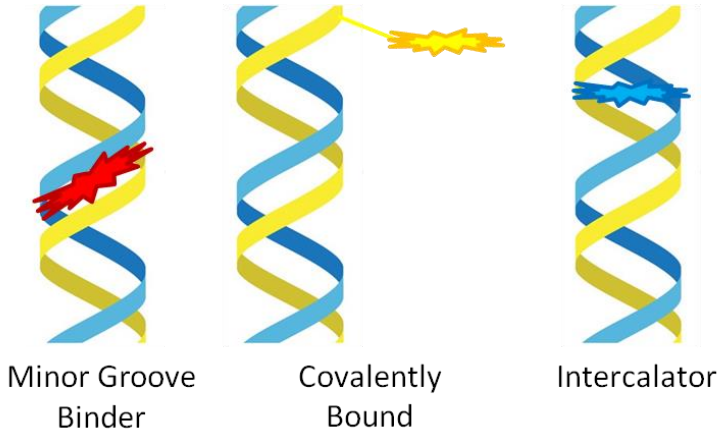

Figure 37*. Three variations of using redox-active molecules in electrochemical transduction.*

3.5.9.1. Groove Binding Redox Molecules

Having been the first to report on surface-bound, electrochemical detection of DNA, Hashimoto et al., used the electroactive molecule Hoechets 3258 to monitor DNA hybridization. Fully hybridized DNA was immobilized on gold electrodes via Au-thiol bonds. The electrode was then incubated in Hoechets 3258, which binds to the minor grooves of dsDNA, as shown in Figure 37. Linear sweep voltammetry was then used to show that the redox signal was much higher in dsDNA than ssDNA because more of the redox molecule was bound to the DNA.[68] In section 4.5.6., $Ru(bpy)_3^{2+}$ is used as a minor groove binder to facilitate the electrochemical detection of guanine. In a more recent study, a bis-acetylferrocene ethylenediamine complex ($(AFc)_2$-en) is used as a groove binder as it is less toxic than Hoechets 3258. As a groove binder, it was used as a novel method for DNA hybridization detection. It has a binding strength of 3.5×10^5 $Lmol^{-1}$ and a detection limit of 2.0×10^{-15} M. Although effective, groove binders can be toxic, such as Hoechets 3258, and have a weak binding strength compared to other methods.[124]

3.5.9.2. Covalently-Bound Indicators

Methylene blue and ferrocene are common covalently-bound redox indicators used in DNA biosensors. Ferrocene is a stable organometallic compound which exhibits a fast, electrochemically reversible redox reaction. The ferrocene molecule is typically covalently bound to the DNA strands through an aminohexyl-linker. The reaction scheme for this linker is described in detail by Ihara et al.[125] Other methods of synthesizing and purifying ferrocene-tagged DNA have also been reported.[125-127] Nakayama et al, utilized ferrocenyl, a derivative of ferrocene, and a sandwich-type assay, such as the one in Figure 34, to monitor DNA hybridization and mismatch discrimination. A capture probe strand is immobilized onto a gold surface. The ferrocenyl-tagged detection probe is hybridized with the target, then the complex is hybridized with the immobilized capture probe. Differential pulse voltammetry is then used to measure the amount of ferrocenyl units, which equates to the number of hybridized duplexes on the surface. The results show that a redox signal was present for fully complementary target but there was no signal for non-complementary target.[128] Ferrocene is used a model similar to the molecular beacon in fluorescence measurements, allowing for label-free detection. The probe is immobilized on gold and can adopt two different conformations, a hairpin (without target DNA) and the hybridized duplex (with target DNA). A ferrocene molecule is tagged on the distal end of the probe. In its hairpin form, the ferrocene is near with the electrode surface; therefore, there is a strong voltammetric signal. After incubation in target solution, the probe hairpin hybridizes with the target causing the ferrocene to be further away from the electrode and lowering the redox signal.[129]

3.5.9.3. Intercalators

Methylene blue (MB) is recognized as a molecule to detect DNA hybridization and discriminate mismatches in a similar fashion to ferrocene. MB can intercalate from solution or be utilized as a covalent modification, as mentioned above. A study on methylene blue and its affect as an intercalator was reported by Kerman.[130,131] A mixed monolayer of probe DNA and alkanethiol is formed on the surface of a gold electrode. The electrode is in hybridized with target DNA forming the duplex. Once formed, it is incubated in a solution of methylene blue. This allows the MB to intercalate in between the base pairs. Differential pulse voltammetry was used to measure the immobilized probe before and after hybridization. They found that once hybridized, the MB signal decreases. Further studies found that MB has a strong affinity towards guanine and by forming the duplex, the guanine are less accessible.[131] Barton et al. reported a new method for DNA detection using methylene blue and ferricyanide. A gold electrode was modified with a monolayer of thiolated dsDNA. The duplexes were then incubated in MB. Electrochemical measurements were done in a solution of ferricyanide. A negative potential reduces the MB to leucomethylene blue, which readily reduces ferricyanide to ferricyanide. This electrocatalytic cycle then regenerates the MB.[132] Later studies have shown that mismatches disrupt the electrocatalytic cycle, diminishing the redox signal.[133] Although both are well studied, methylene blue has some advantages over ferrocene. The oxidized form of ferrocene is extremely prone to nucleophilic attacks and its electrochemical signal decreases over time.[126]

Chapter 4: Electrochemical melting of surface-bound DNA

4.1. Introduction

Development of DNA sensors based on electrochemical or optical measurements on gold electrodes is an area of active research with promising applications in point-of-care detection of biomarkers for medical diagnostics and forensics. These sensors utilize electrochemical techniques,[134-138] spectroscopic detection (particularly SPR and SERS),[139-142] DNA-mediated charge-transport,[105,143] and gravimetric measurements.[144] In many of these sensors the gold substrate is first modified with a mixed monolayer of probe DNA and an alkyl thiol. Subsequent hybridization of the target DNA results in a measurable signal via one of the transduction mechanisms mentioned above. In this work, we present a method for the monitoring and melting surface-bound DNA using a purely electrochemical approach at room temperature. This method relies on the application of a sufficiently negative potential to the modified gold electrode, resulting in destabilization of the surface-bound DNA, dehybrization, and subsequent diffusion of the DNA into the bulk of the solution. This method is distinct from temperature-based melting of surface-bound DNA, which uses increased temperatures to melt surface bound DNA.[145,146] The extent of hybridization is monitored by square wave voltammetry of methylene blue attached to the proximate end of the target strand.

While surface-based electrochemical approaches have great potential, much work is still required to fully understand the underlying electrochemistry and bioelectrochemistry of these systems and the behavior of DNA in the high electric fields generated at these interfaces. The effect of electric fields on surface-bound DNA is well studied. Relatively small electric fields have been shown to orient single-stranded DNA on surfaces. Negative potentials orient DNA in an upright position, due to electrostatic repulsion. In the presence of free target strands in solution, positive potentials can provide enhancement of hybridization, by decreasing the electrostatic penalty of the approaching negatively charged phosphate backbones.[147-151] Theories to explain this enhancement include Pettitt's thermodynamic theory for the effect of electric field on the stability of surface-bound DNA duplexes. Hybridization in the presence of a positive potential results in both greater hybridization efficiency and enhanced hybridization kinetics. These results suggest electrostatic effects play a key role in the hybridization and orientation of surface-bound DNA, offering routes to control DNA assembly utilizing the applied potential.

The destabilizing effect of negative applied potentials has also been explored.[147-149] In these reports, negative potentials are found to inhibit hybridization and to initiate melting of previously hybridized surface-bound DNA. Bartlett et al, have applied this concept towards development of an electrochemical melting procedure on nanostructured gold electrodes utilizing SERS to detect the extent of hybridization.[95] Most of these "e-melting" studies rely on spectroscopy techniques to monitor the

extent of melting, focusing on melting at constant potentials, in the presence of free target in solution.[148,149] These experiments firmly establish the ability of an electric field to melt surface-bound DNA. Bartlett's work introduces the concept of melting potential, analogous to melting temperature, as an indicator of duplex stability and characterizing surface-bound DNA. Additionally, Bartlett et al. have utilized peptide nucleic acids (PNA), which are charge neutral, in lieu of DNA in e-melting experiments.[152] Signal change due to DNA dehybridization still occurred suggesting that the mechanism behind e-melting is not purely due to the electrostatic repulsion of the phosphate backbone and the electrode surface. More recently, infrared reflection absorption spectroscopy of surface-bound DNA duplexes in situ suggests that the base pairs become strained under the application of negative potentials by destabilizing the hydrogen bonds.[153] There is no evidence that the local temperature of the surface is increased, due to joule heating or other mechanism, as has been reported in other cases.

Here we present an in-depth study of e-melting using a simple electrochemical approach. Our approach is carried out in low ionic strength buffers and moderate probe densities, minimizing counterion screening without introducing steric hindrances to hybridization. We carefully examine potential-dependence of the melting kinetics and the melting efficiency. In addition to introducing a facile methodology for DNA analysis and biophysical studies, these results shed some light on the mechanism of e-melting and the interplay of double-layer charging and duplex stability.

4.2. Experimental Method

4.2.1. Preparations of Materials

The 34- and 18-base pair complimentary probe, 2-mismatch probe, 1-mismatch probe, and target DNA strands, sequences shown in Table 3, were purified by dual HPLC (LGC Biosearch Technologies, Petaluma, CA). The probe oligos were labeled with a thiol group through a 6-carbon linker on the 5' end and was delivered in the form of a disulfide. The strands (either probe or target) were tagged with methylene blue are labeled with an amine group. The methylene blue was covalently attached according to procedures by LGC Biosearch Technologies. The amine-modified oligos were diluted and sorted in 0.1 M sodium carbonate buffer (pH 9). Methylene blue, modified with an NHS ester (LGC Biosearch Technologies, Petaluma, CA), was diluted and stored in DMSO (Aldrich, Wyoming, IL). The MB solution was added to the oligo in a ratio of 10:1 to react. The reaction was run for 24 hours, in the dark, at room temperature. After the reaction, the solution was desalted and purified using four 25 g Sephedex columns (GE Healthcare Life Sciences, Pittsburgh, PA) placed in series on an FPLC (GE AKTApure (25L) serial number: 29018224).

***Table 3**. DNA Sequences*

Name	Sequence
34-bp Fully Complementary duplex	Probe: 5′HS-C6-TGG ATC GGC GTT TTA TTC TTG TTC AGA TAT TCA A 3′ Target: 3′ (MB)-ACC TAG CCG CAA AAT AAG AAC AAG TCT ATA AGT T 5′
*34-bp Single **Mismatch** duplex*	Probe: 5′HS-C6-TGG ATC GGC GTT CTA TTC TTG TTC AGA TAT TCA A 3′ Target: 3′ (MB)-ACC TAG CCG CAA AAT AAG AAC AAG TCT ATA AGT T 5′
*34-bp Double **Mismatch** duplex*	Probe: 5′HS-C6-TGG ATC GGC GTT CCA TTC TTG TTC AGA TAT TCA A 3′ Target: 3′ (MB)-ACC TAG CCG CAA AAT AAG AAC AAG TCT ATA AGT T 5′
*18-bp Duplex (**MB** on target)*	Probe: 5′HS-C6-TTG ATC GGC GTT TTA TTC 3′ Target: 3′ (MB)-AAC TAG CCG CAA AAT AAG 5′
*18-bp Duplex (**MB** on probe)*	Probe: 5′HS-C6-TT(MB)G ATC GGC GTT TTA TTC 3′ Target: 3′ AA----C TAG CCG CAA AAT AAG 5′
*34-bp Probe **Hairpin***	Probe: 5′HS-C6-TGG ATC GGC GTT TTA TTC TTG TTC AGA TAT TCA A 3′
*34-bp Target **Hairpin***	Target: 3′ (MB)-ACC TAG CCG CAA AAT AAG AAC AAG TCT ATA AGT T 5′

Sulfuric acid (Pharmco-Aaper, 95-98 wt%, ACS grade), hydrogen peroxide (BDH/VWR Analytical, 30 wt% in H_2O), hydrochloric acid (Pharmco-Aaper, 36.5-38 wt%, ACS grade), potassium ferricyanide (III) (Sigma-Aldrich, >99 wt%), tris(2-carboxyethyl)phosphine-HCl (Sigma-Aldrich, >98 wt%, TCEP), hexamine ruthenium (III) chloride (Alfa Aesar, 32.1 wt%, RuHex), 1-mercaptohexanol (Sigma-Aldrich, 97 wt%, MCH), Phosphate Buffered Saline tablets (Sigma-Aldrich, >98 wt%, PBS), Tris base (JT Baker, 99.9 wt%), NaCl(Sigma Aldrich, ≥99 wt%), KCl(EM Science, 99 wt%), $MgCl_2$ (Johnson Matthey Electronics, 97.5 wt%), and EDTA (Sigma, ≥99 wt%) were used as received. Solutions were made using 18 MΩ nanopure water.

Four buffers were prepared and used as follows: (1) Probe incubation was performed using a PBS solution (10 mM phosphate buffer, 1.0127 M NaCl and 3.7 mM MgCl2 at pH 7.4), (2) Electrodes were rinsed in 5 mM Tris with 10 mM NaCl at pH 7, (3) DNA hybridization was performed in 10 mM Tris with 1.0 M NaCl and 1 mM EDTA at pH 7, and (4) Electrochemical measurements were performed in 10 mM Tris buffer at pH 7.

4.2.2. Preparation of Gold Electrodes

A schematic of our DNA electrodes is shown in Figure 38. To start, polycrystalline gold disk electrodes (2 mm diameter, CH Instruments, Austin, TX) were mechanically polished using 1 and 0.05 μm alumina slurry followed by sonication for 10 min in ethanol and DI water, sequentially. The electrodes were submerged in piranha solution (3:1 sulfuric acid to 30% hydrogen peroxide) for 30 s to remove residual organic matter. After thorough rinsing in DI water, the electrodes were electrochemically polished in 0.5 M H_2SO_4. The process consisted of (a) pulsing the potential at 1.6 V for 5 s, then stepping to -1 V for another 5 s for a total of 20 cycles, (b) cycling the potential from -0.2 to 1.6 V for 50 cycles at

10 V/s, (c) and cycling the potential from -0.2 to 1.6 V for 10 cycles at 50 mV/s. After cleaning, the electrodes were then cycled in 2.5 mM $K_4Fe(CN)_6/K_3Fe(CN)_6$ in 1 M KCl. The final CVs in H_2SO_4 and $K_4Fe(CN)_6/K_3Fe(CN)_6$ were used to verify the cleanliness of the surface.

4.2.3. Preparation of DNA-Modified Electrode

After reduction of the target disulfide bond with TCEP, the probe solution was diluted to a final concentration of 10 µM using PBS buffer. The polished electrodes were incubated in this solution for 20-24 hrs in the dark at 4 ºC. Afterward, the electrodes were backfilled with 10 mM MCH in PBS buffer for 1 hr to prevent non-specific absorption of DNA. At this stage, the surface density of probe was determined using the RuHex assay as first reported by Steel et al.[9] The average probe densities were found to be 8×10^{12} molecules/cm^2 $\pm$ 2×10^{12} molecules/cm^2. These values agree with previously recorded values under similar conditions. The electrodes were then incubated in a solution of 5 µM target DNA, in the dark, for 2 hours at either room temperature (~25 ºC) or 55 ºC. Room temperature hybridization was only used for the experiments requiring the hairpin on the 34-bp oligonucleotide.

4.2.4. Electrochemical Instrumentation and Parameters

Electrochemical measurements were carried out using a VersaStat 4 potentiostat with VersaStudio software (Ametek Scientific Instruments, Berwyn, PA) or a WaveNow potentiostat with AfterMath software (Pine Research, Durham, NC). A typical three-electrode cell was used, which consisted of a DNA-modified gold working electrode, a platinum wire auxiliary electrode (CH Instruments, Part# CHI102), and an Ag/AgCl/1M KCl(aq) reference electrode (CH Instruments, Part# CHI111). All electrochemical measurements, including the melting routines described below, were carried out at room temperature.

The electrochemical melting routines consisted of a programmed sequence of potential pulses, between which SWV are acquired to monitor the amount of MB-tagged DNA on the electrode surface after each potential pulse. The pulse potentials were either incrementally decreased (Figure 39ab) or kept constant (Figure 39cd). After each pulse, but before the SWV, the electrode was equilibrated at -0.1 V for 10 s. The equilibration step was found to provide better quality voltammograms. The SWV parameters were as follows: initial potential -0.1 V, final potential -0.45 V, amplitude 25 mV, period 6 ms, and pulse width 10 milliseconds. The baseline subtracted SWV peak currents were plotted versus time or pulse potential. All measurements were carried out in a solution of 10 mM tris.

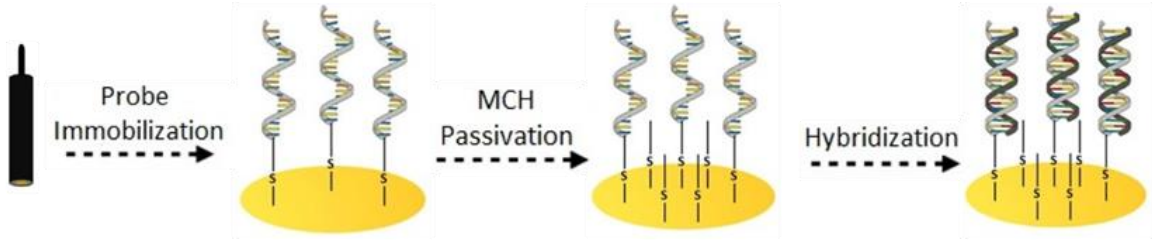

Figure 38. *Schematic of our DNA-modified electrode procedure. (1) We employ a three-step cleaning/polishing method to prepare our gold surface. (2) A mixture of thiolated probe DNA and mercaptohexanol (MCH) is immobilized on the surface. (3) The electrode is then incubated with a methylene blue (MB)-tagged target DNA.*

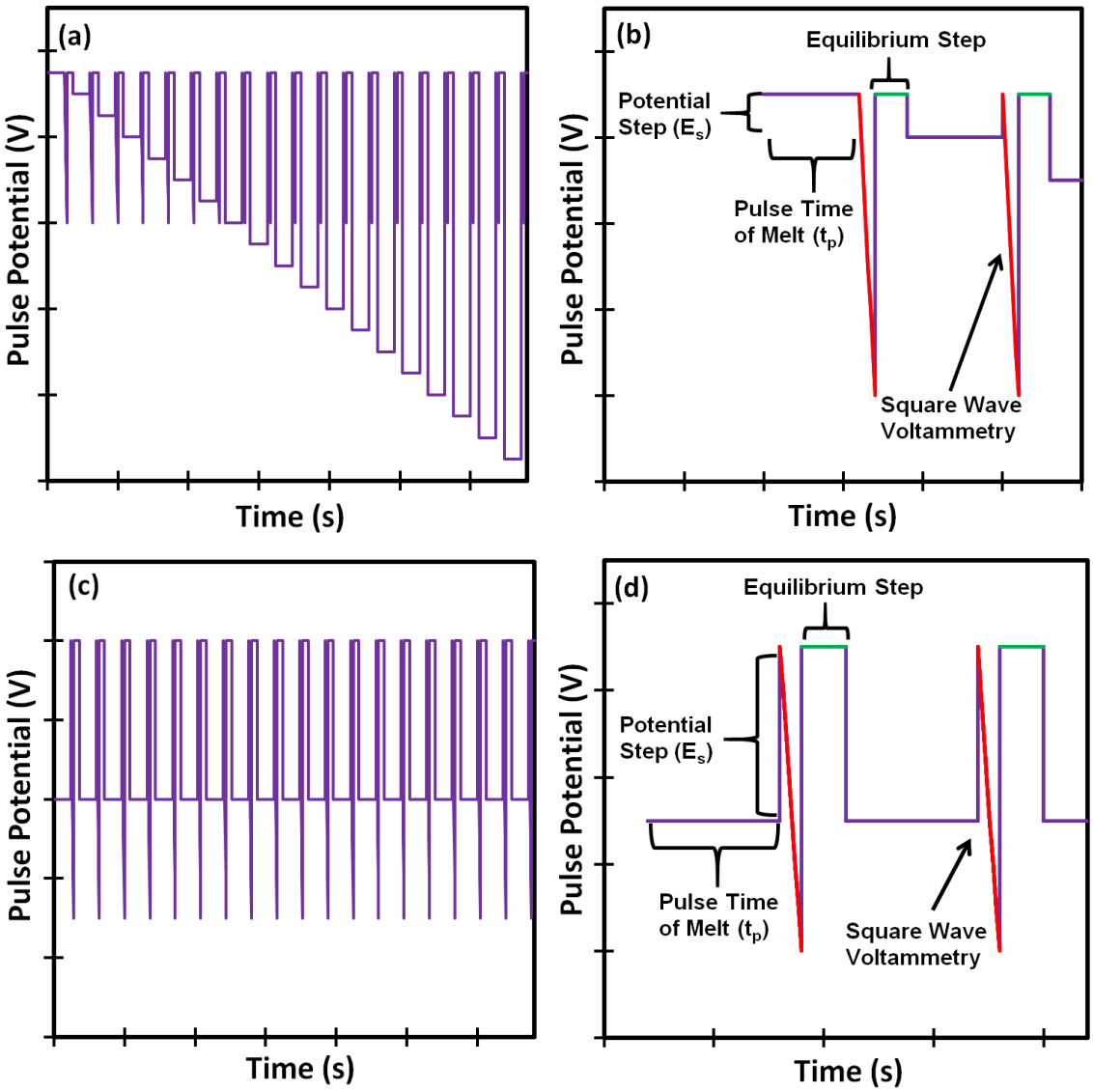

Figure 39. *Schematic of the electrochemical melting routines. Each potential pulse is held for a fixed pulse time,* $\mathbf{t_p}$. *After each pulse, the potential returns to an equilibration step for 10 s before a square wave voltammogram is acquired. During an e-melting experiment, the pulse potentials either* ***(a-b)*** *decrease throughout the routine or* ***(c-d)*** *remain constant for the duration of the melt. Zoomed-in snapshots of the melting routines for* ***(a)*** *and* ***(b)*** *are shown in* ***(b)*** *and* ***(d)****, respectively.*

4.3. Results and Discussion

4.3.1. Monitoring of e-Melting

The SWV signal from the MB is used to monitor the amount of target hybridized to the surface-bound probe. Initial voltammograms, before the application of destabilizing negative potentials, indicate the successful hybridization of the target DNA with the surface-bound probe DNA. Figure 40 displays the average peak currents and peak potentials of 34-bp and 18-bp duplexes before the melting routine (hybridization carried out at 55 °C). These values are representative of initial peak currents observed for the other sequences used in this work and hybridization at room temperature. The initial voltammograms are measured after a 5-minute rinse to remove non-specifically absorbed target from the surface. In absence of surface-bound probe, the MB signal from non-specifically bound target DNA is well below 1 mA (data not shown). This indicates that the mercaptohexanol layer is successfully preventing most non-specific absorption. Though all electrodes were prepared the same, i.e. incubation times and rinsing protocols are the same, there is still considerable spread in the initial peak currents and potentials. This random error indicates that there is variability in the initial density of target bound on the electrode and/or a difference in the accessibility of the MB indicators. Nonetheless, we have found that peak currents above of at least 4 µA give relatively consistent e-melting results. Furthermore, the performance of the DNA modified-electrodes was found not to depend on the initial peak potential.

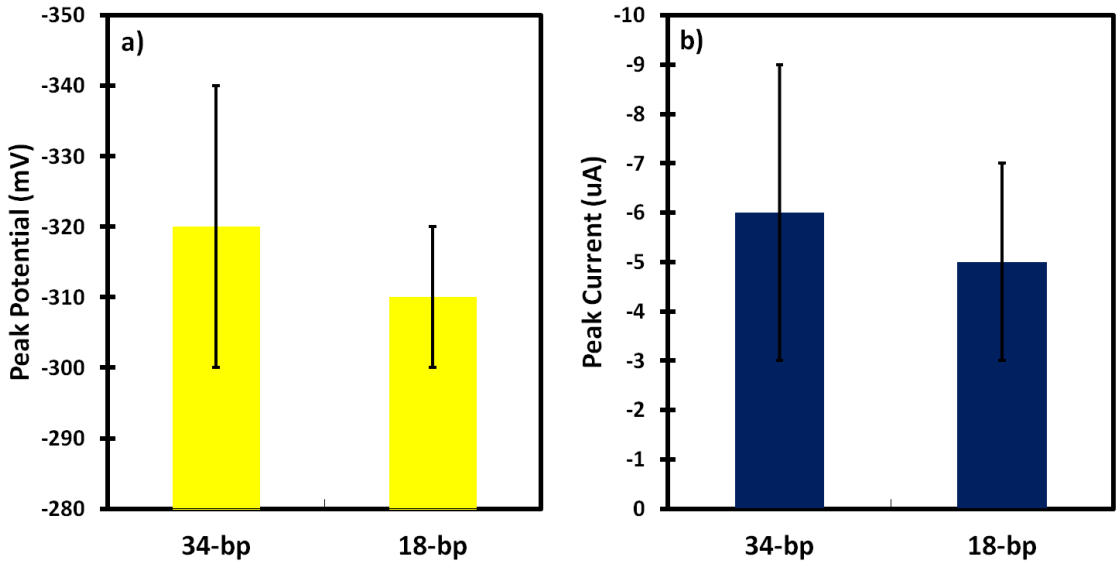

Figure 40. *Bar graph representation of average peak potential (a) and average peak current (b) from square wave voltammograms of methylene blue tagged duplexes at two different lengths. Each SWV was taken using the parameters stated earlier in 10 mM Tris solution.*

To show the effects of negative potential pulses on the peak current, a collection of the baseline-subtracted voltammograms obtained during the melt routine is plotted in Figure 41. This experiment

involved 34-bp complementary duplexes hybridized at 55 ºC (to prevent hairpins). The potential was stepped from -0.1 V to -1.0 V (vs. Ag/AgCl in 1.0 M KCl) with 10 mV increments and a pulse time of 480 s. After each potential pulse, the working electrode was returned to an equilibration potential of -0.1 mV for 10 s before acquiring the voltammogram. As seen in Figure 41, the peak current decreases as a more negative potential is applied to the electrode. This supports the claim that negative potentials dehybridize the DNA duplex, causing the target strand to diffuse into the solution.

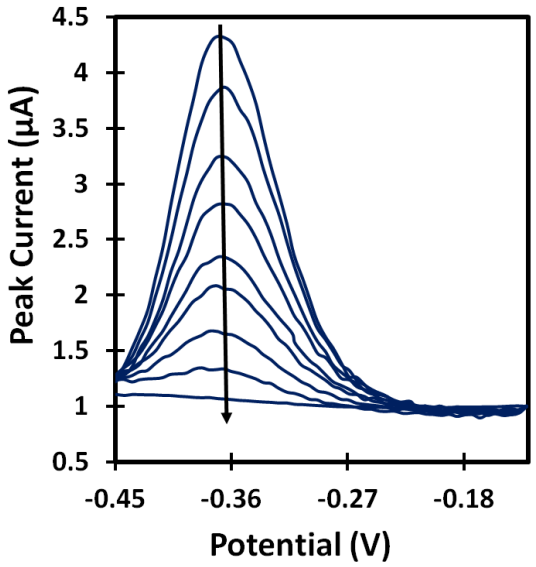

Figure 41. *Overlay of a subset of MB-tagged DNA SWV voltammograms during e-malting experiment. The experiment involved 34-bp complementary duplexes hybridized at 55 ºC. The potential was stepped from -0.1 V to -1.0 V (vs. Ag/AgCl in 1.0 M KCl) with 10 mV steps and a pulse time of 480 s. After each potential pulse, the working electrode was returned to an equilibration potential of -0.1 mV for 10 s before acquiring a voltammogram. The arrow indicates the direction of progressively more negative pulse potentials.*

4.3.2. Melting Curves – Scanning Potential

By incrementally decreasing the potential, we acquired potential melting curves at various pulse times. In these experiments, the potential was decreased from -0.1 V to -1.0 V in 10 mV steps and each pulse was held for a given pulse time (t_p). In between each applied potential pulse, a pulse of -0.1 V equilibrated the system and SWV was used to monitor the extent of melting. The baseline of each voltammogram was fit with a linear line and subtracted to determine the peak current (i_p). The peak current of the voltammograms were then normalized with respect to the first SWV peak current and plotted against the applied potential, resulting in a potential melting curve as seen in Figure 39. The 480 s pulse time (**purple, ●**), corresponds to the data discussed in the last paragraph. Decreasing towards -400 mV, no loss in MB signal is observed. Instead, a slight increase in peak was often observed. This may be caused by structural rearrangements of the thiol monolayer, reorientation of the DNA duplexes and/or reorientation of the MB moieties relative to the electrode surface.[153] Beyond -400 mV, the signal

decreases as the DNA melts, until around -800 mV. It should be noted that at potentials beyond -600 mV, thiol desorption can occur, so that at least some of the signal loss is due to desorption of the entire duplex. This will be discussed later. These melting curves are analogous to temperature melting curves and allow us to determine the melting potential. Like the melting temperature, melting potential in our experiments is the potential at which half of the DNA has dehybridized and diffused away from the surface. The melting curves were fit with the following stretched sigmoidal function:

$$E(t) = \frac{\phi_1}{1 + e^{\frac{\phi_2 - t}{\phi_3}}} \quad \text{(Eq.19)}$$

where ϕ_1 is the peak current maximum (equal to 1 for the normalized peak current data), ϕ_2 is the melting potential, and ϕ_3 describes the broadness of the curve. The broadness of the sigmoid provides information on the electrostatic effects at the surface i.e. the rate that the target strand starts to "unzip" and diffuse into the solution.[155]

Figure 42 depicts the effect of pulse time on melting curves. The pulse times used were 5 s, 60 s, and 480 s. As the pulse time increases, the curves shift more to the right as the apparent melting potential becomes more positive. At 5, 60, and 480 s pulse times, the melting potentials are -750 ± 50 mV, -680 ± 50 mV, -570 ± 30 mV, respectively. Although it has been reported that the melting potential is dependent on the stability of the DNA duplex,[156] the oligonucleotide sequence, environment, pH, and ionic strength are the same for each of these melts; thus the change in the melting potential is presumably caused by kinetic effects. One hypothesis is that DNA melting starts at the electrode surface, where the electric field is the highest.[157] But the subsequent SWV signal from loss of MB, requires that the DNA have time to completely dehybridize and diffuse away from the surface. Therefore, longer pulses allow more time for the DNA to melt and diffuse away, leading to a lower observed melting potential. It was found that the observed melting potential did not continue to shift positive beyond a pulse time of 480 s, indicating that this is enough time for the melted DNA to leave the surface.

The broadness of the sigmoidal fit is less affected by the pulse time. At 5 s, 60 s, and 480 s ϕ_3 is found to be 48 ± 5 mV, 58 ± 5 mV, and 65 ± 1 mV, respectively. As pulse time decreases, the sigmoid becomes less broad: the signal drops more sharply around the melting potential. This suggests that the more rapid potential pulsing at shorter pulse times may play a role in facilitating efficient diffusion of single-stranded DNA away from the surface. Essentially, the rapid influx and efflux of ions at the electrode surface enhance mixing and diffusion of the free strands into the bulk of the solution resulting in a steeper decrease in the SWV signal. Similar potential-assisted diffusion effects have been reported for the enhanced formation of thiol monolayers and DNA hybridization at gold surfaces.[158,159]

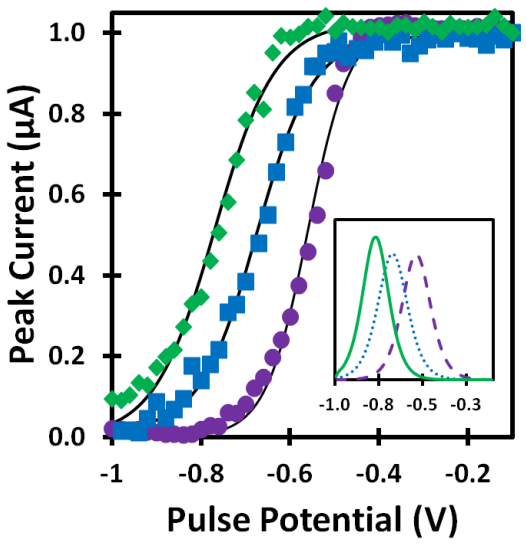

Figure 42. *Normalized peak currents plotted versus the pulse potential of fully complemented 34 – base pair DNA duplexes. The potential decreases from -0.1 V to -1.0 V at 10 mV steps. Each data point reports on the amount of MB-tagged target still present at the electrode surface. From left to right, the curves correspond to melting of DNA at various pulse times: 5 s (**green,** ♦), 60 s (**blue,** ■), and 480 s (**purple,** ●). The first derivatives of the melting curves are shown in the inset to depict the change in melting potential. 5 s (**green,** solid), 60 s (**blue,** dotted), and 480 s (**purple,** dashed).*

Next, we investigated the effect of hairpins, sequence length, and mismatches on the melting curves. These experiments were done at potentials of -0.1 V to -1.0 V in 10 mV steps and a pulse time of 480 s. Table 3 displays the sequences for 18-bp duplex, 34-bp duplex with hairpins (presence favored by hybridizing at room temperature), and 34-bp duplex with single mismatch DNA (no hairpins). The melting temperatures, calculated with the nearest-neighbor two-state model, of the fully complementary 34-bp sequence, the mismatched 34-bp sequence, and the 18-bp sequence are 59.8 ºC, 57.9 ºC, and 47.8 ºC (Integrated DNA Technologies, https://www.idtdna.com/calc/analyzer, 0.25 uM Oligo and 50 mM Na^+). Although the conditions used in this model do not exactly correspond to the conditions used in our experiments, they do provide an indication of the relative stabilities of these duplexes. Melting temperatures for the hairpin-containing duplex were not calculated due to uncertainty about the structure and extent of hybridization. Nevertheless, the hairpin is expected to destabilize the 34-bp duplex relative to the hairpin-free duplex. Overall, if melting potential is an indication of stability, the hairpin-containing duplex, the single mismatch duplex, and the 18-bp duplex are all expected to melt at less negative potentials than the fully complementary, 34-bp hairpin-free duplex.

Hybridization of the 34-bp sequence at room temperature results in a stable hairpin on both the probe and target strands, which should disrupt full hybridization. These hairpins have melting temperatures of 33.4 ºC and 44.5 ºC on the probe and target, respectively, as shown in Table 3 and Figure 43. To our surprise, the hairpin-containing 34-bp duplex displays a more negative melting potential (-590

mV) compared to the hairpin-free duplex (-570 mV). Furthermore, there are no significant differences between the broadness factors. It is also worth mentioning that the initial peak current values are more reproducible when the electrode is fully annealed without any hairpins. The apparent enhancement of stability associated with the hairpin cannot be easily rationalized in terms of simple electrostatic repulsion between phosphate backbone and electrode. Some insight may be gained by closely inspecting the work of Mahajan et al.[95] In that work, the melting temperatures and melting potentials of three 22-mer duplexes were compared: a wild type target (WT) which was fully complementary to the probe, a single-mismatch target (1653C/T), and a target containing a triple deletion (ΔF508). The melting temperatures are reported to be ~51 ºC, ~46.5 ºC, and ~39.5 ºC for the WT, 1653C/T, and ΔF508 targets, respectively. While it was found that the ΔF508 target (triple deletion) is less stable in the electric field than the single mismatch and wild type targets, the difference was not as large as anticipated. The secondary structure and tertiary structure for the ΔF508 duplex was not discussed in that work, but the triple deletion is expected to disrupt hybridization on either side of the mutation, potentially leading to a disruption of the double helical structure itself. Their result, and ours, suggests that deviations from the rigid cylinder-like structure typical of short DNA duplexes may provide enhanced stability against applied electric fields despite the thermodynamic instability imparted by these motifs.

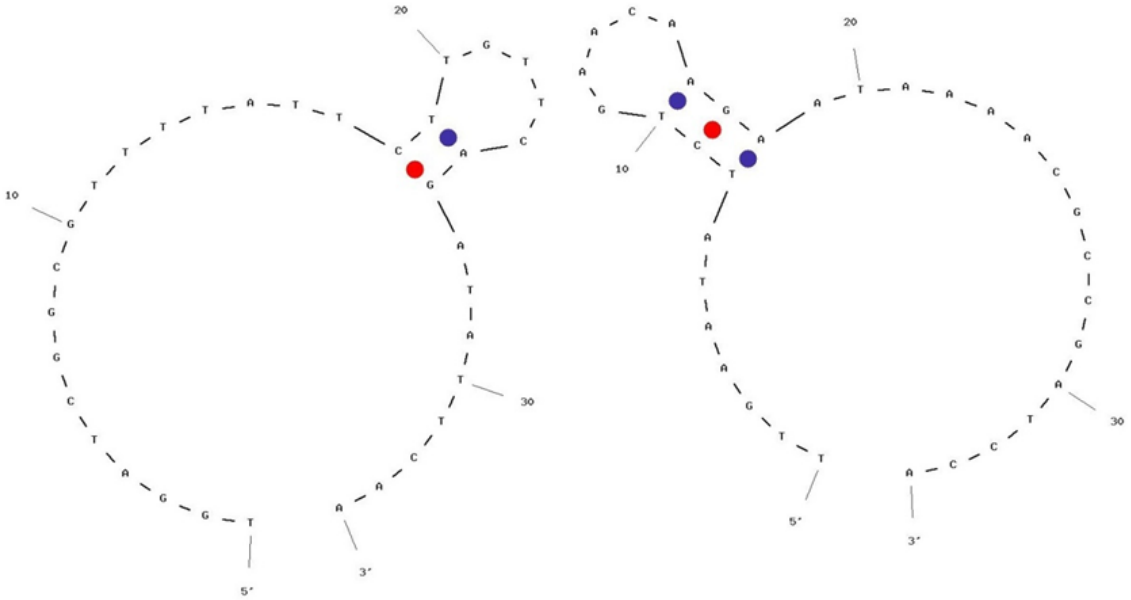

Figure 43*. Image showing the location of the hairpin in a) 34 – base pair probe and b) 34 – base pair target, from IDT Oligo Analyzer*

The 18-bp sequence was found to have a melting potential of -570 mV, the same as the hairpin-free 34-bp sequence. Figure 44 displays the melting curves of the 34- and 18-bp sequences to show that both the melting potential and broadness factor are similar. Given that this duplex's melting temperature

is 10 ºC lower than the 34-bp duplex, the results were not expected. Recall that a relatively small difference of 1.9 ºC between the fully complimentary and single mismatch 34-bp sequence resulted in a 20 mV difference in melting potential. Here, a 10 ºC difference between the 18-bp sequence and the 34-bp 100% complimentary sequence does not result in a significant difference in the melting potential. This suggests that longer sequences may not necessary contribute to enhanced stability in the electric field, which originates at the electrode surface and is predicted to extend less than 10 nm into the solution.

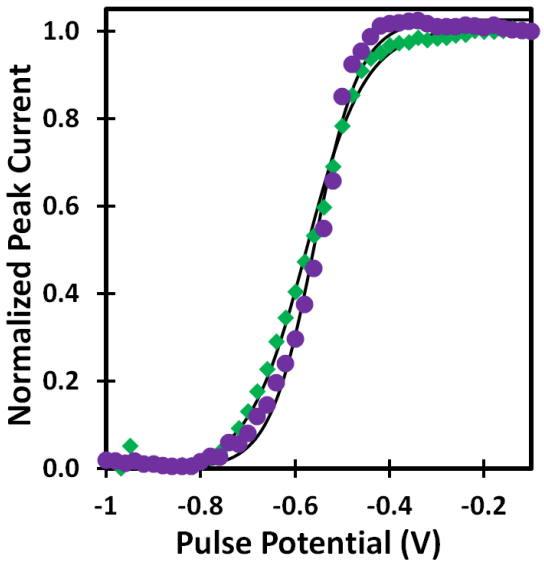

Figure 44. *Normalized representative melting curves of 34-base pair (**purple,** ●) and 18-base pair (**green,** ♦) DNA duplexes. The potential decreases from -0.1 V to -1.0 V at 10 mV step with a pulse time of 480 s.*

4.3.3. Time Traces at Constant Pulse Potential

Unlike the melting routine presented in the last section, time traces monitor the SWV signal as a function of time between applied pulses of constant potential (see Figure 39cd). Much like in the previous section, the baseline-subtracted peak current reports on the presence of hybridized DNA, via MB, at the electrode surface. These peaks currents are plotted versus time and normalized to the initial peak current. In each case, the curves are fit with a sum of exponential functions of the form:

$$\boldsymbol{i(t) = A_1 e^{-(t/\tau_1)} + A_2 e^{-(t/\tau_2)}} \qquad \text{(Eq.20)}$$

Since the data is normalized, $\boldsymbol{A_1 + A_2 = 1}$. Therefore,

$$\boldsymbol{i(t) = A_1 e^{-(t/\tau_1)} + (1 - A_1) e^{-(t/\tau_2)}} \qquad \text{(Eq.21)}$$

where $\boldsymbol{A_1}$ is the amplitude for the first exponential and $\boldsymbol{\tau_1}$ and $\boldsymbol{\tau_2}$ are time constants of our melting experiment. These time traces at constant potential provide a more sensitive approach toward interrogating duplex stability. Generally, $\boldsymbol{\tau_2}$ was found to be orders of magnitude larger than $\boldsymbol{\tau_1}$ and is

responsible for the slow decay at long times, whereas τ_1 was found to be sensitive to the duplex under study: a larger value of τ_1 indicates that the duplex is more stable in the high electric fields and requires more time to melt. Time traces could not be fit with a single exponential function. However, the time constant, τ_1, proves to be sufficient enough to provide us with information about e-melting.

First, we studied the effects of pulse time on the constant potential time traces using 34-bp fully complementary duplexes. Figure 45 depicts the effect of pulse time on time traces with constant potential pulses at -750 mV. At 60 s, 240 s, and 480 s pulse times τ_1 values were 52 ± 9 s, 110 ± 10 s, and 170 ± 40 s, respectively. As pulse time increases, so does τ_1, meaning that the target strand is removed from the electrode at a lower rate. As previous stated, pulse enhanced stirring occurs as the potential is pulsed between potentials.[158,159] At shorter pulse times this stirring effect enhances removal of DNA from the surface, resulting in a shorter τ_1, as observed.

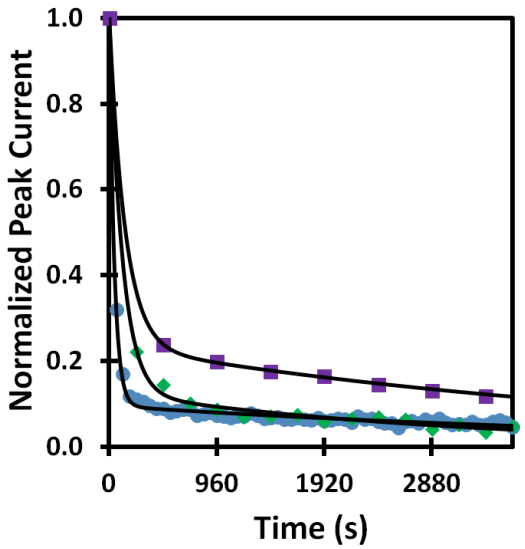

Figure 45. *Normalized SWV peak current vs. time of fully complementary, 34-bp DNA duplexes. The potential was held constant at - 750 mV and the pulse time varied at 60 s (**blue,** ●), 240 s (**green,** ♦), 480 s (**purple,** ■).*

Next, we investigated the effects of the pulse potential (using the same duplex as above). Figure 46 depicts time traces at -500 mV, -600 mV, and -750 mV using a pulse time of 480 s. A control is also shown in which an open cell potential replaces each potential pulse, i.e. no potential was applied between voltammograms. During the control, no MB signal is lost. However, we do see a slight increase in peak current, possibly due to structural rearrangements, as previously noted for the melting curves.[153] As pulse potential becomes more negative, τ_1 decreases. At -500 mV, -600 mV, and -750 mV τ_1 values are 2000 ± 200 s, 400 ± 80 s, and 150 ± 10 s respectively.

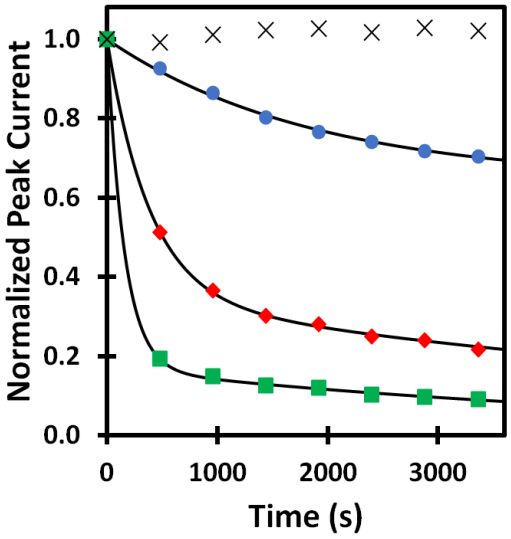

***Figure 46**. Normalized SWV peak current vs. time data with the pulse time being held constant at 480 s while the pulse potential varied at -500 mV (**blue,** ●), -600 mV (**red,** ♦), and -750 mV (**green,** ■). The control (**black, x**) was done by taking square waves every 480 s.*

Next, the dependence of sequence length, hairpins, and mismatches was carried using this constant potential routine. In each instance, the duplex was melted at two potentials: -500 mV and -750 mV, with a pulse time of 480 s. As seen in Figure 46, -500 mV is low enough to start melting and -750 mV is sufficient to melt most of the target strand. First, we will examine how the 34 base-pair duplexes hybridized at 55 ºC and room temperature compare to determine how the time traces are affected when hairpins are introduced into the system (Figure 47). At -500 mV, the τ_1 values are 2000 ± 200 s and 5000 ± 1000 s for fully complementary and hairpin-containing duplexes, respectively. At -750 mV, the τ_1 values are 150 ± 10 s and 300 ± 100 s for fully complementary and hairpin-containing duplexes, respectively. Based on these values, our method is sensitive enough to discern whether the sequence has a hairpin. Typically, a hairpin in the sequence should lower the overall stability, leading to a lower melting temperature or a faster rate in melting. In this case, the hairpin-containing duplex melted more slowly than the fully hybridized DNA strand. This apparent increase in stability towards the applied electric field was also observed for the scanning potential melting curves already discussed. Further experiments will be needed to determine the mechanism by which this enhanced stability occurs, which will provide further insight into the overall driving force for electrochemical DNA melting.

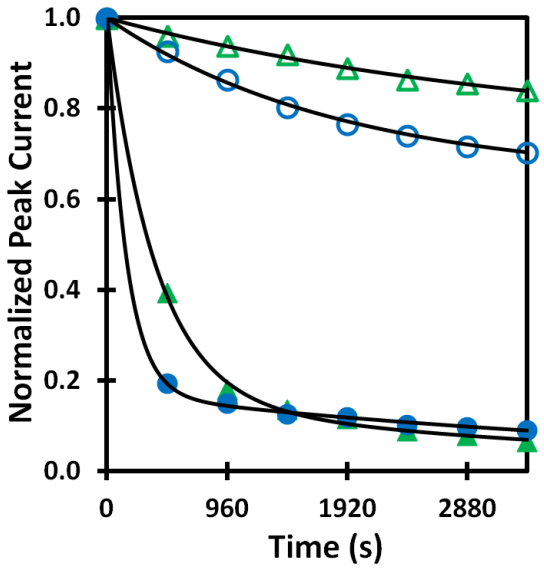

Figure 47. *Comparison melting at constant pulse potentials for 34-bp fully complementary hybridized at 55 ºC (**blue,** ●) and hairpin when hybridized at room temperature (**green,** ▲). Time traces were acquired at pulse potentials of -500 mV (open symbols) and -750 mV (closed symbols), with a pulse time of 480 s.*

Next, the 34-bp (hairpin-free) and 18-bp sequences are compared (Figure 48). At -500 mV, the τ_1 values are 1600 ± 700 s and 900 ± 100 s for 34-bp and 18-bp duplexes, respectively. At -750 mV, the τ_1 values are 150 ± 10 s and 140 ± 20 s for 34-bp and 18-bp duplexes, respectively. As already reported for the scanning potential melting curves above, the electrochemical melting used here is not very sensitive to the length of the oligonucleotide. As before, we speculate that differences in the sequence beyond the Debye length, i.e. extent of the electric field, do not contribute to the overall melting behavior of the duplexes.

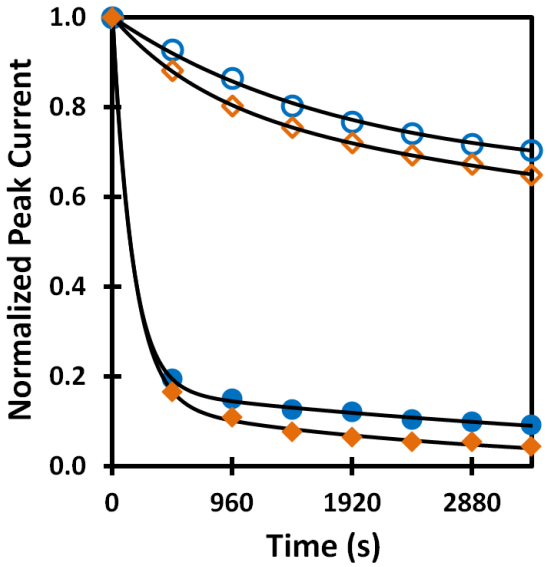

Figure 48. *Comparison melting at constant pulse potentials for 34-bp (**blue,** ●) and 18-bp (**orange,** ♦) at pulse potentials of -500 mV (open symbols) and -750 mV (closed symbols) and pulse time of 480 s.*

Constant potential time traces are promising for differentiating between complementary and mismatch strands. In Figure 49 the time constants are plotted versus the pulse times for a pulse potential of -750 mV. At 60 s and 240 s pulse times, the time constants of the two strands cannot be distinguished. However, at 480 s, there is a significant difference between the τ_1 of the complementary and mismatch duplex. The mismatch strand has a lower time constant than the complementary strand suggesting less stability of the mismatched duplex, as expected. Using a pulse time of 480 s, time traces were also taken at both -500 mV and compared to -750 mV. At both potentials, the single mismatch melts at a higher rate than the fully complementary duplex, as shown in Figure 50. The differences in melting behavior are amplified at the lower melting potential, i.e. the difference between the fully complementary and mismatched duplex is largest at -500 mV. This is in part due to the rapid decay of the signal to nearly zero after the first 8-minute pulse at -750 mV. This suggests that the large destabilization induced by the -750 mV pulse is less discriminant towards small difference in stability, essentially removing most of the DNA in a very short time, no matter its stability. It should be noted that significant thiol desorption is observed at -750 mV, which also contributes to the decreased dependence on duplex stability, as will be discussed later.

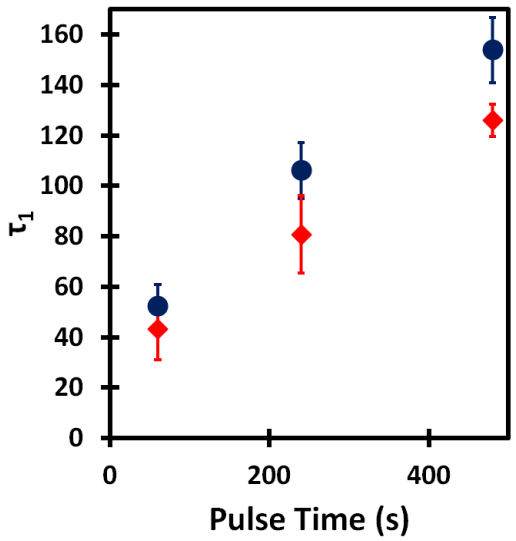

Figure 49*. Time constant (τ_1) vs. pulse time of constant potential time traces taken at pulse times of 60, 240, and 480 s, with a pulse potential of -750 mV for 34-bp complementary (**blue** ●) and 34 bp single mismatch duplexes (**red** ♦).*

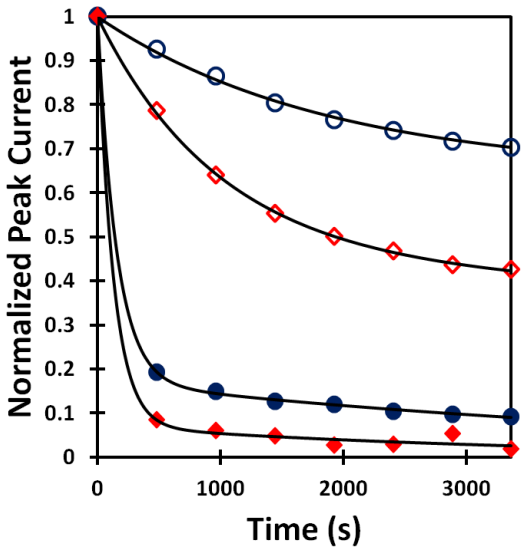

Figure 50. *Comparison of constant current time traces for 34-bp complementary (**blue** ●) and 34-bp single mismatch duplexes (**red** ♦). Times traces were obtained with a pulse time of 480 s at pulse potentials of -500 mV (open symbols) and -750 mV (closed symbols).*

4.3.4. DNA e-Melting vs. Thiol Desorption

Understanding the extent of thiol desorption is important for the optimization of the methodology and increased reusability of the sensor. The simultaneous reduction of thiol bonds and DNA melting both lead to signal loss, complicating our analysis and decreasing our sensitivity to duplex stability. Thiol desorption is reported to begin around -650 mV, and it becomes significant around -1.3 V.[160] To study the effects of applied potential on thiol desorption, we used a potential pulse routine on two different types of duplexes: one where the duplex has a MB-tagged probe and the other with a MB-tagged target (shown in Figure 51). Both strands have the same sequence as the fully complementary 18-bp probe and target strands used above. The length of the DNA should not affect the extent of desorption, and thus this duplex should provide insight into the behavior of the 34-bp sequence as well.[161] We applied a constant potential of -500 mV and -750 mV with a pulse time of 480 s, and monitored the SWV signal change of MB. SWV signal change from the tagged probe (Figure 51A) results only from desorption of the thiol-gold bond and subsequent loss of the entire duplex, while signal change from the tagged target (Figure 51B) can result from DNA melting, i.e. the target leaving the surface, and thiol desorption.

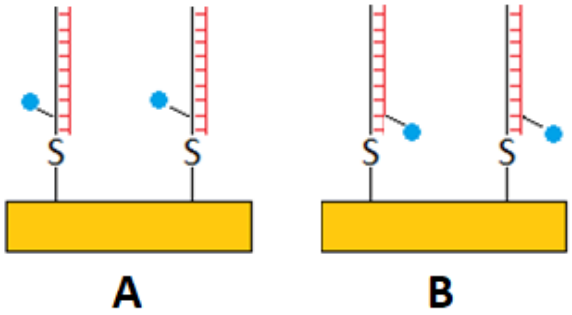

Figure 51*. Schematic of DNA duplexes on gold electrodes: (A) methylene blue-tagged probe with blank target (B) blank probe with methylene blue-tagged target.*

Loss of the tagged probe resulting from reduction of thiol bonds appears to occur at both -500 and -750 mV, however, the effect is greater at a higher potential: ~10% signal loss at -500 mV compared to the ~60% at -750 mV. When the target is tagged with MB and signal changes can be due to simultaneous desorption and melting, signal loss occurs at a significantly greater rate. The curves also vary in their limiting current at long times. After 16 minutes, the curves with the tagged target (Figure 52, purple ♦) begin to flatten out illustrating that most of the target has diffused from the electrode surface after melting and desorption of the duplex. Subsequent loss of untagged probe occurring after 16 minutes does not result in additional signal loss, but desorption of tagged probe results in continued signal loss (Figure 52, filled ●). This large contribution from desorption results in the smaller difference between complementary and mismatched DNA observed at -750 mV (Figure 52, closed symbols). On the other hand, at -500 mV the difference in signal between tagged probe and tagged target increases through the first 32 minutes or so and then plateaus (Figure 52, open symbols). This suggests that melting occurs primarily within the first 32 minutes, after which, only desorption occurs at a slow rate. These results suggest that melting at -500 mV should lead to improved reusability of the electrodes while still allowing mismatch discrimination.

We should also note that a potential of -500 mV is much less negative than the values reported by the Bartlett group.[95] In their work, potentials between -800 mV to -1.3 V are necessary to observe melting. We believe that this discrepancy may be due to the differences in our thiol linker and electrochemical melting routine. The work by Bartlett utilizes a triple disulfide linkage to gold, while our work relies on the standard single thiol-gold bond. Furthermore, their electrochemical routine employs a linear scanning potential and SERS to monitor the extent of the melting. Our system utilizes potential pulses to melt, a pulse of -100 mV to equilibrate the system, and then the SWV. As discussed earlier, this rapid pulsing of the potential may induce mixing and agitation of the species within the electrical double-

layer, including the DNA strands, resulting in enhanced melting and/or diffusion of DNA into the bulk of solution.

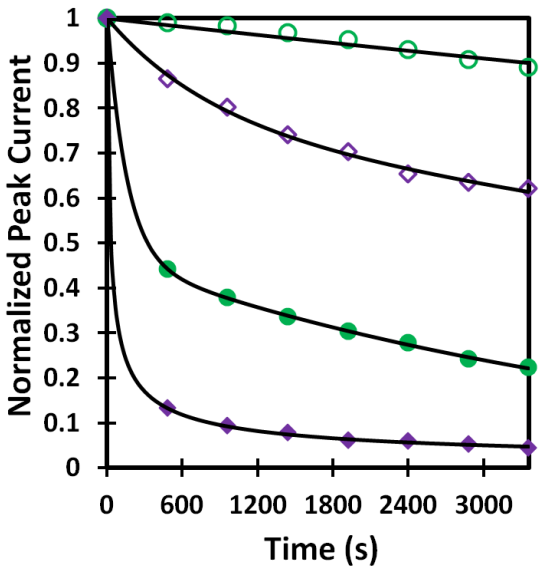

Figure 52. *Comparison of melting and desorption during constant potential melting routine obtained for the 18-bp complementary duplexes with either MB-tagged probe (**green** ●) or MB-tagged target (**purple** ♦). The pulse potential was -500 mV (open symbols) or -750 mV (closed symbols) with a pulse time of 480 s.*

As outlined above, we investigated the effects of pulse potential, pulse time, sequence length, hairpins, and mismatches on the electrochemical melting of DNA duplexes using periodic SWV to monitor the extent of dehybridization. Based on these observations, we propose that the destabilizing electric field not only affects the kinetics of melting, presumably by decreasing the activation energy for dehybridization and enhancing the rate of diffusion, but also determines the fraction of hybridized duplexes remaining at equilibrium, even with no free DNA concentration in solution. With the low concentration of electrolyte in our experiments, the kinetics of e-melting are accelerated because of the weaker counterion screening.[147] As the potential is pulsed negative, the buffer solution must supply the positive ions needed to maintain the counter charge in the double-layer. There exists a balance between the duplex stability and the necessary double-layer charge, and as the electrode potential becomes more negative, the necessary double-layer charge increases, requiring additional counterions to accumulate. For a given potential, only some fraction of the bound DNA needs to be removed before the electric field is sufficiently screened to prevent further dehybridization. Thus, we see that at -500 mV, only some fraction of the DNA melts, after which only slow desorption occurs. Gong et al. found that at low ionic strength hybridization ceased when counterions from the solution cannot provide the necessary charge screening between the probe, target, and electrode.[160] Here, we observe the same phenomena but for dehybridization – at low ionic strength the DNA melts until counterions from solution can provide the necessary charge

screening to stabilize the remaining duplexes and halt further melting. This potentially provides a simple electrochemical means of controlling the extent of hybridization and using applied potential pulses to select for fully hybridized duplexes over partially hybridized or mismatched duplexes.

4.4. Conclusion

We have developed a purely electrochemical method for melting and monitoring surface-bound double-stranded DNA. Electrochemical monitoring coupled with electrochemical melting results in a facile and versatile technique for studying the behavior of DNA exposed to high electric fields. Furthermore, it provides a robust and simple platform for further development of DNA biosensors. The resulting melting curves display a characteristic "melting potential" which reports on the stability of the surface-bound duplex in the presence of the applied electric field. Overall, the scanning potential melting curve routine is not robust enough to differentiate between different sequence lengths or single mismatches. Figure 53 summarizes that compares the melting potentials and broadness factors of the different duplexes used in this work. Further optimization will need to be done to improve the reproducibility of this experiment and improve rehybridization and re-usability of our electrodes. Time traces of hybridized DNA under the application of a constant applied potential also report on the stability of the DNA. Under optimized conditions (i.e. 480 s pulse time and -500 mV pulse potential) time traces could not report differences in sequence length. However, they can distinguish between complementary and single base-pair mismatches, as shown in Figure 54.

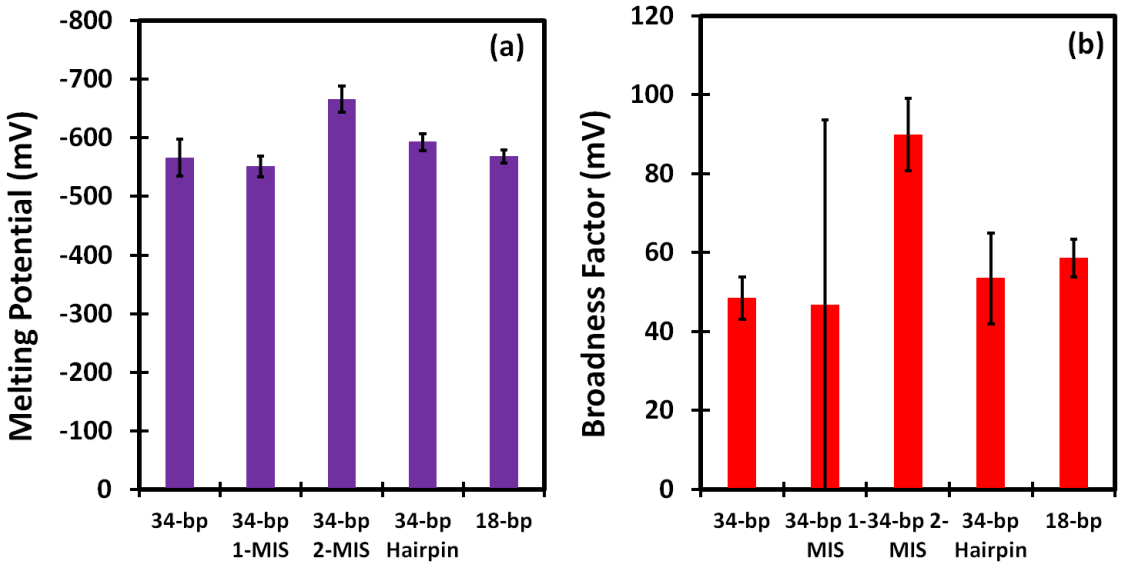

Figure 53. *Summary of average melting potentials (a, purple) and broadness factor (b, red) for the 5 DNA duplexes in this work.*

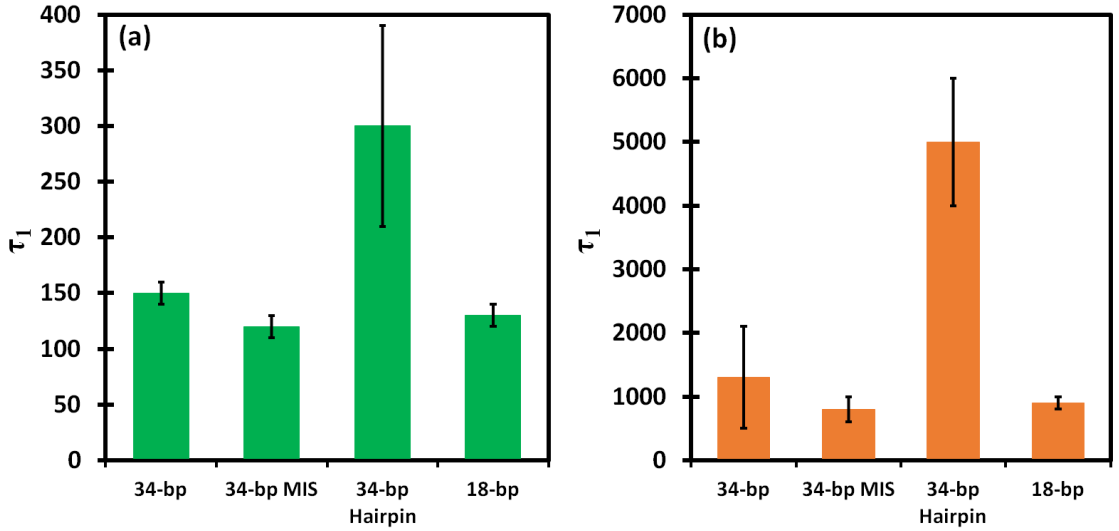

***Figure 54**. Summary of time constant (τ_1) for the four DNA duplexes obtained from constant potential time traces at -750 mV (a, **green**) and -500 mV (b, **orange**) with a pulse time of 480 s*

.

Chapter 5: Development of a label-free electrochemical method for the detection of DNA biomarkers

5.1. Introduction

The development of electrochemical DNA (E-DNA) sensors is an area of active research with promising applications in point-of-care detection of biomarkers for medical diagnostics and forensics. Because electrochemical sensors only require simple electronics, are easily miniaturized, and can be multiplexed, they are promising platforms for the development of handheld, easy to operate, personalized medical devices, like the blood glucose meter. [105,137,163] Furthermore, E-DNA sensors have been used to detect breast and lung cancer.[164,165] In this work, we are developing an E-DNA sensor that utilizes the high electric fields generated at electrode surfaces to manipulate the hybridization of DNA. Sufficiently negative electrical potentials have been shown to not only orient DNA in an upright position,[166] but also to inhibit hybridization and initiate melting of hybridized DNA.[149,167] Essentially, the applied potential can be used to destabilize and melt the DNA in a process known as e-melting. The potential and rate at which this melting occurs depends on the stability of the DNA duplex, i.e. the sequence, length, and presence of mismatches, deletions, and other mutations. In this way, the behavior of DNA in the presence of high electric fields has diagnostic value. The hybridization and melting of DNA via negative potentials is well studied and in existing reports, the presence of DNA is monitored using optical techniques.[95,134,149] Utilizing this bimodal system (simultaneous electrochemical control and optical measurement) can be cumbersome because of the specialized equipment required to perform these experiments. In the previous chapter, we circumvent the bimodal measurements by utilizing a fast and sensitive voltammetric approach for monitoring the DNA. Our method for melting and monitoring surface-bound DNA includes a sequence of potential pulses to melt the DNA duplex while square wave voltammetry is used to monitor the extent of melting in real time. Using this approach, we have successfully melted short DNA sequences in which the target DNA is covalently modified, i.e. labeled, with the redox reporter methylene blue.

To develop a label-free sensor, in which our target strand is not labeled, we employ a molecular beacon-like set up.[168,169] A typically molecular beacon consists of a probe sequence that forms a stable stem loop structure. One terminus of the probe is labeled with a fluorophore, while the other has a quencher; creating a sensor that "turns on" when the loop breaks and forms the rigid helix due to hybridization of the target. For our electrochemical measurements, the single-stranded molecular beacon is modified with a thiol bond at one terminus (to form a monolayer on a gold electrode) while the other is labeled with methylene blue. Square-wave voltammetry reports on the structural configuration (loop or helix) by monitoring the signal of methylene blue based on its proximity to the electrode surface. To demonstrate the applicability of our sensor to a real-world application, the RSAD2 gene is used as the

target in this study.[166] The RSAD2 gene is used to code Viperin, an interferon-inducible protein that inhibits the replication of a variety of viruses by apparently diverse mechanisms.[170]

5.2. Experimental Method

5.2.1. Preparation of Materials

The sequences of the 31-base pair probe, 25-base pair target, and 25 base-pair 2-mismatch target DNA strands (outlined in red) are shown in Table 1 and were purified by dual HPLC (LGC Biosearch Technologies, Petaluma, CA). The probe is labeled with a thiol group through a 6-carbon linker on the 5' end and an amino-tag on the 3' end to covalently tether methylene blue to the strand (outlined in blue). The MB solution was added to the oligo in a ratio of 10:1 to react. The reaction was run for 24 hours, in the dark, at room temperature. After the reaction, the solution was desalted and purified using four 25 g Sephedex columns (GE Healthcare Life Sciences, Pittsburgh, PA) placed in series on an FPLC (GE AKTApure). The probe has 6 base pairs on each end that are complimentary to each other, forming the hairpin loop (outlined in green). Note that only the probe is labeled, not the target strands.

Table 4. *DNA Sequences*

Name	Sequence
25-bp Fully Complementary duplex	Probe: 5′HS-C6-GTG TAG AAA GCG ACT CTA TAA TCC CTA CAC T-(MB)3′ Target: 3′ CTT TCG CTG AGA TAT TAG GGA TGT G 5′
*25-bp Double **Mismatch** duplex*	Probe: 5′HS-C6-GTG TAG AAA GCG ACT CTA TAA TCC CTA CAC T-(MB)3′ Target: 3′ CTT TCG CTG AGG GAT TAG GGA TGT G 5′

Sulfuric acid (Pharmco-Aaper, 95-98 wt%, ACS grade), hydrogen peroxide (BDH/VWR Analytical, 30 wt% in H_2O), hydrochloric acid (Pharmco-Aaper, 36.5-38 wt%, ACS grade), potassium ferricyanide (III) (Sigma-Aldrich, >99 wt%), tris(2-carboxyethyl)phosphine-HCl (Sigma-Aldrich, >98 wt%, TCEP), 1-mercaptohexanol (Sigma-Aldrich, 97 wt%, MCH), Phosphate Buffered Saline tablets (Sigma-Aldrich, >98 wt%, PBS), Tris base (JT Baker, 99.9 wt%), NaCl (Sigma Aldrich, ≥99 wt%), KCl (EM Science, 99 wt%), $MgCl_2$ (Johnson Matthey Electronics, 97.5 wt%), and EDTA (Sigma, ≥99 wt%) were used as received. Solutions were made using 18 MΩ distilled water.

Four buffers were prepared and used as follows: (1) Probe incubation was performed using a PBS solution (10 mM phosphate buffer, 1.0127 M NaCl and 3.7 mM, and MgCl2 at pH 7.4), (2) Electrodes were rinsed in 5 mM Tris with 10 mM NaCl at pH 7, (3) DNA hybridization was performed in 10 mM Tris with 1.0 M NaCl and 1 mM EDTA at pH 7, and (4) Electrochemical measurements were performed in 10 mM Tris buffer at pH 7.

5.2.2. Preparation of Gold Electrodes

A schematic of our DNA electrodes is shown in Figure 55. To start, polycrystalline gold disk electrodes (2 mm diameter, CH Instruments, Austin, TX) were mechanically polished using 1 and 0.05 μm alumina slurry followed by sonication for 10 min in ethanol and DI water, sequentially. The electrodes were submerged in piranha solution (3:1 sulfuric acid to 30% hydrogen peroxide) for 30 s to remove residual organic matter. After thorough rinsing in DI water, the electrodes were electrochemically polished in 0.5 M H_2SO_4. The process consisted of (a) pulsing the potential at 1.6 V for 5 s, then stepping to -1 V for another 5 s for a total of 20 cycles, (b) cycling the potential from -0.2 to 1.6 V for 50 cycles at 10 V/s, (c) and cycling the potential from -0.2 to 1.6 V for 10 cycles at 50 mV/s. After cleaning, the electrodes were then cycled in 2.5 mM $K_4Fe(CN)_4/K_3Fe(CN)_6$ in 1 M KCl. The final CVs in H_2SO_4 and $K_4Fe(CN)_4/K_3Fe(CN)_6$ were used to verify the cleanliness of the surface, as described previously.

5.2.3. Preparation of DNA-Modified Electrode

After reduction of the target disulfide bond with TCEP, the probe solution was diluted to a final concentration of 2 μM using PBS buffer. The polished electrodes were incubated in this solution for 20-24 hrs in the dark at 4 ºC. Afterward, the electrodes were backfilled with 10 mM MCH in PBS buffer for 1 hr to prevent non-specific absorption of DNA. Electrodes with the probe + MCH form the hairpin loop. To form the rigid duplex, the electrodes were incubated in a solution of 2 μM target strand or 2 – bp mismatch target in the hybridization buffer (in the dark at room temperature) for 2 hours. DNA was annealed at 55 ºC and slowly cooled to room temperature to get rid of hairpins.

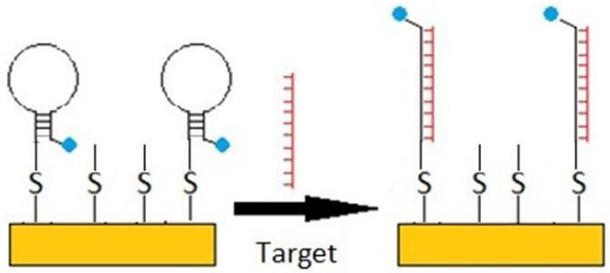

Figure 55*. Schematic of DNA sensor with and without target DNA.*

5.2.4. Electrochemical Instrumentation

Electrochemical measurements were carried out using a WaveNow potentiostat with AfterMath software (Pine Research). We employed the typical three-electrode cell, which consisted of the DNA-modified working electrode, a platinum wire auxiliary electrode (CH Instruments), and an Ag/AgCl reference electrode with 1 M KCl (CH Instrument).

5.3. Results and Discussion

5.3.1. Electrochemical Procedure

After the monolayer of probe DNA and MCH was formed, a cyclic square-wave voltammogram was taken in 10 mM Tris and 20 mM NaCl. The CSWV parameters were as follows: initial potential -0.1 V, final potential -0.45 V, amplitude 25 mV, period 6 ms, and pulse width 10 milliseconds. Since the MB is near the electrode in the hairpin loop, the signal from the voltammogram is observed (shown in Figure 56). After hybridization, the electrodes undergo electrochemical melting. First, voltammograms were taken after hybridization, when the helical structure of the double-stranded duplex forces the MB away from the electrode, leading to decreased signal. The subsequent electrochemical melting routine consisted of a potential pulse of -600 mV for 480 s to partially melt the double-stranded DNA. A CSWV was acquired immediately afterwards to report on the MB signal. As target melts away and diffuses into the solution, the probe is no longer rigid, and the MB can access the electrode surface again, leading to higher signals. A programmed time delay (during which electrode is at open cell potential) is then used for 1 minute; this is to allow the free probe strands to reform the hairpin. Another CSWV is taken to report on surface activity and the cycle of OCP and CSWV repeats for 20 minutes to monitor the reformation of the hairpin. After 20 minutes, the signal from the CSWV is stable, suggesting that the free probe strands were given enough time to reform hairpins. The process was then repeated for 2-Mismatch target DNA. The signal recovered after the melting is divided by the original signal (before hybridization) in order to calculate the percent signal regenerated value (Eq. 22).

$$\textbf{Signal Recovered} = \frac{\textbf{Peak Current After Melting Cycles}}{\textbf{Peak Current Before Melting Cycles}} \qquad \text{(Eq.22)}$$

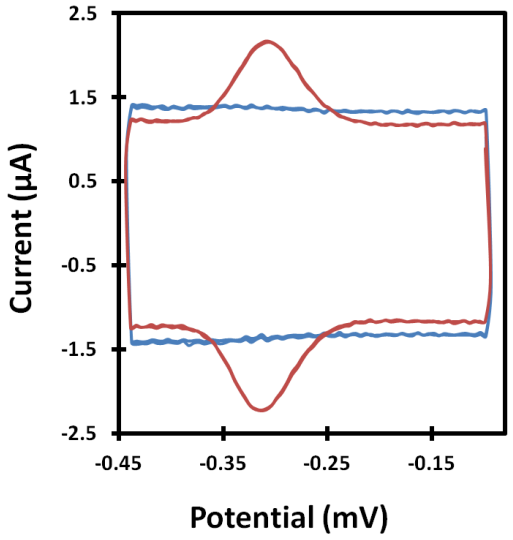

Figure 56*. CSWV before (**red**) and after (**blue**) hybridization*

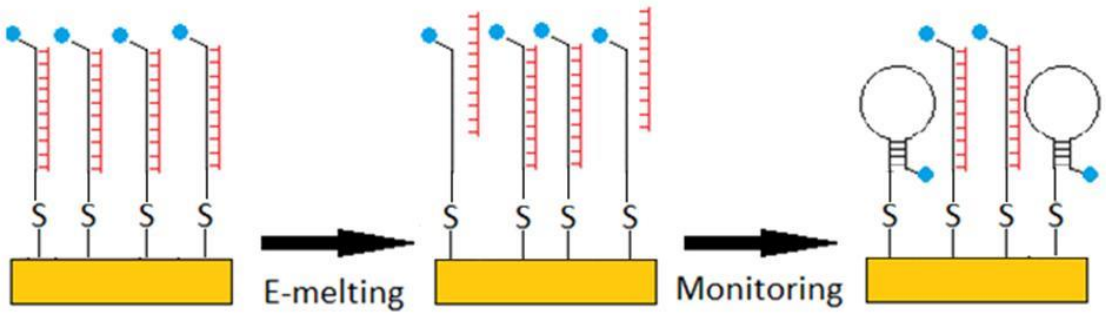

Figure 57*. Schematic of electrochemical melting of target and regeneration of hairpin.*

5.3.2. Signal Regeneration of Complimentary and Mismatch Target

For complimentary target, the % Signal Regenerated was 4 ± 1 %; while the value for 2 – Mismatch target was 20 ± 10 %. The values suggest that more of the 2-mismatch target melted off during the potential pulse, resulting in more free probe strands and a higher signal when the hairpin reforms. This value is as expected because the mismatch would cause the duplex to be thermodynamically less stable than the complimentary duplex.

5.4. Conclusion

Here we have extended our electrochemical melting approach to the detection of non-labeled DNA. This method has been applied to a label-free method the RSAD2 gene in a molecular beacon setup. The experiment has shown to detect the presence of the gene in a solution and discriminate between complimentary and mismatch strands. This preliminary data is a first step; however, further studies and optimization will need to be done for this system.

Applying a higher pulse potential or longer pulse time will result in more of the target strand to melt, resulting in a higher signal after reformation of the hairpin, and a higher % Signal Regenerated value. This will may allow us to better compare between complimentary and mismatch target. Other variables that should be optimized include, ionic strength, probe density, and probe length. Increasing the ionic strength, for instance by increasing the concentration of NaCl, will affect the rate at which the hairpin reforms due to counterion screening. It should also increase the stability of the hybridized duplex. Studies have shown that the signal and equilibrium time for linear and hairpin sensors depend on the probe density.[171,172] Increasing the duplex length may also increase the rate because the probe strand becomes more malleable; possibly forming the hairpin more readily. Work is currently underway to further optimize this method for mismatch detection and real-time monitoring of hairpin formation.

Appendix A. Comparison of Commercially Available SERS Substrates

A.1. Introduction

In this work, we compare four different types of commercially-available SERS substrates and test their compatibility with the Nicolett NXR FT-Raman Module equipped with a 1064 nm Nd:YAG laser using 4-mercaptobenzoic acid as our probe molecule. In order for a substrate to be SERS-active, it must (1) have a roughened surface that gives reproducible enhancement, (2) allow the analyte to absorb onto the surface effectively, (3) and be chemically inert with no surface photochemistry.[174] In addition to the Raman enhancement capability of each substrate, we will also test the electroactivity of the substrates to comment on their usefulness as a dual electrochemical/SERS sensor.

A.2. Raman Spectroscopy

In 1930, Sir Chandrasekhara Venkata Raman won the Nobel Prize in Physics for his theory of Raman scattering. When an incident photon collides with a molecule, an electric field induces the polarization of the molecule's electrons and produces an induced dipole. The result is a scattering of photons known as Raman scattering.[175]

The magnitude of the Raman Effect is proportional to the induced electric dipole (***p***) in a molecule, given by;[176]

$$\boldsymbol{p} = \boldsymbol{\alpha E_i} \quad \text{(Eq.23)}$$

where $\boldsymbol{\alpha}$ refers to the polarizability of the molecule's bond and $\boldsymbol{E_i}$ is the incident electromagnetic field. The incident electric field is a time-varying quantity described by;

$$\boldsymbol{E_i = E_0 cos(2\pi \upsilon_i t)} \quad \text{(Eq.24)}$$

where $\boldsymbol{E_0}$ is the amplitude of the electric field and $\boldsymbol{\upsilon_i}$ is the excitation frequency. To be Raman active, the polarizability of a bond must vary as a function of the distance between nuclei written as;

$$\boldsymbol{\alpha = \alpha_0 + \alpha_{vib} cos(2\pi \nu_{vib} t)} \quad \text{(Eq.25)}$$

where $\boldsymbol{\alpha_0}$ is the polarizability of the bond at the equilibrium position and $\boldsymbol{\upsilon_{vib}}$ is the frequency of the vibration. Manipulation of the two terms gives;

$$p = \frac{\alpha_{vib} E_0}{2} [\cos(2\pi(\nu_i + \nu_{vib})t) + \cos(2\pi(\nu_i - \nu_{vib})t)] \quad \text{(Eq.26)}$$

Raman spectroscopy reports on the vibrational states (symmetrical or asymmetrical) of molecules complimentary to IR spectroscopy except that Raman requires a change in polarization while IR requires a change in dipole moment.[177]

The energy of the incident photon excites the molecule to a virtual state. Like other electronic states, the molecule relaxes back from virtual state to the ground state. If the electron falls back to the vibrational state where it originated, then the wavelength of the scattering light is the same as the incident light, resulting in Rayleigh scattering. This phenomenon, which is the most prominent, is related to the first term in Eq. 30. The second term, relatively weak, refers to situations where the energy of the scattering light differs from that of the light source. If the scattering energy is smaller than the incident energy, then the process is called Stokes scattering. If the scattering energy is larger than the incident energy, the process is called anti-Stokes scattering.[93] Figure 58 is a representation of these different modes of light scattering.

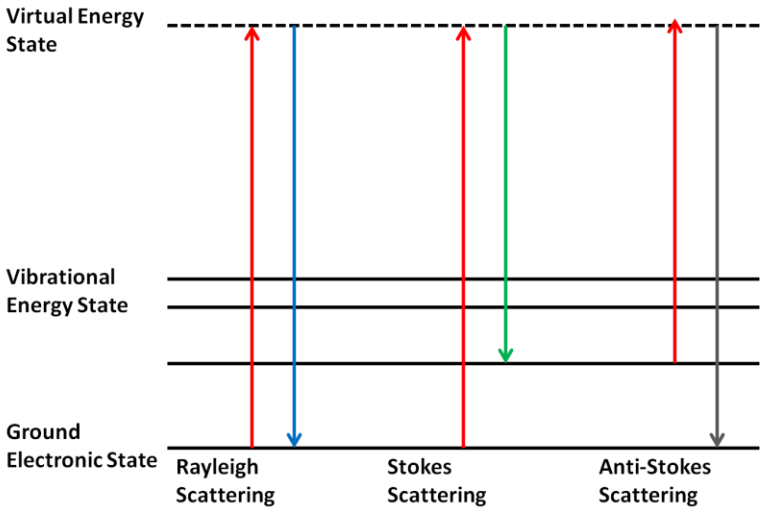

***Figure 58**. Different modes of light scattering within Raman Spectroscopy*

A.3. Surface-Enhanced Raman Spectroscopy Background

Since the effects of Raman scattering are known to be weak, a technique called Surface-Enhanced Raman Spectroscopy (SERS) was discovered and developed to enhance the signal using metallic nanostructures on surfaces. The enhancement from a SERS signal can be 10^4 - 10^5 times higher (or more) than the typical Raman signal of the same molecule and concentration.[176] The enhancement is due to both electromagnetic and chemical mechanisms. The electromagnetic enhancement is attributed to localized surface plasmons and the geometry and dielectric function of the SERS substrate. When light is incident

on the metallic nanostructures, a resonant field is induced. This occurs because the electrons in metals behave as a sea of free negative charges, or plasma, bound by stationary cations. Excitation by an electromagnetic wave at a given frequency can induce a resonant vibration of these free electrons. These vibrations are known as plasmons.[93] By exciting these localized surface plasmons in the metal, it is possible to increase the local electric field along the surface. The electrons will create an additional, localized electric field on the surface of the metallic particles. The metal essentially acts as an antenna by amplifying the incident light. The metal also amplifies any light scattering by molecules on the surface, leading to further enhancement of the signal. The chemical enhancement involves a charge transfer mechanism, whereby the excitation wavelength is resonant with the metal-molecule charge transfer electronic states.[179] First, the metal absorbs the photon and excites the surface plasmon. The energy is then transferred to the molecule, which is used to excite the molecule into an excited electronic state. The molecule then relaxes and the energy, minus a vibrational quantum, is transferred back to the metal, which in turn reradiates the new photon with the Stokes shifted frequency.[180] The large enhancement of molecule specific vibrational signatures inherent in the SERS spectrum allow extremely low detection limits and open the possibility of chemical and biological sensing using SERS. In this section, four types of solid gold SERS substrates are discussed in terms of their SERS-activity and electrochemical activity for chemical and biological sensing applications.[181]

A.4. Experimental Method

A.4.1. Preparation of 4-Mercaptobenzoic Acid on Substrates

A solution of 100 mM 4-mercaptobenzoic acid (4-MBA) was made using ethanol as the solvent. Serial dilutions yield a total of nine solutions at 100 mM, 10 mM, 1 mM, 100 μM, 10 μM, 1 μM, 100 nM, 10 nM, and 1 nM. The substrates, with exception of the Ocean Optics substrates, were mounted on a 75 by 25 by 1 mm glass slide. 10 uL of the 4-MBA solution was then dropped onto the SERS-active region of each substrate. Once dried, an FT Raman spectrum is obtained. Once completed, the next concentration above was dropped onto the substrate and scanned again until finished.

A.4.2. Raman Instrumentation

Raman spectra were acquired using a Nicolett NXR FT-Raman Module equipped with a 1064 nm Nd:YAG laser. The substrates were placed on an XYZ stage controller. The diameter of the laser spot was set to 50 μm. To avoid burning the substrates, the laser power was set to 108-250 mW, depending on the

substrate. The data collection was done with an average of 50 scans and a resolution of 8 cm^{-1}. The intensity was later corrected by normalizing the intensity by the laser power.

A.4.3. Electrochemical Measurements

Electrochemical measurements were carried out using a VersaStat 4 potentiostat with VersaStudio software (Ametek Scientific Instruments, Berwyn, PA) or a WaveNow potentiostat with AfterMath software (Pine Research, Durham, NC). A typical three-electrode cell was used, which consisted of the SERS-active substrates as a working electrode, a platinum wire auxiliary electrode (CH Instruments, Part# CHI102), and an Ag/AgCl (1M KCl) reference electrode (CH Instrument, Part# CHI111). The substrates were adhered onto aluminum strips using silver epoxy and mounted in a custom cell (Figure 59). Cyclic voltammograms were acquired using a scan rate of 50 mV/s in a solution of 5 mM potassium ferrocyanide/ferricyanide with 1 M KCl.

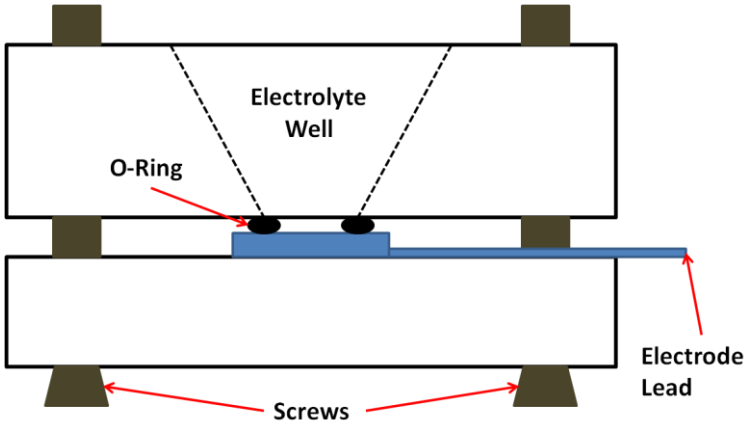

***Figure 59**. Schematic of electrochemical cell*

A.5. Results and Discussion

A.5.1. Types of SERS Substrates Used

In this work, four different commercially available SERS substrates were tested: Ocean Optics, anSERS, Q-SERS, and Silmeco. SEM images of these substrates are shown in Figure 60. The Ocean Optics (Winter Park, Florida) substrate is mixture of borosilicate glass nanofibers and gold nanoparticle on a borosilicate glass wafer. The anSERS (Laramie, Wyoming) substrate is composed of gold nanoparticles embedded in cellulose. The Q-SERS (Columbia, Missouri) substrate is a silicon wafer with gold nanoparticles deposited on the surface. Finally, the Silmeco (Copenhagen, Denmark) substrates are

silicon nanopillars with gold deposited on the tips of the pillars. As stated before, SERS enhancement is affected by the shape and nanostructure of the substrate.

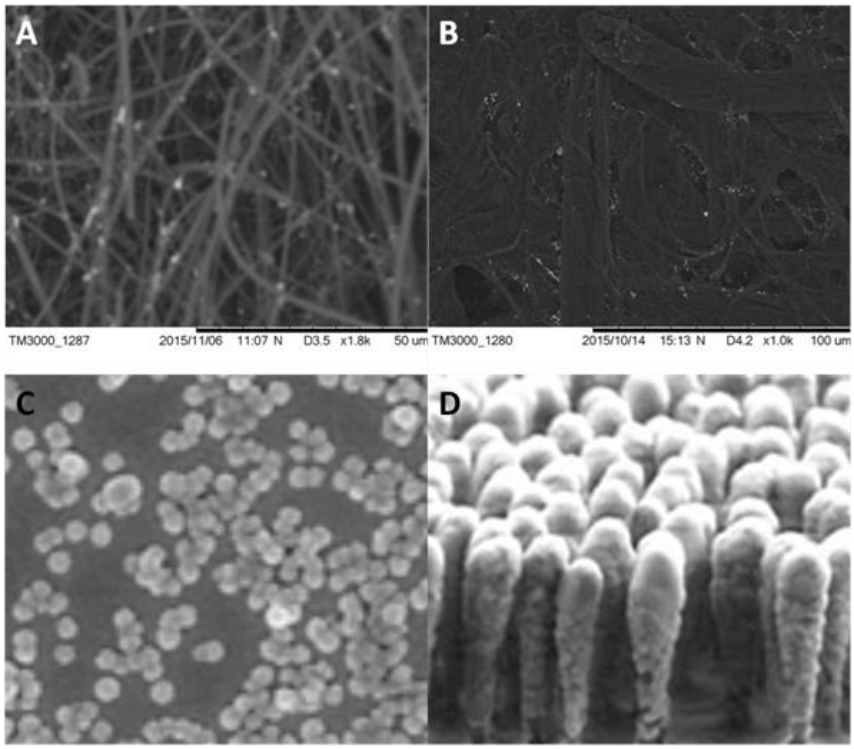

***Figure 60**. SEM images of SERS Substrates: A) Ocean Optics B) anSERS C) Q-SERS* D) Silmeco* *SEM image provided by their respective company websites*

***Table 5**. Summary of the specifications of each substrate*

	Ocean Optics	*anSERS*	*Q-SERS*	*Silmeco*
Material	AuNP in glass	AuNP in cellulose	AuNP on Si Wafer	Au on Si nanopillars
SERS Active Area	24 mm^2	9 x 5 mm	5 x 5 mm	16 mm^2
Excitation Wavelength	785 nm	785 nm	785 nm	785 nm

A.5.2. Raman Spectra of 4-mercaptobenzoic acid

4-mercaptohexanol was used as the probe molecule for SERS measurements. Figure 61 shows a Raman spectrum of 4-MBA powder. The specific peaks that will be analyzed are at 1112 cm^{-1} and 1610 $cm^{-`1}$, which are the C-COOH aromatic ring stretching and the C = O stretching vibration respectively. It is important to note that once on the substrates, these Raman peaks shift from 1112 cm^{-1} and 1610 cm^{-1} to 1070 cm^{-1} and 1583 cm^{-1}, respectively.

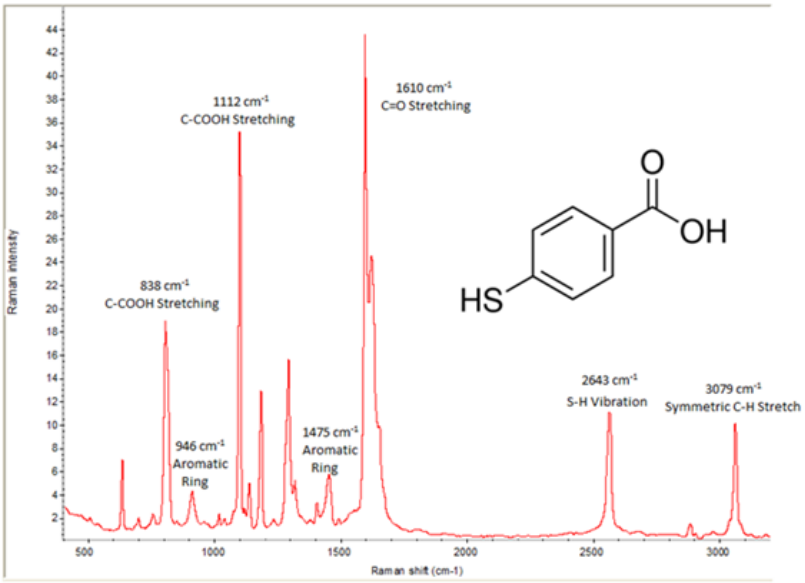

Figure 61. *FT-Raman Spectrum of 4-Mercaptobenzoic Acid (4-MBA) powder with the assigned vibrational peaks. 100 scans were averaged under a laser power of 500 mW with a spectral resolution of 8 cm^{-1}.*

A.5.3. Comparison of SERS-activity

To test if the substrates display SERS enhancement with a 1064 nm laser, Raman spectra are taken and compared to one another. Figure 62 shows the Raman spectra of each substrate at varying concentrations of 4-MBA. Each substrate has 10 µL of solution drop-cast on the active area and then left to dry. The drop volume was enough to cover the entirety of each substrate, therefore, the surface coverage of each are as followed: Ocean Optics – 23.76 mm^2, anSERS – 45 mm^2, and Silmeco – 16 mm^2. Based on the material, the laser power of the scans differed. The Ocean Optics had a laser power of 250 mW, while the anSERS and Silmeco had a laser power of 108 mW. Raman spectra of Q-SERS (data not presented) resulted in no signal; meaning that the Q-SERS substrate is not SERS active with the 1064 nm laser.

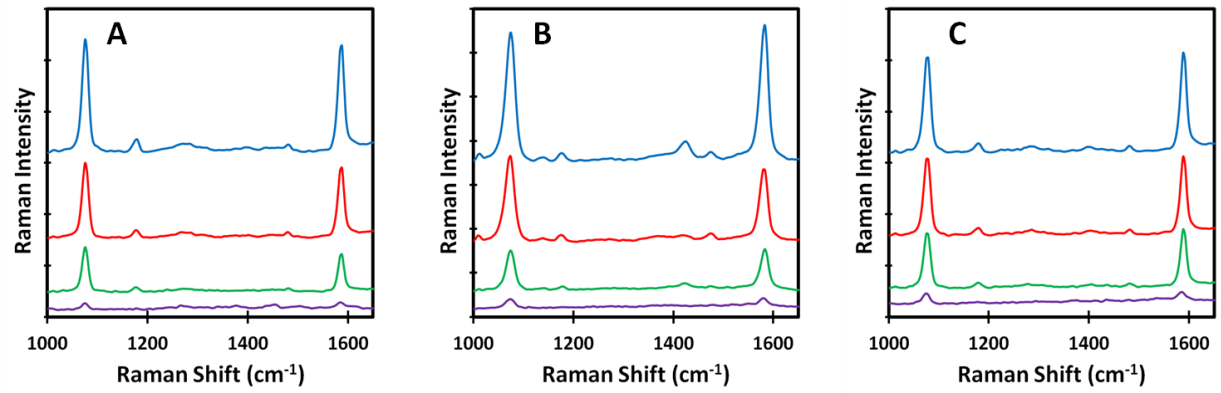

***Figure 62**. FT Raman Spectra of 4-MBA drop-cast on the Ocean Optics (**A**), anSERS (**B**), and Silmeco (**C**) substrates from 100 mM (**blue**), 10 mM (**red**), 1 mM (**green**), and 1 uM (**purple**) of 4-MBA in ethanol.*

To make the data comparable to one another, the Raman intensities and concentrations were corrected. The intensities were correcting using the OMNIC program (Thermo Fisher, Pleasanton, CA) by calculate the peak heights at 1070 cm^{-1} and 1583 cm^{-1}, then dividing by the laser power. Instead of concentration, we looked at the number of molecules scanned which is based on the area of the laser spot and the surface area of the substrate. The equation is as followed;

$$\boldsymbol{Molecules\ Measured = CVN_A \frac{Area\ of\ Laser\ Spot}{Area\ of\ Substrate}} \qquad \text{(Eq.27)}$$

where $\boldsymbol{C}$, $\boldsymbol{V}$, and $\boldsymbol{N_A}$ is the concentration (mol/L) of the drop, volume of the drop (L), and Avogadro's number (molecules/mol). The area of the laser is set to 50 µm in diameter. Figure 63 is a plot of the corrected Raman intensity with respect to the number of molecules on the three substrates. To comment of the performance of the substrates, one must look at the substrate's enhancement factor.

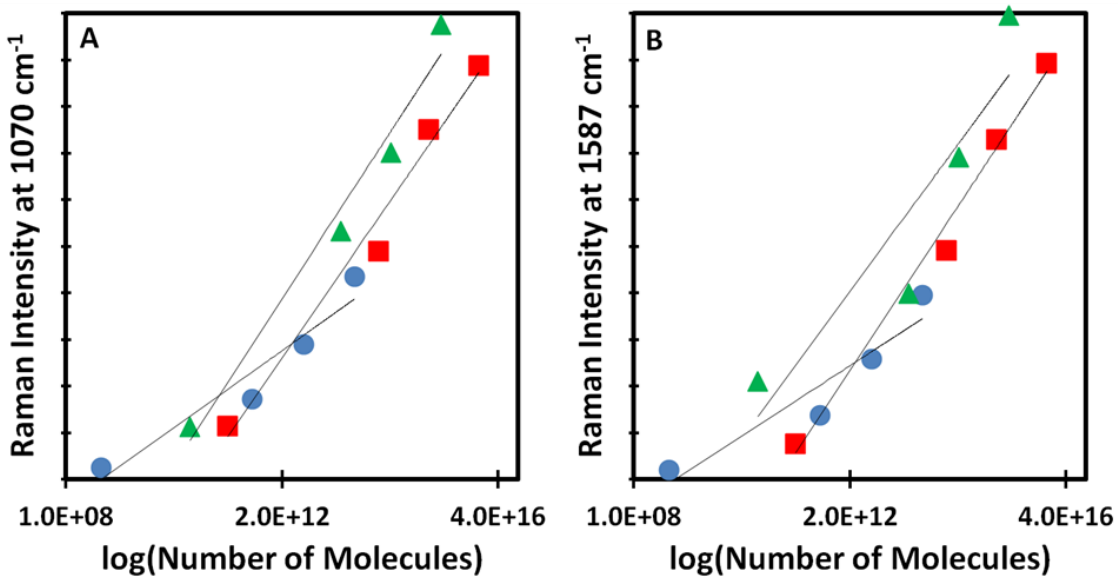

***Figure 63**. Plot of Raman intensity at 1070 (**A**) and 1587 (**B**) cm^{-1} versus the number of molecules scanned on a log scale. The substrates are Ocean Optics (**blue**, ●), anSERS (**green**, ▲) and Silmeco (**red**, ■)*

The enhancement factor (EF) is the ability of the substrate to enhance the Raman signal. Experimentally, the SERS enhancement factor is found from; [181,182]

$$\boldsymbol{EnhancementFactor} = \frac{\frac{\boldsymbol{I_{SERS}}}{\boldsymbol{N_{SERS}}}}{\frac{\boldsymbol{I_{RAMAN}}}{\boldsymbol{N_{RAMAN}}}} \quad \text{(Eq.28)}$$

where $\boldsymbol{I_{SERS}}$ and $\boldsymbol{I_{RAMAN}}$ are the intensities with and without the substrate. $\boldsymbol{N_{SERS}}$ is the number of molecules scanned on the substrate (as shown in the calculations above) and $\boldsymbol{N_{RAMAN}}$ is the number of molecules scanned in solution. Signal for the Raman signal was taken using a solution of 250 mM 4-MBA/ethanol in an NMR tube, not a flat surface. Therefore, the $\boldsymbol{N_{RAMAN}}$ was calculated using;

$$\boldsymbol{N_{RAMAN} = C * Focal\,Volume} \quad \text{(Eq.29)}$$

where the focal formula is found by visualizing the laser as a cylinder in the NMR tube. This gives the following equation;

$$\boldsymbol{Focal\,Volume = \pi * r_{Laser}^2 * L_{LaserPenetration}} \quad \text{(Eq.30)}$$

In solution, the 1070 cm^{-1} is not visible at a concentration of 250 mM; therefore, only the 1587 cm^{-1} peak will be considered for EF calculations. The maximum EF for the Ocean Optics, an SERS, and Silmeco substrates are 3.0 x 10^9, 6.0 x 10^8, and 3.0 x 10^7. Both the Ocean Optics and anSERS were orders of magnitude above the Silmeco substrate.

A.5.4. Electrochemical Activity

To test the electrochemical activity, the substrates must be electrically conducting and inert. Furthermore, there must be a practical way of connecting the substrates to the potentiostat. Due to the cellulose and borosilicate glass fibers, an electrical connection to that substrate was not possible with the Ocean Optics or anSERS substrates. Therefore, only the electrochemical activity of the Silmeco substrate was examined. Figure 64 shows the voltammograms of the Silmeco substrate compared to a polycrystalline gold electrode. The current from the gold electrode is higher due to having a higher surface area. Since the peak separation of both electrodes were ~59 mV the electrode surface of the Silmeco allow the ferric/ferrocyanide to maintain a fast, reversible reaction.

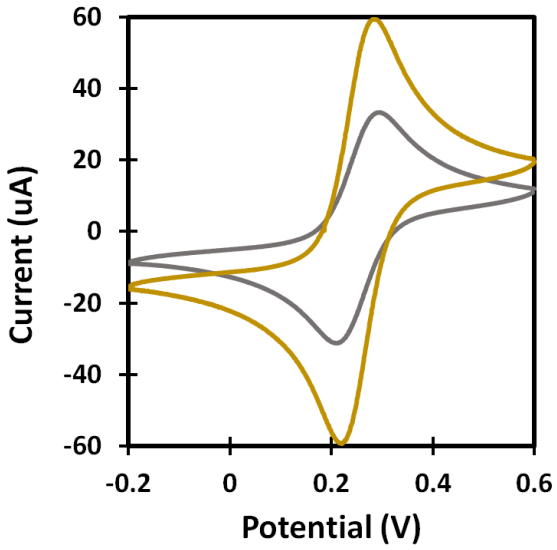

***Figure 64**. Cyclic voltammograms of polycrystalline gold electrode (**gold**) and the Silmeco substrate (**gray**). Scans were acquired in 5 mM ferric/ferrocyanide with a scan rate of 50 mV/s.*

A.6. Conclusion

The Nicolett NXR FT-Raman Module utilizes a 1064 nm laser for NIR-SERS detection of chemical and biochemical analytes. The SERS-activity of four different SERS substrates was compared and all, but the Q-SERS, was compatible with the 1064 nm laser. Furthermore, the Ocean Optics substrate had the highest maximum enhancement factor. Of the three remaining substrates, only one was found to have electrochemical compatibility - the Silmeco substrate was tested using cyclic voltammetry, producing a steady voltammogram with good peak separation and peak ratios. Although the Silmeco had the lowest enhancement factor, it was the only substrate capable of also being used as an electrode in future electrochemical-SERS studies. Further studies are underway to determine if the Silmeco substrate can be used for biological sensing, for instance DNA e-melting studies.

Appendix B: Fabrication of Gold Nanocolumns using Anodic Aluminum Oxide Wafers

B.1. Introduction

In this section a method for the fabrication of gold nanostructures using Anodic Aluminum Oxide (AAO) is presented. The fabrication combines the physical vapor deposition and electrochemical deposition of metals onto AAO substrates. Experiments are done to optimize the parameters of the physical vapor deposition and electrodeposition. Once optimized, the techniques are applied to the AAO, which act as a template to form gold nanostructures for bioelectrochemical or SERS applications. Our focus was to fabricate gold nanocolumns (AuNC Figure 68). The AuNCs are expected to increase Raman signals by creating Raman-active hotspots due to the edges and geometry of the nanocolumns. Nanocolumns provide several advantages over a planar structure, such as significantly reducing defect density due to the small area. This will reduce the strain build up from lattice and thermal expansions between the metal and growth template; thus reducing piezoelectric polarization.[183,184] The use of gold was based on previous studies of creating self-assembled monolayer of thiols and DNA to report on DNA hybridization and melting.

B.2. Physical Vapor Deposition of Aluminum on Glass

B.2.1. Background

Physical vapor deposition (PVD) is one of the oldest methods of depositing metal films. Generally, a purified, solid material is sublimated or ejected from a source (by means of resistive heating, electron beam heating, ion bombardment or laser beam bombardment) and condenses in a vacuum to the substrate surface producing a thin film.[185] PVD systems are comprised of a vacuum chamber with associated pumps, and evaporation sources and their controlling electronics. One advantage of utilizing a vacuum system is that the number of molecules in a gas deposited is directly related to pressure in a given volume as shown by the ideal gas equation,

$$\boldsymbol{PV = Nk_bT} \qquad \text{(Eq.31)}$$

where $\boldsymbol{P}$ is pressure, $\boldsymbol{V}$ is volume, $\boldsymbol{N}$ is the number of molecules, $\boldsymbol{k_b}$ is Boltzmann's constant and $\boldsymbol{T}$ is the gas absolute temperature. Therefore, at lower pressures, there are directly fewer molecules. Another advantage is that under vacuum, the material atoms have a longer mean free path, which represents the average distance an atom travels before colliding with another atom. Thus, the metal atoms are less likely to collide with each other on the way to the substrate. The mean free path can be determined using the kinetic theory of gases in the following equation,

$$\lambda = \frac{V}{\sqrt{2}N\sigma} = \frac{k_b T}{\sqrt{2}\sigma P} \quad \text{(Eq.32)}$$

where λ is the mean free path of an atom and σ is the interaction cross section, which represents the likelihood of interaction between particles.[185]

Figure 65A depicts the typical set up of a PVD chamber. For PVD, evaporation is possible under low pressure conditions which are attained using a two-vacuum pump system consisting of a rotary vane pump (RVP) and a turbo pump. The RVP is an oil-sealed displacement pump. The rotor vane system moves eccentrically and divides the chamber into two sections. The gas flows through the inlet as the rotor spins and is then sealed off by the vanes. The gas enclosed in the chamber is then compressed and goes through the outlet. The second pump in the system is a turbo pump. This pump has a stator and rotor with several stages of blades that simply transfer the momentum of the vapor driving it towards lower stages. A turbo pump cannot operate at near atmospheric pressure. The purpose of the RVP is to reduce pressure in the vacuum chamber, bringing the pressure down to about 1 mTorr. The turbo pump also cannot exhaust at near atmospheric pressures. Therefore, the RVP has a "rough" valve connecting to the chamber and a "foreline" valve connecting to the turbo pump. The RVP is then able to provide an appropriate backing pressure. Once the chamber and the foreline valve are at an appropriate pressure, the turbo pump can then be used to pump down the chamber to 10^{-4} Torr. If the vacuum system is not set up correctly, the turbo pump can be severely damaged and the chamber would not be at an appropriate pressure for physical vapor deposition.

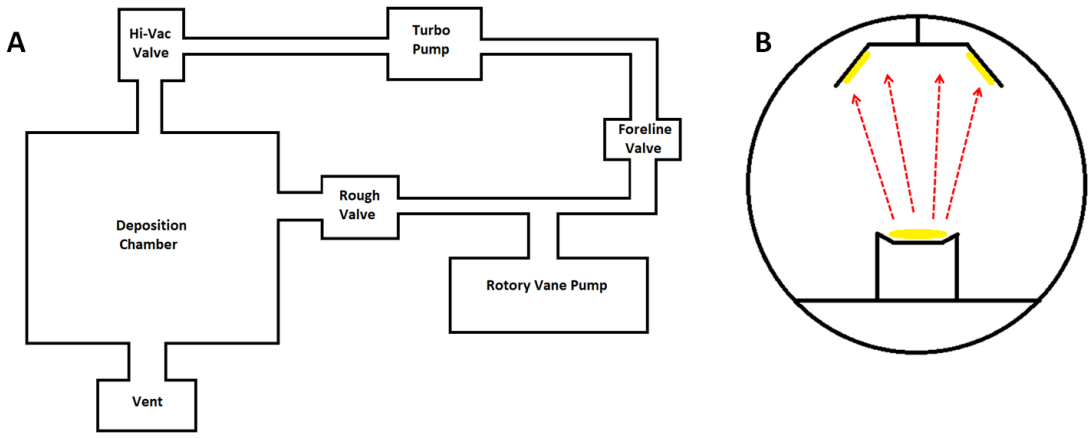

***Figure 65**. A) Schematic of vacuum lines connecting to the PVD chamber. B) Inside a PVD where a metal is vaporized onto substrates above.*

Once the chamber is at the correct pressure, the evaporation process can begin. Inside the chamber (Figure 65B), the material is placed on vessel (typically a tungsten coil or basket) and then

evaporated using resistive heating which utilizes a large electric current through the vessel to evaporate the material. The mass deposition rate per unit of the surface may be approximated using the Langmuir-Knudsen equation, given by,

$$R_m = C_m \sqrt{\frac{M}{T}} \cos\theta \sin\phi \frac{1}{r^2} (P_e(T) - P) \quad \text{(Eq.33)}$$

where R_m is the mass deposition rate, C_m is a constant (1.85×10^{-2} $^{\text{mol K}}/_{\text{s Torr}}$) M is the gram-molecular mass of the material, T is the temperature of the material, θ is the angle between the normal of the source and the substrate, ϕ is the angle normal to the surface of the substrate and the source, r is the distance between the substrate and the source, P is the pressure of the chamber, and P_e is the vapor pressure of the material. Once the material vaporizes, the gaseous metal then flows towards the substrate where it sublimates. The vapor pressure is strongly dependent on the temperature of the chamber, which affects the efficiency of the metal depositing on the wafer. Furthermore, vacuum deposition, used in this work, may provide poor uniformity and waste of material. However, the ease of PVD to form standard surface coverage of metal is the reason why it is used here.[186]

B.2.2. Experimental Method

Aluminum strips (Reynolds Kitchen, Lake Forest Illinois) were cut and varied by mass. The PVD set up consists of a chamber (Electro-Mechanical Services Inc., Albuquerque, New Mexico), a turbo pump (model: ENDISOK63N5NOVEP, Vacuum Research Corporation, Pittsburg, Pennsylvania), and roughing pump (model: 100-3.5, VRC, Pittsburgh, Pennsylvania). The aluminum is wrapped around a tungsten coil (4" x 1 ¾" – ¼", Ted Pella Inc., Redding, California) and is then set to a temperature high enough to deposited on glass slides. This chamber has no thermometer probe, so vaporization temperature is unknown. After each deposition, the step height of aluminum is measured using a profilometer (Sitek Process Solutions Inc, Rocklin, California).

B.2.3. Results and Discussion

Figure 66 compares the mass of aluminum used in the deposition to the step height of the aluminum deposited on the glass. The chamber has a hanging carousel with four arms to attach the glass slides. Interestingly, the location of the arms effects the amount of aluminum deposited on the glass. The strips of aluminum were cut rectangular to wrap around the coil, so this uneven deposition is a result of the position of the slides with respect to the rectangular foil. The results of this experiment will prove useful as aluminum is an inexpensive metal that can be used to deposit on the back of substrates to make them sturdier.

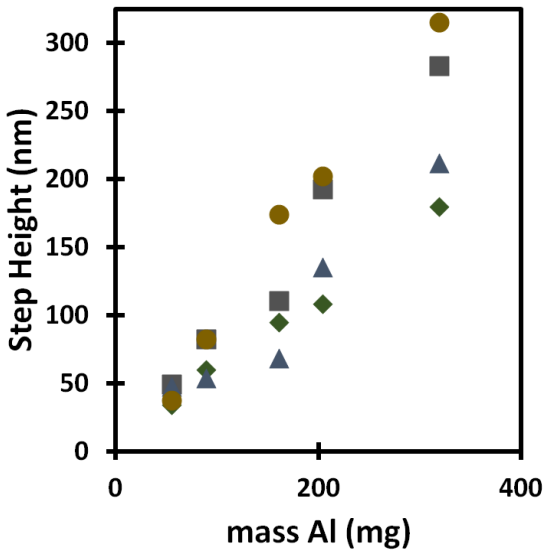

Figure 66*. Plot of step height because of the amount of aluminum deposited in the PVD chamber. The different shapes represent the positions of the glass slides in the chamber. Data clustered together are a result of the glass slides being on opposite sides of each other.*

B.3. Gold Electrodeposition

B.3.1. Background

The process of electrochemically depositing gold is dated back to 1803 with Professor Luigi Brugnatelli. Brugnatelli's solution consisting of one part of the saturated solution of gold in nitromuriatic acid, six parts of solution of ammonia in which the solution will decompose forming oxides of gold as well as ammoniurets of gold. Nowadays, gold electrodeposition solutions come in many different varieties such as cyanide and sulfite-based solutions. The use for this technique ranges from jewelry and dentistry to microelectronics.[187] Through an electrochemical reduction process, the ions deposit on the electrode surface and form structures of varying morphology. The morphology can be adjusted by varying parameters of the electrodeposition process, such as time, bath concentration, and applied current or potential.[188] Furthermore, careful control of these parameters allows for maximum surface area and resolution of nanostructures.

Consider the general electrodeposition mechanism;

$$3Au(SO_3)_2^{3-} \leftrightarrow 2Au + Au(SO_3)_4^{5-} + 2SO_3^{2-} \qquad \text{(Rxn.9)}$$

the positive gold ions are freely moving in the solution. The negatively charged working electrode draws the gold ions into the electrical double layer. An electron transfer reaction occurs where the gold ions gain electrons from the working electrode. This reduction reaction then forms neutral atomic gold on the surface of the electrode.

Aside from the electrochemical technique, another important aspect of electrodeposition is the solution. For gold, a cyanide-based solution is common. The solution that used in this thesis is sulfite-based which is less stable and efficient than cyanide. However, the stability of the cyanide complex causes the reduction potential to occur at very negative potentials, resulting in co-reduction causing hydrogen evolution.[188] Furthermore, the release of free cyanide is incompatible with compounds, such as photoresist, and is a health hazard.

B.3.2. Experimental Method

Gold deposition solution (Elevate ® Gold 7990) was purchased from Technic Inc (San Jose, CA). Gold working electrodes were fabricated using physical vapor deposition on chromium from NIST. Electrochemical measurements were carried out using a VersaStat 4 potentiostat with VersaStudio software (Ametek Scientific Instruments, Berwyn, PA). The substrate was placed in a custom electrochemical cell (Figure 59) with the electrodeposition solution, a platinum wire auxiliary electrode (CH Instruments, Part# CHI102), and an Ag/AgCl (1M KCl) reference electrode (CH Instrument, Part# CHI111).

Gold was electrochemically deposited using a constant potential -0.58 V (vs Ag/AgCl), at this potential, the current is within the lower and upper limits of the charge density. The constants potential was ran at varying times which was dependent on the final charge of the experiment. The step height of the gold deposited was calculated using a profilometer (catalog: 030889, Sitek Process Solutions Inc, Rocklin, California).

B.3.3. Results and Discussion

A calibration plot (Figure 67A) to relate the final charge of each deposition to the step height of the gold deposited onto the gold electrode. At -1.05, -5.23, -5.96, and -13.2 mC, the amount of gold deposited was 56 ± 4, 270 ± 13, 300 ± 10, and 689 ± 8 nm. The substrates were further characterized by examining the electrochemical activity of the surface. A liner sweep voltammogram was acquired of the substrate in 2.5 mM ferri/ferrocyanide at 50 mV/s (Figure 67B). Although the surface area of the substrate is smaller than the polycrystalline electrode, the peak potential of the substrate is shifted more negatively, and the peak current is higher. This suggests that the electrode area may be rough and not in the best condition. To confirm, the roughness factor of the substrate was calculated by taking by dividing the electrode surface area (calculated using the Randles-Sevcik equation) by the geometric area (0.0079 cm^2). The RF of our substrate was ~0.7. So, the electrode needs to be electrochemically polished after the deposition. Combining the techniques from the PVD and gold deposition experiments will be essential to create the AuNCs.

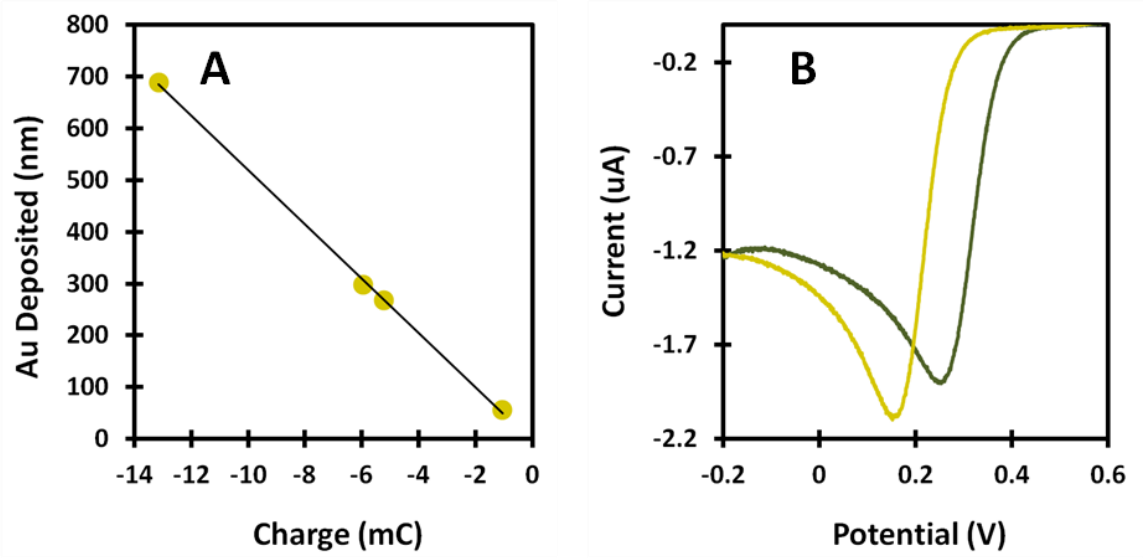

***Figure 67**. A) Step height of gold deposited with respect to the final charge of the chronoamperometric experiment. B) linear scan voltammograms of a polycrystalline gold electrode (**green**) and the substrate (**yellow**)*

B.4. Fabrication of Au Nanocolumns (AuNC)

B.4.1. Experimental Method

Whatman ® anodic aluminum oxide (AAO) wafers were purchased from Sigma Aldrich. Gold deposition solution and PVD set-up were the same as mentioned above. Figure 68 depicts the general scheme of fabricating the AuNCs. AAO were mounted on glass slides so that the back of AAO would be deposited on. Using a tungsten basket (Product: 84-22, Ted Pella Inc), a 99.99% pure gold pellet (Kurt J. Lesker, Jefferson Hills, Pennsylvania) was deposited onto the back of the AAO substrate. The substrate was then annealed at 120 ^{0}C to ensure a smooth gold layer. The substrate was placed back into the PVD chamber and 300 mg of aluminum was deposited to strengthen the backing of the substrate.

Afterward, the Al/Au/AAO substrate is placed in the electrochemical cell with the same set up as previously stated. A constant potential was used at -0.58 V (vs Ag/AgCl) to a final charge of -6 mC to form the AuNC. The AAO is then dissolved in 3 M NaOH leaving behind the AuNCs.

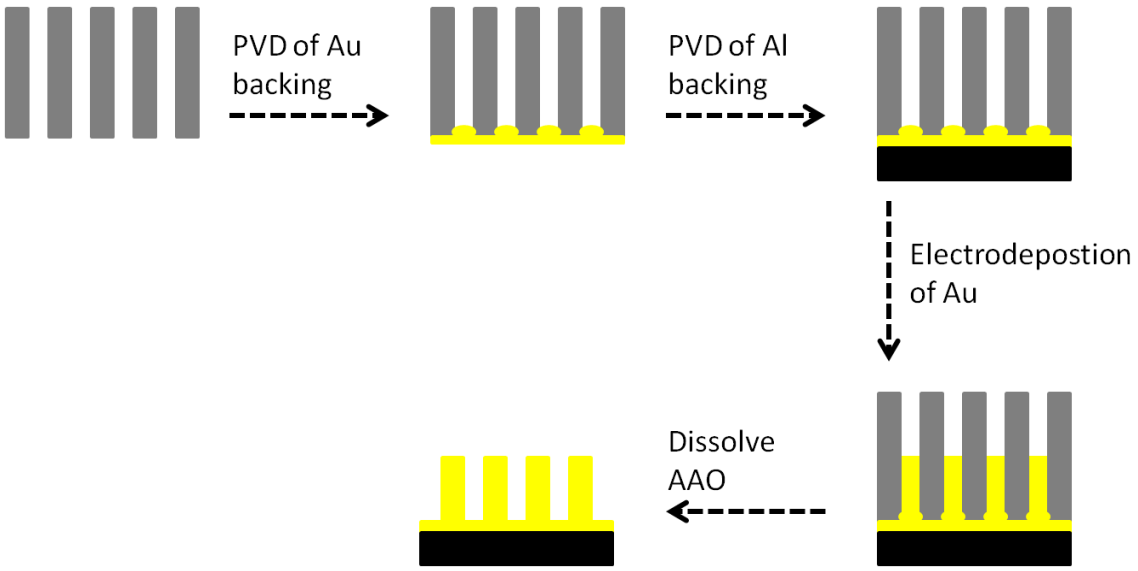

***Figure 68**. Schematic for the fabrication of AuNCs*

B.4.2. Results and Discussion

SEM images were taken of the AAO throughout the entire deposition process. Figure 69A, is the Au backing of the AAO before the annealing and Al. After annealing, the surface seemed much smoother (SEM not presented). Figure 69B is the front side of the Au/AAO substrate. This image shows that many of the pores are still open for gold to be electrochemically deposited. Finally, Figure 69C is the AuNC substrate after dissolving the AAO in 3 M NaOH. On the surface, there may be residual salt or NaOH from the experiment. However, below that are the AuNCs that we wanted to fabricate.

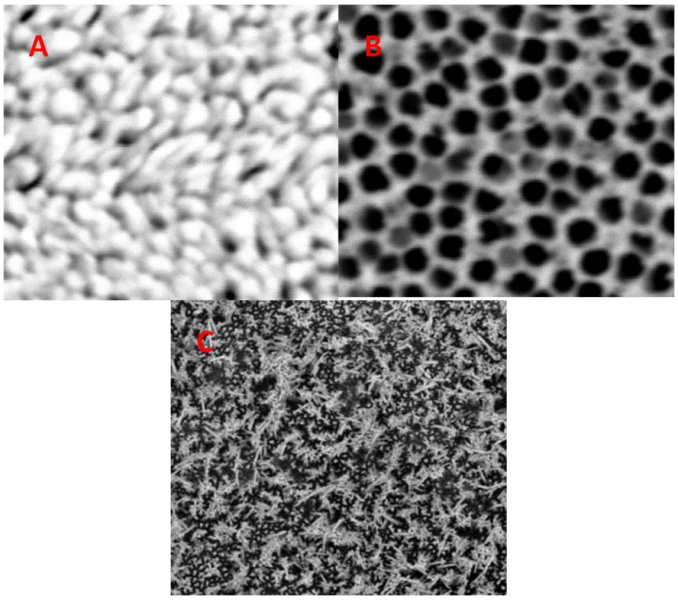

***Figure 69**. SEM images of the substrate after the PVD of the (A) gold backing, (B) the front of that same substrate, and (C) after the AuNCs have formed*

B.5. Conclusion

Although the rinsing process knocked over some of the columns, as a proof concept, we were able to fabricate our AuNCs. For future experiments, the amount of the backing and the columns would need to be optimized to a height where they are sturdy enough to withstand environmental conditions. Further studies are underway for the fabrication of more robust substrates. Once complete, these substrates will be tested for their electrochemical and optical activity.

References

1. Bard AJ, Faulkner LR. *Electrochemical methods: Fundamentals and applications.* New York: Wiley; 2001.
2. Fernie AR, Carrari F, Sweetlove LJ. Respiratory metabolism: Glycolysis, the TCA cycle and mitochondrial electron transport. *Curr Opin Plant Biol*. 2004;7(3):254-261.
3. Robertson AD, West AR, Ritchie AG. Review of crystalline lithium-ion conductors suitable for high temperature battery applications. *Solid State Ionics*. 1997;104(1):1-11.
4. Janata J. *Principles of chemical sensors.* Springer Science & Business Media; 2010.
5. Niu L, Li Q, Wei F, Chen X, Wang H. Formation optimization of platinum-modified polyaniline films for the electrocatalytic oxidation of methanol. *Synth Met*. 2003;139(2):271-276.
6. Cai H, Wang Y, He P, Fang Y. Electrochemical detection of DNA hybridization based on silver-enhanced gold nanoparticle label. *Analytica Chimica Acta*. 2002;469(2):165-172. http://www.sciencedirect.com/science/article/pii/S0003267002006700. doi: 10.1016/S0003-2670(02)00670-0.
7. Kai E, Sawata S, Ikebukuro K, Iida T, Honda T, Karube I. Detection of PCR products in solution using surface plasmon resonance. *Anal Chem*. 1999;71(4):796-800.
8. Kamat A, Huth A, Klein O, Scholl S. Chronoamperometric investigations of the electrode–electrolyte interface of a commercial high temperature PEM fuel cell. *Fuel Cells*. 2010;10(6):983-992.
9. Steel AB, Herne TM, Tarlov MJ. Electrochemical quantitation of DNA immobilized on gold. *Anal Chem*. 1998;70(22):4670-4677.
10. Kissinger PT, Heineman WR. Cyclic voltammetry. *J Chem Educ*. 1983;60(9):702.
11. Mabbott GA. An introduction to cyclic voltammetry. *J Chem Educ*. 1983;60(9):697.
12. Cherevko S, Topalov AA, Zeradjanin AR, Katsounaros I, Mayrhofer KJ. Gold dissolution: Towards understanding of noble metal corrosion. *Rsc Advances*. 2013;3(37):16516-16527.
13. Krause MS, Ramaley L. Analytical application of square wave voltammetry. *Analytical Chemistry*. 1969;41(11):1365-1369. doi: 10.1021/ac60280a008.
14. Dogan-Topal B, Ozkan SA, Uslu B. The analytical applications of square wave voltammetry on pharmaceutical analysis. *The Open Chemical and Biomedical Methods Journal*. 2010;3:56-73.
15. Špaček J, Daňhel A, Hasoň S, Fojta M. Label-free detection of canonical DNA bases, uracil and 5-methylcytosine in DNA oligonucleotides using linear sweep voltammetry at a pyrolytic graphite electrode. *Electrochemistry Communications*. 2017;82:34-38.
16. Chen A, Shah B. Electrochemical sensing and biosensing based on square wave voltammetry. *Analytical Methods*. 2013;5(9):2158-2173.
17. Ussery DW. DNA structure: A-, B- and Z-DNA helix families. In: *Encyclopedia of life sciences.* Macmillan Publishers Ltd, Nature Publishing Group; 2002. http://onlinelibrary.wiley.com/doi/10.1038/npg.els.0003122/abstract. Accessed Jan 27, 2018.
18. Williams AA, Darwanto A, Theruvathu JA, Burdzy A, Neidigh JW, Sowers LC. The impact of sugar pucker on base pair and mispair stability. *Biochemistry*. 2009;48(50):11994. Accessed Jan 27, 2018. doi: 10.1021/bi9014133.
19. Huang M, Giese TJ, Lee T, York DM. Improvement of DNA and RNA sugar pucker profiles from semiempirical quantum methods. *Journal of chemical theory and computation*. 2014;10(4):1538-1545.
20. Svoboda P, Cara AD. Hairpin RNA: A secondary structure of primary importance. *Cellular and Molecular Life Sciences CMLS*. 2006;63(7-8):901-908.
21. Staple DW, Butcher SE. Pseudoknots: RNA structures with diverse functions. *PLoS biology*. 2005;3(6):e213.
22. Potaman VN, Sinden RR. DNA: Alternative conformations and biology. https://www.ncbi.nlm.nih.gov/books/NBK6545/. Updated 2013. Accessed Jan 22, 2018.

23. Ivanov VI, Krylov DY. [6] A-DNA in solution as studied by diverse approaches. *Meth Enzymol*. 1992;211:111-127.
24. Herbert A, Rich A. Left-handed Z-DNA: Structure and function. *Genetica*. 1999;106(1-2):37-47. Accessed Jan 27, 2018. doi: 1003768526018.
25. Berg JM, Tymoczko JL, Stryer L. *Biochemistry.* 5th ed. New York: W H Freeman; 2002:11-21. https://www.ncbi.nlm.nih.gov/books/NBK22585/. Accessed Jan 27, 2018.
26. Brazda V, Laister RC, Jagelska EB, Arrowsmith C. Cruciform structures are a common DNA feature important for regulating biological processes. *BMC molecular biology*. 2011;12(1):33.
27. Mikheikin AL, Lushnikov AY, Lyubchenko YL. Effect of DNA supercoiling on the geometry of holliday junctions. *Biochemistry (N Y)*. 2006;45(43):12998-13006.
28. Eun H. *Enzymology primer for recombinant DNA technology.* Elsevier; 1996.
29. Jain A, Wang G, Vasquez KM. DNA triple helices: Biological consequences and therapeutic potential. *Biochimie*. 2008;90(8):1117-1130.
30. Cooney M, Czernuszewicz G, Postel EH, Flint SJ, Hogan ME. Site-specific oligonucleotide binding represses transcription of the human c-myc gene in vitro. *Science*. 1988;241(4864):456-459.
31. Wu Q, Gaddis SS, MacLeod MC, et al. High-affinity triplex-forming oligonucleotide target sequences in mammalian genomes. *Mol Carcinog*. 2007;46(1):15-23.
32. Christensen LA, Finch RA, Booker AJ, Vasquez KM. Targeting oncogenes to improve breast cancer chemotherapy. *Cancer Res*. 2006;66(8):4089-4094.
33. Lipps HJ, Rhodes D. G-quadruplex structures: In vivo evidence and function. *Trends Cell Biol*. 2009;19(8):414-422.
34. Bochman ML, Paeschke K, Zakian VA. DNA secondary structures: Stability and function of G-quadruplex structures. *Nature Reviews Genetics*. 2012;13(11):770.
35. Belmont A, Nicolini C. Polyelectrolyte theory and chromatin-DNA quaternary structure: Role of ionic strength and hl histone. *J Theor Biol*. 1981;90(2):169-179.
36. Bartke T, Vermeulen M, Xhemalce B, Robson SC, Mann M, Kouzarides T. Nucleosome-interacting proteins regulated by DNA and histone methylation. *Cell*. 2010;143(3):470-484.
37. Ririe KM, Rasmussen RP, Wittwer CT. Product differentiation by analysis of DNA melting curves during the polymerase chain reaction. *Anal Biochem*. 1997;245(2):154-160.
38. Rusling JF. *Biomolecular films: Design, function, and applications.* CRC Press; 2003.
39. Schildkraut C, Lifson S. Dependence of the melting temperature of DNA on salt concentration. *Biopolymers*. 1965;3(2):195-208.
40. PCR basics. https://www.thermofisher.com/us/en/home/life-science/cloning/cloning-learning-center/invitrogen-school-of-molecular-biology/pcr-education/pcr-reagents-enzymes/pcr-basics.html. Accessed Apr 3, 2018.
41. What is PCR (polymerase chain reaction)? /facts/what-is-pcr-polymerase-chain-reaction. Accessed Jul 23, 2018.
42. Neidler S. What are the differences between PCR, RT-PCR, qPCR, and RT-qPCR? http://www.enzolifesciences.com/science-center/technotes/2017/march/what-are-the-differences-between-pcr-rt-pcr-qpcr-and-rt-qpcr?. Accessed Apr 3, 2018.
43. Mannucci A, Sullivan KM, Ivanov PL, Gill P. Forensic application of a rapid and quantitative DNA sex test by amplification of the XY homologous gene amelogenin. *Int J Legal Med*. 1994;106(4):190-193.
44. Nicklas JA, Buel E. Development of an alu-based, real-time PCR method for quantitation of human DNA in forensic samples. *J Forensic Sci*. 2003;48(5):936-944.
45. Lee SB, McCord B, Buel E. Advances in forensic DNA quantification: A review. *Electrophoresis*. 2014;35(21-22):3044-3052.
46. Introduction to PCR primer & probe chemistries. http://www.bio-rad.com/en-us/applications-technologies/introduction-pcr-primer-probe-chemistries?ID=LUSOJW3Q3. Accessed Apr 3, 2018.
47. Wittwer CT. High-resolution DNA melting analysis: Advancements and limitations. *Hum Mutat*. 2009;30(6):857-859.

48. A guide to high resolution melting (HRM) analysis. *Life Technologies, Applied Biosystems*. 2009:1-20.
49. Gelaye E, Mach L, Kolodziejek J, et al. A novel HRM assay for the simultaneous detection and differentiation of eight poxviruses of medical and veterinary importance. *Scientific reports*. 2017;7:42892.
50. Gelaye E, Mach L, Kolodziejek J, et al. A novel HRM assay for the simultaneous detection and differentiation of eight poxviruses of medical and veterinary importance. *Scientific reports*. 2017;7:42892.
51. Malapelle U, Carlomagno C, Salatiello M, et al. KRAS mutation detection by high-resolution melting analysis significantly predicts clinical benefit of cetuximab in metastatic colorectal cancer. *Br J Cancer*. 2012;107(4):626.
52. Franca LT, Carrilho E, Kist TB. A review of DNA sequencing techniques. *Q Rev Biophys*. 2002;35(2):169-200.
53. Ansorge WJ. Next-generation DNA sequencing techniques. *New biotechnology*. 2009;25(4):195-203.
54. Yu L, Lim H, Maslova A, Hsing I. Rational design of electrochemical DNA biosensors for Point-of-Care applications. *ChemElectroChem*. 2017.
55. Arrigan D, Kranz C, Lee HJ. Electrochemical biosensing: From the bench to the real world. *ChemElectroChem*. 2017;4(4):751-752.
56. Campuzano S, Yanez-Sedeno P, Pingarron JM. Electrochemical biosensing approaches for diagnosis of viral infections and tropical diseases. *ChemElectroChem*. 2017.
57. Paleček E. Oscillographic polarography of highly polymerized deoxyribonucleic acid. *Nature*. 1960;188(4751):656-657.
58. Fojta M, Vetterl V, Tomschik M, et al. Adsorption of peptide nucleic acid and DNA decamers at electrically charged surfaces. *Biophys J*. 1997;72(5):2285-2293.
59. Paleček E. Determination of pseudouridine at submicromolar concentrations by cathodic stripping voltammetry at a mercury electrode. *Anal Chim Acta*. 1985;174:103-113.
60. Pedano ML, Rivas GA. Immobilization of DNA on glassy carbon electrodes for the development of affinity biosensors. *Biosensors and Bioelectronics*. 2003;18(2):269-277.
61. Erdem A, Kerman K, Meric B, Akarca US, Ozsoz M. DNA electrochemical biosensor for the detection of short DNA sequences related to the hepatitis B virus. *Electroanalysis*. 1999;11(8):586-587.
62. Erdem A, Kerman K, Meric B, Ozsoz M. Methylene blue as a novel electrochemical hybridization indicator. *Electroanalysis*. 2001;13(3):219-223.
63. Paleček E. Adsorptive transfer stripping voltammetry: Determination of nanogram quantities of DNA immobilized at the electrode surface. *Anal Biochem*. 1988;170(2):421-431.
64. Sashiwa H, Aiba S. Chemically modified chitin and chitosan as biomaterials. *Progress in Polymer Science*. 2004;29(9):887-908.
65. Alwarappan S, Cissell K, Dixit S, Li C, Mohapatra S. Chitosan-modified graphene electrodes for DNA mutation analysis. *Journal of Electroanalytical Chemistry*. 2012;686:69-72. doi: 10.1016/j.jelechem.2012.09.026.
66. Zhou XC, Huang LQ, Li SFY. Microgravimetric DNA sensor based on quartz crystal microbalance: Comparison of oligonucleotide immobilization methods and the application in genetic diagnosis. *Biosensors and Bioelectronics*. 2001;16(1):85-95. http://www.sciencedirect.com/science/article/pii/S0956566300001366. doi: 10.1016/S0956-5663(00)00136-6.
67. Wang F, Xu Y, Wang L, Lu K, Ye B. Immobilization of DNA on a glassy carbon electrode based on Langmuir–Blodgett technique: Application to the detection of epinephrine. *Journal of Solid State Electrochemistry*. 2012;16(6):2127-2133.
68. Hashimoto K, Ito K, Ishimori Y. Novel DNA sensor for electrochemical gene detection. *Analytica Chimica Acta*. 1994;286(2):219-224.

http://www.sciencedirect.com/science/article/pii/0003267094801630. doi: 10.1016/0003-2670(94)80163-0.
69. Lucarelli F, Marrazza G, Turner APF, Mascini M. Carbon and gold electrodes as electrochemical transducers for DNA hybridisation sensors. *Biosensors and Bioelectronics*. 2004;19(6):515-530. http://www.sciencedirect.com/science/article/pii/S0956566303002562. doi: 10.1016/S0956-5663(03)00256-2.
70. Liu X, Tan W. A fiber-optic evanescent wave DNA biosensor based on novel molecular beacons. *Anal Chem*. 1999;71(22):5054-5059.
71. Wilchek M, Bayer EA, Livnah O. Essentials of biorecognition: The (strept) avidin–biotin system as a model for protein–protein and protein–ligand interaction. *Immunol Lett*. 2006;103(1):27-32.
72. Christiaens P, Vermeeren V, Wenmackers S, et al. EDC-mediated DNA attachment to nanocrystalline CVD diamond films. *Biosensors and Bioelectronics*. 2006;22(2):170-177.
73. Millan KM, Saraullo A, Mikkelsen SR. Voltammetric DNA biosensor for cystic fibrosis based on a modified carbon paste electrode. *Anal Chem*. 1994;66(18):2943-2948.
74. Wang SG, Wang R, Sellin PJ, Zhang Q. DNA biosensors based on self-assembled carbon nanotubes. *Biochem Biophys Res Commun*. 2004;325(4):1433-1437.
75. Liang L, Liu J, Windisch CF, Exarhos GJ, Lin Y. Direct assembly of large arrays of oriented conducting polymer nanowires. *Angewandte Chemie International Edition, 41(19):3665-3668*. 2002. http://www.osti.gov/scitech/biblio/15002653. doi: AID-ANIE3665>3.0.CO;2-B.
76. Bo Y, Yang H, Hu Y, Yao T, Huang S. A novel electrochemical DNA biosensor based on graphene and polyaniline nanowires. *Electrochimica Acta*. 2011;56(6):2676-2681. http://www.sciencedirect.com/science/article/pii/S0013468610016671. doi: 10.1016/j.electacta.2010.12.034.
77. Chang H, Yuan Y, Shi N, Guan Y. Electrochemical DNA biosensor based on conducting polyaniline nanotube array. *Anal Chem*. 2007;79(13):5111-5115.
78. Nuzzo RG, Allara DL. Adsorption of bifunctional organic disulfides on gold surfaces. *J Am Chem Soc*. 1983;105(13):4481-4483.
79. Häussling L, Michel B, Ringsdorf H, Rohrer H. Direct observation of streptavidin specifically adsorbed on biotin-functionalized self-assembled monolayers with the scanning tunneling microscope. *Angewandte Chemie International Edition*. 1991;30(5):569-572.
80. Hegner M, Wagner P, Semenza G. Immobilizing DNA on gold via thiol modification for atomic force microscopy imaging in buffer solutions. *FEBS Lett*. 1993;336(3):452-456.
81. Herne TM, Tarlov MJ. Characterization of DNA probes immobilized on gold surfaces. *J Am Chem Soc*. 1997;119(38):8916-8920.
82. Love JC, Estroff LA, Kriebel JK, Nuzzo RG, Whitesides GM. Self-assembled monolayers of thiolates on metals as a form of nanotechnology. *Chem Rev*. 2005;105(4):1103-1170.
83. Nuzzo RG, Zegarski BR, Dubois LH. Fundamental studies of the chemisorption of organosulfur compounds on gold (111). implications for molecular self-assembly on gold surfaces. *J Am Chem Soc*. 1987;109(3):733-740.
84. Ulman A. Formation and structure of self-assembled monolayers. *Chem Rev*. 1996;96(4):1533-1554.
85. Widrig CA, Chung C, Porter MD. The electrochemical desorption of n-alkanethiol monolayers from polycrystalline au and ag electrodes. *Journal of electroanalytical chemistry and interfacial electrochemistry*. 1991;310(1-2):335-359.
86. Mehnaaz F Ali, Romy Kirby, Adrian P Goodey, Marc D Rodriguez. DNA hybridization and discrimination of single-nucleotide mismatches using chip-based microbead arrays. *Analytical Chemistry*. 2003;75(18):4732-4739. http://www.ncbi.nlm.nih.gov/pubmed/14674448. doi: 10.1021/ac034106z.
87. Tyagi S, Kramer FR. Molecular beacons: Probes that fluoresce upon hybridization. *Nat Biotechnol*. 1996;14(3):303-308.
88. Marras SA, Tyagi S, Kramer FR. Real-time assays with molecular beacons and other fluorescent nucleic acid hybridization probes. *Clinica Chimica Acta*. 2006;363(1):48-60.

89. Wang H, Li J, Liu H, et al. Label-free hybridization detection of a single nucleotide mismatch by immobilization of molecular beacons on an agarose film. *Nucleic Acids Res*. 2002;30(12):e61.
90. Du H, Disney MD, Miller BL, Krauss TD. Hybridization-based unquenching of DNA hairpins on au surfaces: Prototypical "molecular beacon" biosensors. *J Am Chem Soc*. 2003;125(14):4012-4013.
91. Li H, Rothberg LJ. DNA sequence detection using selective fluorescence quenching of tagged oligonucleotide probes by gold nanoparticles. *Anal Chem*. 2004;76(18):5414-5417.
92. Kneipp K, Kneipp H, Itzkan I, Dasari RR, Feld MS. Ultrasensitive chemical analysis by raman spectroscopy. *Chem Rev*. 1999;99(10):2957-2976.
93. Cao YC, Jin R, Mirkin CA. Nanoparticles with raman spectroscopic fingerprints for DNA and RNA detection. *Science*. 2002;297(5586):1536-1540.
94. Mahajan S, Richardson J, Brown T, Bartlett PN. SERS-melting: A new method for discriminating mutations in DNA sequences. *J Am Chem Soc*. 2008;130(46):15589-15601.
95. Braun G, Lee SJ, Dante M, Nguyen T, Moskovits M, Reich N. Surface-enhanced raman spectroscopy for DNA detection by nanoparticle assembly onto smooth metal films. *J Am Chem Soc*. 2007;129(20):6378-6379.
96. Kang T, Yoo SM, Yoon I, Lee SY, Kim B. Patterned multiplex pathogen DNA detection by au particle-on-wire SERS sensor. *Nano letters*. 2010;10(4):1189-1193.
97. Mahajan S, Richardson J, Brown T, Bartlett PN. SERS-melting: A new method for discriminating mutations in DNA sequences. *J Am Chem Soc*. 2008;130(46):15589-15601.
98. Jin W, Jin Q, Lin X, Lv S, Zhang Y, Mu Y. A DNA sensor based on surface plasmon resonance for apoptosis-associated genes detection. *Biosensors and Bioelectronics*. 2009;24(5):1266-1269. http://www.sciencedirect.com/science/article/pii/S0956566308003862. doi: 10.1016/j.bios.2008.07.031.
99. Wong IY, Melosh NA. Directed hybridization and melting of DNA linkers using counterion-screened electric fields. *Nano letters*. 2009;9(10):3521. http://www.ncbi.nlm.nih.gov/pubmed/19606816.
100. Heaton RJ, Peterson AW, Georgiadis RM. Electrostatic surface plasmon resonance: Direct electric field-induced hybridization and denaturation in monolayer nucleic acid films and label-free discrimination of base mismatches. *Proceedings of the National Academy of Sciences*. 2001;98(7):3701-3704.
101. Pollet J, Delport F, Janssen KP, et al. Fiber optic SPR biosensing of DNA hybridization and DNA–protein interactions. *Biosensors and Bioelectronics*. 2009;25(4):864-869.
102. Sassolas A, Leca-Bouvier BD, Blum LJ. DNA biosensors and microarrays. *Chem Rev*. 2008;108(1):109-139.
103. Karamollaoğlu İ, Öktem HA, Mutlu M. QCM-based DNA biosensor for detection of genetically modified organisms (GMOs). *Biochem Eng J*. 2009;44(2):142-150.
104. Wang J, Nielsen PE, Jiang M, Cai X. Mismatch-sensitive hybridization detection by peptide nucleic acids immobilized on a quartz crystal microbalance. *Analytical Chemistry*. 1997;69(24):5200-5202. http://www.ncbi.nlm.nih.gov/pubmed/9414622. doi: 10.1021/ac9706077.
105. Drummond TG, Hill MG, Barton JK. Electrochemical DNA sensors. *Nat Biotechnol*. 2003;21(10):1192-1199.
106. Patolsky F, Lichtenstein A, Willner I. Electronic transduction of DNA sensing processes on surfaces: Amplification of DNA detection and analysis of single-base mismatches by tagged liposomes. *J Am Chem Soc*. 2001;123(22):5194-5205.
107. Calleja M, Nordstrm M, Alvarez M, Tamayo J, Lechuga LM, Boisen A. Highly sensitive polymer-based cantilever-sensors for DNA detection. *Ultramicroscopy*. 2005;105(1):215-222.
108. Fritz J, Baller MK, Lang HP, et al. Translating biomolecular recognition into nanomechanics. *Science*. 2000;288(5464):316-318.
109. Hansen KM, Ji H, Wu G, et al. Cantilever-based optical deflection assay for discrimination of DNA single-nucleotide mismatches. *Anal Chem*. 2001;73(7):1567-1571.

110. Wohlgamuth CH, McWilliams MA, Slinker JD. DNA as a molecular wire: Distance and sequence dependence. *Anal Chem*. 2013;85(18):8634-8640.
111. Genereux JC, Barton JK. Mechanisms for DNA charge transport. *Chem Rev*. 2009;110(3):1642-1662.
112. Jortner J, Bixon M, Voityuk AA, Rosch N. Superexchange mediated charge hopping in DNA. *The Journal of Physical Chemistry A*. 2002;106(33):7599-7606.
113. Giese B, Wessely S, Spormann M, Lindemann U, Meggers E, Michel-Beyerle ME. On the mechanism of long-range electron transfer through DNA. *Angewandte Chemie International Edition*. 1999;38(7):996-998.
114. O'Neil MA, Barton JK. DNA charge transport: Conformationally gated hopping through stacked domains. *J Am Chem Soc*. 2004;126(37):11471-11483.
115. Singhal P, Kuhr WG. Direct electrochemical detection of purine-and pyrimidine-based nucleotides with sinusoidal voltammetry. *Anal Chem*. 1997;69(17):3552-3557.
116. Paleček E. Polarography of single-stranded homopolynucleotides. *Journal of Electroanalytical Chemistry and Interfacial Electrochemistry*. 1969;22(3):347-358.
117. Wang J, Bollo S, Lopez Paz JL, Sahlin E, Mukherjee B. Ultratrace measurements of nucleic acids by baseline-corrected adsorptive stripping square-wave voltammetry. *Anal Chem*. 1999;71(9):1910-1913.
118. Kerman K, Ozkan D, Kara P, et al. Label-Free bioelectronic detection of point mutation by using peptide nucleic acid probes. *Electroanalysis*. 2003;15(7):667-670.
119. Thorp HH. Cutting out the middleman: DNA biosensors based on electrochemical oxidation. *Trends Biotechnol*. 1998;16(3):117-121.
120. Zhang Y, Kim H, Mano N, Dequaire M, Heller A. Simple enzyme-amplified amperometric detection of a 38-base oligonucleotide at 20 pmol L-1 concentration in a 30-µL droplet. *Analytical and bioanalytical chemistry*. 2002;374(6):1050-1055.
121. Zhang Y, Kim H, Heller A. Enzyme-amplified amperometric detection of 3000 copies of DNA in a 10-µL droplet at 0.5 fM concentration. *Anal Chem*. 2003;75(13):3267-3269.
122. de Lumley-Woodyear T, Campbell CN, Freeman E, Freeman A, Georgiou G, Heller A. Rapid amperometric verification of PCR amplification of DNA. *Anal Chem*. 1999;71(3):535-538.
123. Xie H, Zhang C, Gao Z. Amperometric detection of nucleic acid at femtomolar levels with a nucleic acid/electrochemical activator bilayer on gold electrode. *Anal Chem*. 2004;76(6):1611-1617.
124. Ding Y, Wang Q, Gao F, Gao F. Highly sensitive and selective DNA biosensor using a dumbbell-shaped bis-groove binder of bi-acetylferrocene ethylenediamine complex as electrochemical indicator. *Electrochim Acta*. 2013;106:35-42.
125. Ihara T, Maruo Y, Takenaka S, Takagi M. Ferrocene-oligonucleotide conjugates for electrochemical probing of DNA. *Nucleic Acids Res*. 1996;24(21):4273-4280.
126. Kang D, Zuo X, Yang R, Xia F, Plaxco KW, White RJ. Comparing the properties of electrochemical-based DNA sensors employing different redox tags. *Anal Chem*. 2009;81(21):9109.
127. Takenaka S, Uto Y, Kondo H, Ihara T, Takagi M. Electrochemically active DNA probes: Detection of target DNA sequences at femtomole level by high-performance liquid chromatography with electrochemical detection. *Anal Biochem*. 1994;218(2):436-443.
128. Nakayama M, Ihara T, Nakano K, Maeda M. DNA sensors using a ferrocene-oligonucleotide conjugate. *Talanta*. 2002;56(5):857-866.
129. Fan C, Plaxco KW, Heeger AJ. Electrochemical interrogation of conformational changes as a reagentless method for the sequence-specific detection of DNA. *Proceedings of the National Academy of Sciences*. 2003;100(16):9134-9137.
130. Kerman K, Ozkan D, Kara P, et al. Label-Free bioelectronic detection of point mutation by using peptide nucleic acid probes. *Electroanalysis*. 2003;15(7):667-670.
131. Kerman K, Ozkan D, Kara P, Meric B, Gooding JJ, Ozsoz M. Voltammetric determination of DNA hybridization using methylene blue and self-assembled alkanethiol monolayer on gold electrodes. *Anal Chim Acta*. 2002;462(1):39-47.

132. Kelley SO, Barton JK, Jackson NM, Hill MG. Electrochemistry of methylene blue bound to a DNA-modified electrode. *Bioconjug Chem*. 1997;8(1):31-37.
133. Boon EM, Ceres DM, Drummond TG, Hill MG, Barton JK. Mutation detection by electrocatalysis at DNA-modified electrodes. *Nat Biotechnol*. 2000;18(10).
134. Xiao Y, Lai RY, Plaxco KW. Preparation of electrode-immobilized, redox-modified oligonucleotides for electrochemical DNA and aptamer-based sensing. *Nature protocols*. 2007;2(11):2875-2880.
135. Fojta M, Daňhel A, Havran L, Vyskočil V. Recent progress in electrochemical sensors and assays for DNA damage and repair. *TrAC Trends in Analytical Chemistry*. 2016;79:160-167.
136. Palecek E, Bartosik M. Electrochemistry of nucleic acids. *Chem Rev*. 2012;112(6):3427-3481.
137. Odenthal KJ, Gooding JJ. An introduction to electrochemical DNA biosensors. *Analyst*. 2007;132(7):603-610.
138. Shen Z, Sintim HO, Semancik S. Rapid nucleic acid melting analyses using a microfabricated electrochemical platform. *Anal Chim Acta*. 2015;853:265-270.
139. Šípová H, Homola J. Surface plasmon resonance sensing of nucleic acids: A review. *Anal Chim Acta*. 2013;773:9-23.
140. Bantz KC, Meyer AF, Wittenberg NJ, et al. Recent progress in SERS biosensing. *Physical Chemistry Chemical Physics*. 2011;13(24):11551-11567.
141. Zhao W, Xu J, Chen H. Photoelectrochemical DNA biosensors. *Chem Rev*. 2014;114(15):7421-7441.
142. Peterlinz KA, Georgiadis RM, Herne TM, Tarlov MJ. Observation of hybridization and dehybridization of thiol-tethered DNA using two-color surface plasmon resonance spectroscopy. *J Am Chem Soc*. 1997;119(14):3401-3402.
143. Furst AL, Hill MG, Barton JK. A multiplexed, two-electrode platform for biosensing based on DNA-mediated charge transport. *Langmuir*. 2015;31(23):6554-6562.
144. Lucarelli F, Tombelli S, Minunni M, Marrazza G, Mascini M. Electrochemical and piezoelectric DNA biosensors for hybridisation detection. *Anal Chim Acta*. 2008;609(2):139-159.
145. Chen T, Jia Y, Dong C, Gao J, Mak P, Martins RP. Sub-7-second genotyping of single-nucleotide polymorphism by high-resolution melting curve analysis on a thermal digital microfluidic device. *Lab on a Chip*. 2016;16(4):743-752.
146. Biala K, Sedova A, Flechsig G. Sequence and temperature influence on kinetics of DNA strand displacement at gold electrode surfaces. *ACS applied materials & interfaces*. 2015;7(36):19948-19959.
147. Wong IY, Melosh NA. An electrostatic model for DNA surface hybridization. *Biophys J*. 2010;98(12):2954-2963.
148. Spehar-Deleze A, Schmidt L, Neier R, Kulmala S, de Rooij N, Koudelka-Hep M. Electrochemiluminescent hybridization chip with electric field aided mismatch discrimination. *Biosensors and Bioelectronics*. 2006;22(5):722-729.
149. Su H, Surrey S, McKenzie SE, Fortina P, Graves DJ. Kinetics of heterogeneous hybridization on indium tin oxide surfaces with and without an applied potential. *Electrophoresis*. 2002;23(10):1551-1557.
150. Sosnowski RG, Tu E, Butler WF, O'Connell JP, Heller MJ. Rapid determination of single base mismatch mutations in DNA hybrids by direct electric field control. *Proceedings of the National Academy of Sciences*. 1997;94(4):1119-1123.
151. Kekedy-Nagy L, Ferapontova EE, Brand I. Submolecular structure and orientation of oligonucleotide duplexes tethered to gold electrodes probed by infrared reflection absorption spectroscopy: Effect of the electrode potentials. *The Journal of Physical Chemistry B*. 2017;121(7):1552-1565.
152. Papadopoulou E, Goodchild SA, Cleary DW, et al. Using surface-enhanced raman spectroscopy and electrochemically driven melting to discriminate yersinia pestis from Y. pseudotuberculosis based on

single nucleotide polymorphisms within unpurified polymerase chain reaction amplicons. *Anal Chem*. 2015;87(3):1605-1612.
153. Johnson RP, Gao R, Brown T, Bartlett PN. The effect of base-pair sequence on electrochemically driven denaturation. *Bioelectrochemistry*. 2012;85:7-13.
154. Wei F, Chen C, Zhai L, Zhang N, Zhao XS. Recognition of single nucleotide polymorphisms using scanning potential hairpin denaturation. *J Am Chem Soc*. 2005;127(15):5306-5307.
155. Jambrec D, Gebala M, La Mantia F, Schuhmann W. Potential-Assisted DNA immobilization as a prerequisite for fast and controlled formation of DNA monolayers. *Angewandte Chemie International Edition*. 2015;54(50):15064-15068.
156. Jambrec D, Conzuelo F, Estrada-Vargas A, Schuhmann W. Potential-Pulse-Assisted formation of thiol monolayers within minutes for fast and controlled electrode surface modification. *ChemElectroChem*. 2016;3(9):1484-1489.
157. Daggumati P, Appelt S, Matharu Z, Marco ML, Seker E. Sequence-specific electrical purification of nucleic acids with nanoporous gold electrodes. *J Am Chem Soc*. 2016;138(24):7711-7717.
158. Arinaga K, Rant U, Knežević J, et al. Controlling the surface density of DNA on gold by electrically induced desorption. *Biosensors and Bioelectronics*. 2007;23(3):326-331.
159. Drummond TG, Hill MG, Barton JK. Electrochemical DNA sensors. *Nat Biotechnol*. 2003;21(10):1192.
160. Xiang Y, Lu Y. Using personal glucose meters and functional DNA sensors to quantify a variety of analytical targets. *Nature chemistry*. 2011;3(9):697-703.
161. Benvidi A, Firouzabadi AD, Tezerjani MD, Moshtaghiun SM, Mazloum-Ardakani M, Ansarin A. A highly sensitive and selective electrochemical DNA biosensor to diagnose breast cancer. *J Electroanal Chem*. 2015;750:57-64.
162. Liu S, Su W, Li Z, Ding X. Electrochemical detection of lung cancer specific microRNAs using 3D DNA origami nanostructures. *Biosensors and Bioelectronics*. 2015;71:57-61.
163. Kelley SO, Barton JK, Jackson NM, et al. Orienting DNA helices on gold using applied electric fields. *Langmuir*. 1998;14(24):6781-6784.
164. Johnson RP, Gale N, Richardson JA, Brown T, Bartlett PN. Denaturation of dsDNA immobilised at a negatively charged gold electrode is not caused by electrostatic repulsion. *Chemical Science*. 2013;4(4):1625-1632.
165. Ricci F, Plaxco KW. E-DNA sensors for convenient, label-free electrochemical detection of hybridization. *Microchimica Acta*. 2008;163(3-4):149-155.
166. Ngo HT, Wang H, Fales AM, Vo-Dinh T. Label-free DNA biosensor based on SERS molecular sentinel on nanowave chip. *Anal Chem*. 2013;85(13):6378-6383.
167. Seo J, Yaneva R, Cresswell P. Viperin: A multifunctional, interferon-inducible protein that regulates virus replication. *Cell host & microbe*. 2011;10(6):534-539.
168. Ricci F, Lai RY, Plaxco KW. Linear, redox modified DNA probes as electrochemical DNA sensors. *Chemical Communications*. 2007(36):3768-3770.
169. Ricci F, Lai RY, Heeger AJ, Plaxco KW, Sumner JJ. Effect of molecular crowding on the response of an electrochemical DNA sensor. *Langmuir*. 2007;23(12):6827-6834.
170. Kkedy-Nagy L, Shipovskov S, Ferapontova EE. Effect of a dual charge on the DNA-conjugated redox probe on DNA sensing by short hairpin beacons tethered to gold electrodes. *Anal Chem*. 2016;88(16):7984-7990.
171. Mosier-Boss PA. Review of SERS substrates for chemical sensing. *Nanomaterials*. 2017;7(6):142.
172. Singh R. CV raman and the discovery of the raman effect. *Physics in Perspective (PIP)*. 2002;4(4):399-420.
173. Weaver GC, Norrod K. Surface enhanced raman spectroscopy: A novel physical chemistry experiment for the undergraduate laboratory. *J Chem Educ*. 1998;75(5):621.
174. Thomas S. Infrared and raman spectroscopy. https://serc.carleton.edu/NAGTWorkshops/mineralogy/mineral_physics/raman_ir.html. Accessed Apr 6, 2018.

175. Sharma B, Frontiera RR, Henry A, Ringe E, Van Duyne RP. SERS: Materials, applications, and the future. *Materials today*. 2012;15(1):16-25.
176. Benner RE, Von Raben KU, Dornhaus R, Chang RK, Laube BL, Otter FA. Correlation of SERS with cyclic voltammetry for cyanide complexes adsorbed on cu electrodes. *Surf Sci*. 1981;102(1):7-17.
177. Greeneltch NG, Blaber MG, Henry A, Schatz GC, Van Duyne RP. Immobilized nanorod assemblies: Fabrication and understanding of large area surface-enhanced raman spectroscopy substrates. *Anal Chem*. 2013;85(4):2297-2303.
178. Greeneltch NG, Blaber MG, Schatz GC, Van Duyne RP. Plasmon-sampled surface-enhanced raman excitation spectroscopy on silver immobilized nanorod assemblies and optimization for near infrared (λex= 1064 nm) studies. *The Journal of Physical Chemistry C*. 2012;117(6):2554-2558.
179. Cheung CL, Nikolić RJ, Reinhardt CE, Wang TF. Fabrication of nanopillars by nanosphere lithography. *Nanotechnology*. 2006;17(5):1339.
180. Chang J, Chang S, Li Y, et al. Fabrication and luminescent properties of core-shell InGaN/GaN multiple quantum wells on GaN nanopillars. *Appl Phys Lett*. 2012;100(26):261103.
181. Adams TM, Layton RA. *Introductory MEMS: Fabrication and applications.* Vol 70. Springer Science & Business Media; 2009.
182. Mattox DM. *Handbook of physical vapor deposition (PVD) processing.* William Andrew; 2010.
183. Hunt LB. The early history of gold plating. *Gold Bulletin*. 1973;6(1):16-27.
184. Green TA. Gold electrodeposition for microelectronic, optoelectronic and microsystem applications. *Gold Bulletin*. 2007;40(2):105-114.